CENTRO DE BIOCIÊNCIAS

PROGRAMA DE PÓS-GRADUAÇÃO EM CIÊNCIAS BIOLÓGICAS

MARIA ISABELA DE ANDRADE PEREIRA

AGENTES DE CONTRASTE BIMODAIS BASEADOS EM *QUANTUM DOTS* E QUELATOS DE GADOLÍNIO

Recife

2016

MARIA ISABELA DE ANDRADE PEREIRA

AGENTES DE CONTRASTE BIMODAIS BASEADOS EM *QUANTUM DOTS* E QUELATOS DE GADOLÍNIO

Dissertação apresentada ao Programa de Pós-graduação em Ciências Biológicas, como parte dos requisitos necessários à obtenção do título de Mestre em Ciências Biológicas, com ênfase em Biotecnologia.

Orientadora: Profa. Dra. Adriana Fontes

Co-orientadora: Profa. Dra. Giovannia Pereira

Recife

2016

Catalogação na fonte

Elaine Barroso

CRB 1728

Pereira, Maria Isabela de Andrade

Agentes de contraste bimodais baseados em *Quantum dots* e quelatos de gadolínio / Recife: O Autor, 2016.

112 folhas : il., fig., tab.

Orientadora: Adriana Fontes

Coorientadora: Giovannia Pereira

Dissertação (mestrado) – Universidade Federal de Pernambuco. Centro de Biociências. Biotecnologia, 2016.

Inclui referências e anexos

(1) Nanotecnologia 2. Gadolínio 3. Diagnóstico I. Fontes, Adriana (orientadora) II. Pereira, Giovannia (coorientadora) III. Título

620.5 CDD (22.ed.) UFPE/CCB-2017-029

MARIA ISABELA DE ANDRADE PEREIRA

AGENTES DE CONTRASTE BIMODAIS BASEADOS EM *QUANTUM DOTS* E QUELATOS DE GADOLÍNIO

Dissertação de mestrado apresentada ao Programa de Pós-graduação em Ciências Biológicas, como parte dos requisitos necessários à obtenção do título de Mestre em Ciências Biológicas, com ênfase em Biotecnologia.

Aprovada em:15 de julho de 2016.

BANCA EXAMINADORA

Profa. Dra. Adriana Fontes

Programa de Pós-graduação em Ciências Biológicas – UFPE (Presidente)

Profa. Dra. Maria Tereza dos Santos Correia

Programa de Pós-graduação em Ciências Biológicas – UFPE (Membro interno)

Profa. Dra. Claudilene Ribeiro Chaves

Universidade Federal de Minas Gerais – UFMG (Membro externo)

Recife

2016

Dedico à todos que contruibuíram para que essa etapa acadêmica fosse concluída.

AGRADECIMENTOS

Agradeço, primeiramente, à Deus, por ter permitido com que essa etapa acadêmica se concretizasse, em meio a tantas dificuldades na minha vida pessoal e de pós-graduanda. Ele tem me abençoado, desde o início, colocando pessoas especiais em meu caminho, sem as quais, eu não teria conseguido trilhar bem essa jornada.

À minha família, em especial, aos companheiros de apartamento, Waltinho, Ninha, Marcelo, Laika, Flavinho, Toninho, Fatinha, pela convivência diária, preocupação, por todo apoio nas horas difíceis, companheirismo, implicâncias e brincadeiras nas horas de extremo cansaço, tornando meu cotidiano menos monótono e fazendo-me sentir bem, mesmo longe de "casa". Ao meu noivo, Cássio, pelo apoio, pela paciência, companheirismo e momentos de descontração. Não poderia deixar de mencionar a participação essencial de grandes exemplos de pessoas, de princípios a seguir e de educação: meus tios, Enir, Almir, Iêda, Cileide, Edsângela, minhas avós, Bel, Lica, meus avôs Zezinho, Deildo, por todo o suporte e confiança. À minha mãe, Elinete, que palavras seriam poucas para descrever sua dedicação, por ter abdicado de tantas coisas para me proporcionar tudo que estava ao seu alcance, fortalecendo minha base e preocupando-se sempre com o meu futuro. Por todo o amor e atenção concedidos.

À Universidade Federal de Pernambuco, pela experiência adquirida ao longo desses cindo anos de vivência, lugar de grande aprendizado acadêmico e profissional, onde descobri novos horizontes, que me fizeram saber que posso ser e ter mais do que imaginei.

Aos amigos da Turma de graduação, Biomedicina 2010.2, pela amizade mantida mesmo após contato não tão frequentes. Em especial, Alex, Babi, Eduardo, Joana, Gleybson.

Às amigas da Turma do Mestrado, 2014.2, pela parceria desde a seleção, disciplinas, até os dias atuais, sobrevivendo às defesas. Que perduremos torcendo umas pelas outras independentemente da concorrência.

À Prof. Dra. Ana Mendonça, Prof. Elvis França e Crescêncio Andrade agradeço pelas análises de ICP, cruciais para o nosso trabalho, bem como ao pessoal de Campinas (SP) pelas medidas de FCS e Patrícia da CENAPESQ (UFRPE) pela contribuição nas medidas preliminares de RMN.

Aos amigos do LBQ, lugar através do qual cada vez mais novas amizades tem surgido e laços antigos sendo mais consolidados. Nesse "lar", conheci pessoas incríveis que tornaram o trabalho diário mais prazeroso. Destaco meus queridos amigos forever, Nati, Carlos, Lívia, Gilzinha, Dewson, pelos quais tenho grande carinho, e que sei que posso contar além dos

limites acadêmicos. Meu amigo Joãozinho que tanto me aperreia e é parceiro para todas as horas. Preciso agradecer meu amigo Rafael Padilha à parte pelo acalento espiritual que várias vezes acalmou meu coração e provou minha fé em Deus, me fazendo ser mais forte e ter convicção de que tudo passa, e que um ombro amigo sempre terei por perto, representando os demais amigos do laboratório, que não citaria aqui para não ter risco de esquecimento. Muitos estão por longe, mas fizeram história e deixaram saudade (Anna Lívia, Victor, Thiago Jampa, Diogo, Diego). Aos vigentes QDotados do grupo NanoBio, espero dividir cada vez mais conhecimentos e obter mais com nossa troca diária, Thiago, Aline, Cássia, Camila Galvão, "Catarina", Ryan, Jéssika, vocês fazem parte da minha família científica. E, aos queridos Professores, nossos exemplos e responsáveis por compor essa família que é nosso lab, Ricardo, Cláudia, Beate e Adri, meu muito obrigado.

À Giovannia, minha co-orientadora, Goreti, nossa pós-doutoranda, Gabi e Camila Pereira (ICs) que tanto contribuíram para a execução e planejamos dos experimentos e discussão dos nossos resultados, foram fundamentais.

À minha querida orientadora, Adriana Fontes, pelo suporte singular que um orientador poderia fornecer, pela oportunidade de evoluir meu pensamento científico, por ter me ensinado a escrita científica, e por ter me dado a oportunidade de experimentar a docência também. Além de ter viabilizado meu trilhar pelo mundo científico, continua me inspirando cada vez mais e é um grande exemplo de profissional, educadora e pesquisadora. À Paulo, por ter dividido comigo tantos conhecimentos e momentos, por ter me ensinado com paciência no início da minha rotina no laboratório, por ter acompanhado cada passo meu e hoje vejo que andamos juntos e nos ajudando cada dia mais. Sem você o caminho seria bem mais triste, ganhei muito mais do que um colega de trabalho e professor, e sim, um amigo-irmão. À Camila Pereira por toda ajuda e dedicação com nossos experimentos, tão nova, mas tão determinada e inteligente, foi sem dúvida fundamental no desenvolvimento desse trabalho e me orgulho muito em vê-la crescendo. Sei também que posso contar com a sua amizade e parceria além das fronteiras do laboratório.

“O conhecimento exige uma presença curiosa do sujeito em face do mundo. Requer uma ação transformadora sobre a realidade. Demanda uma busca constante. Implica em invenção e em reinvenção”.

Paulo Freire

LISTA DE ILUSTRAÇÕES DO REFERENCIAL TEÓRICO

LISTA DE ILUSTRAÇÕES DO ARTIGO

LISTA DE TABELAS DO ARTIGO

LISTA DE ABREVIATURAS

ACs	Agentes de contraste
AMA	Ácido mercaptoacético
AMP	Ácido mercaptopropiônico
AMS	Ácido mercaptossuccínico
BC	Banda de Condução
BV	Banda de Valência
CdSe	Seleneto de Cádmio
CdTe	Telureto de Cádmio
CIS	Cisteína
CISTM	Cisteamina
QDs	*Quantum dots*
DLS	*Dynamic light scattering*
DOTA	Ligante tetraazacyclododecane tetraacetic acid
DP	Densidade de prótons
EDC	1-etil-3-(3-dimetilaminopropil) carbodiimida
EFM	Ensaio Fluorescente em Microplaca
FCS	*Fluorescence Correlation Spectrocopy*
FL	Fluorescência
FWHM	*Full width at half maximum*
Gd (III)	Íons gadolínio
HeLa	Henrieta Lacks
IR	*Infrared*
IRM	Imagem por ressonânica magnética
NaOH	Hidróxido de sódio
PBS	Tampão fosfato salino
QDs	*Quantum dots*
RMN	Ressonância magnética nuclear
SPIONs	Superparamagnetic iron oxide nanoparticles
Sulfo-NHS	N-hidroxisuccinimida
UV	Ultravioleta

LISTA DE SÍMBOLOS

e^-	elétron
eV	elétron-volt
K	constant de Boltzmann
a_o	raio de Bohr
*E*g	*band gap* de energia
γ	razão giromagnética
h	constante de Plank
h^+	buraco deixado pelo elétron
λ_{emi}	comprimento de onda de emissão
λ_{exi}	comprimento de onda de excitação
M_0	vetor de magnetização
q	moléculas de água coordenadas na esfera interna
r_1	relaxividade a partir do tempo de relaxação longitudinal
r_2	relaxividade a partir do tempo de relaxação transversal
T_1	tempo de relaxação longitudinal
T_2	tempo de relaxação transversal
M_z	magnetização resultante
τ_D	tempo de difusão da água nas proximidades do íon paramagnético
τ_M	tempo de resistência da água coordenaa ao centro paramagnético
τ_R	tempo rotacional do complexo
υ	frequência da luz
ε	coeficiente de extinção molar

RESUMO

A técnica de imagem por ressonância magnética (IRM) é uma poderosa ferramenta de diagnóstico, que apesar de discriminar tecidos saudáveis dos tumorais com boa definição anatômica, muitas vezes necessita de alta concentração de agentes de contraste (ACs) para se atingir a devida diferenciação. Além disso, investigações de eventos com especificidade química a nível celular são limitadas na IRM, as quais podem ser atingidas por técnicas de fluorescência. Devido a essas limitações, ACs nanoparticulados vêm sendo desenvolvidos a fim de aumentar a concentração local de ACs sem que haja aumento da dosagem para que se obtenha um melhor contraste nas imagens, bem como para associar modalidades complementares de imagem em uma só nanopartícula. Assim, o objetivo desse trabalho foi desenvolver um sistema bimodal nanoparticulado baseado na conjugação de quelatos contendo o íon paramagnético gadolínio [Gd (III)] a pontos quânticos, para aplicações em fluorescência e IRM, associando as vantagens de cada técnica a fim de suprir suas respectivas limitações. Preparamos os sistemas bimodais por meio da conjugação covalente entre as carboxilas dos QDs e carboxilas dos quelatos de Gd (III), sendo a etilenodiamina um mediador. Foram testadas diferentes proporções de QDs:quelatos de Gd (III), mas apenas os sistemas com 10, 20 e 30 quelatos por QDs permaneceram estáveis. Para comprovar as propriedades magnéticas dos sistemas, medidas de tempos de relaxação longitudinal (T_1) dos núcleos dos prótons de hidrogênio presentes nas moléculas de água foram realizadas a 300 MHz e 25º C. De acordo com os dados relaxométricos, observou-se que todos os sistemas levaram a diminuições em T_1, sendo o sistema com 30 quelatos o mais promissor com relaxividade de 535 $mM^{-1}.s^{-1}$ por QD e 103 $mM^{-1}.s^{-1}$ por íon Gd (III). Pelo ensaio com resazurina, as células mantiveram-se metabolicamente ativas após incubação com os sistemas bimodais, mostrando que os mesmos praticamente não induzem citotoxicidade. Além disso, os sistemas foram utilizados para marcação de células HeLa, demonstrando também ser potenciais sondas fluorescentes. Assim, os sistemas apresentaram-se como ferramentas promissoras para aquisição de imagens por fluorescência e ressonância magnética nuclear, podendo então ser aplicados para a compreensão de variados processos biológicos.

Palavras-chave: Sistemas bimodais nanoparticulados. Pontos quânticos. Conjugação. Quelatos paramagnéticos.

ABSTRACT

The magnetic resonance imaging technique (MRI) is a powerful diagnostic tool that can distinguish healthy from tumoral tissues with good anatomic resolution. However, MRI usually needs a high concentration of contrasts agents (CAs) to achieve the adequate differentiation. Moreover, investigations of events with biochemical specificity, at cellular and molecular levels, are limited in MRI, which can be achieved by fluorescence techniques. Due to these MRI' limitations, nanoparticulate CAs have been developed in order not only to increase the local concentration of CAs, without increase the dosage aiming to obtain a better contrast in the images, but also to associate more than one imaging modalities into a single nanoparticle. Thus, the objective of this work was to develop a nanoparticulate bimodal system, based on the conjugation of chelates containing paramagnetic ions, namely gadolinium [Gd (III)], with quantum dots (QDs), for applications in fluorescence and MRI techniques, taking advantages of each other in order to supply their respective limitations. For this, bimodal nanosystems were prepared by covalent conjugation between carboxyl coated QDs and carboxyl Gd (III)-chelates by using the ethylenediamine as a mediator. Different proportions of QDs:Gd-chelates were tested, however only the systems with 10, 20 and 30 chelates per QD remained stable. In order to verify the magnetic properties of the systems, measurements of the nuclear longitudinal relaxation time (T_1) of the proton water molecules were performed at 300 MHz and 298 K. According to relaxometric data, all nanosystems were able to decrease T_1 values, being the system with 30 chelates the most promising, presenting a relaxivity of 535 $mM^{-1}.s^{-1}$ and 103 $mM^{-1}.s^{-1}$ per QD and per Gd (III) ion, respectively. By the resazurin assay, HeLa cells remained metabolically active after incubation with bimodal nanosystems, showing that QDs-[Gd (III)-chelates] practically do not induce cytotoxicity. Furthermore, bimodal nanosystems were able to label efficiently HeLa cells, demonstrating to be potential fluorescent probes. Thus, the QDs:Gd (III)-chelates nanosystems developed in this study can be considered as promising tools for acquiring images by fluorescence and magnetic resonance, in order to understand a variety of biological processes.

Keywords: Nanoparticulate bimodal systems. Quantum dots. Conjugation. Paramagnetic chelates.

SUMÁRIO

CAPÍTULO I

1. INTRODUÇÃO

A tendência atual da medicina é de ser personalizada, ou seja, utilizar terapias e diagnósticos mais específicos e individualizados para várias doenças (XIE; LEE; CHEN, 2010). Como a maioria das doenças são multifatoriais, cada vez mais se procura por técnicas capazes de detectar e distinguir os vários mecanismos e/ou processos envolvidos em cada fase da doença, bem como compreendê-la mais profundamente, e como consequência, poder diagnosticar e tratar com mais eficiência. Enquanto outras áreas do conhecimento investigam os indicadores biológicos (ou biomarcadores) das doenças, a imagenologia experimental e clínica podem contribuir com informações, de preferência em tempo real, sobre a localização, atividade e dinâmica desses biomarcadores em processos biológicos (WEISSLEDER; PITTET, 2008).

Dentre as técnicas de imagenologia temos, por exemplo, a aquisição de imagens por ressonância magnética (IRM), que fornece informações de tecidos moles e órgãos em vários planos tridimensionais (WEISSLEDER; PITTET, 2008). A IRM é uma técnica muito utilizada para diagnóstico, principalmente por fornecer contraste de diferentes intensidades que permite distinguir tecidos patológicos de saudáveis com alta definição anatômica e boa resolução espacial, de maneira não invasiva. Para se obter um contraste adequado para distinção segura de determinadas estruturas, pode ser necessário a utilização dos agentes de contraste (ACs). Dentre os ACs comumente utilizados estão os baseados em quelatos paramagnéticos contendo íons gadolínio [Gd (III)], que proporcionam diminuição dos tempos de relaxação longitudinal (T_1) dos núcleos dos prótons de hidrogênio (^{1}H) presentes nas moléculas de água do meio (ZHOU; LU, 2012). Devido à natureza molecular dos ACs, muitas vezes é necessário a administração dos mesmos em concentrações relativamente altas, o que não é tão interessante, devido a sua toxicidade e também por não serem direcionados especificamente ao local de análise.

Por outro lado, para se estudar com especificidade bioquímica a dinâmica dos diversos eventos biológicos, com resolução a nível molecular e celular, é crucial a utilização de ferramentas altamente sensíveis, tais como as técnicas baseadas em fluorescência (GIEPMANS et al., 2006). Porém, para que as estruturas biológicas possam ser visualizadas, de maneira a se obter as informações desejadas, é necessária a utilização de marcadores fluorescentes, pois é a partir deles que advém a especificidade e a sensibilidade dessas técnicas.

Dentro desse contexto, os nanocristais fluorescentes de semicondutores, também chamados de quantum dots (QDs), ou pontos quânticos, vêm atraindo o interesse da nanomedicina por poderem ser aplicados no desenvolvimento de sondas bimodais, que apresentem propriedades óptica e magnética, para associar as vantagens e versatilidades de técnicas com diferentes funcionalidades, tais como as baseadas em fluorescência e ressonância magnética nuclear (RMN).

Os QDs são particularmente promissores para esse fim, pois apresentam propriedades únicas, dentre elas: (1) excelente resistência à fotodegradação, que permite realizar e monitorar estudos biológicos em tempo real; (2) estreito espectro de emissão, que permite múltiplas marcações coloridas e simultâneas com variadas especificidades e (3) superfície ativa que viabiliza conjugações com diversas biomoléculas e/ou compostos que possuam grupos funcionais, tais como fármacos, outras nanopartículas e também compostos paramagnéticos (RESCH-GENGER et al., 2008). Dessa forma, os QDs podem então também ser utilizados para concentrar vários íons de Gd (III) em uma única nanopartícula a fim de intensificar, com ainda mais eficiência, o sinal de RMN, contribuindo assim para um melhor contraste observável nas imagens (STASIUK et al., 2013). Além disso, os QDs podem propiciar a aplicação de uma menor dosagem e direcionar, através de conjugações com biomoléculas, esses ACs aos alvos biológicos que se pretende investigar.

Várias pesquisas têm sido direcionadas para o desenvolvimento de sistemas bimodais envolvendo essa associação de QDs e compostos de Gd (III) através de diferentes estratégias. Dentre elas, as mais exploradas, estão: (1) revestimento de cada nanopartícula de QD com moléculas, tais como lipídeos, associadas a Gd (III), e (2) encapsulação de vários QDs livres e quelatos com Gd (III) no interior de vesículas, como lipossomas (TAN; ZHANG, 2005; KOOLE et al., 2008a). No entanto, tais metodologias não tem se mostrado tão eficientes em reduzir os tempos de relaxação, devido à dificuldade de troca da água, principalmente nos encapsulados, e, porque, geralmente não mantêm um tamanho nanométrico ideal para aplicações biológicas. Além dessas, há também outra abordagem, que baseia-se na conjugação direta de quelatos paramagnéticos à superfície dos QDs. Ainda há poucos trabalhos dessa natureza na literatura, mas essa estratégia se mostra promissora por: (1) manter o raio hidrodinâmico das nanopartículas menor que 10 nm, ideal para minimizar a toxicidade, e (2) favorecer a dinâmica de troca da água, sem barreira que impeça ou dificulte esse processo, a qual influencia na eficiência do sistema em reduzir o T_1 dos núcleos de hidrogênio, quando estão sob ação de um campo magnético externo (GHAGHADA et al., 2009a; CHOI et al., 2007).

Assim, neste trabalho foram desenvolvidos sistemas bimodais nanoparticulados, fluorescentes e magnéticos, baseados em QDs hidrofílicos de CdTe (Telureto de Cádmio) conjugados covalentemente a quelatos DOTA-Gd (III). A eficiência desses nanossistemas em reduzir o tempo de relaxação longitudinal T_1, e fornecer sinal para IRM, foi verificada por meio de medidas relaxométricas a 7 T. Além disso, as propriedades ópticas dessas nanopartículas foram avaliadas através de análises espectroscópicas e o potencial de marcação por fluorescência, bem como a sua toxicidade, foram estudadas utilizando as células cancerígenas HeLa como modelo.

CAPÍTULO II

2. REFERENCIAL TEÓRICO

2.1 *Quantum dots*

Desde 1959, surgiram ideias iniciais sobre a possibilidade de manipulação da matéria em escala atômica, quando o físico americano, Richard Feynman, ministrou uma palestra (*There's Plenty of Room at the Bottom*) proferindo que não haveria princípios físicos que impedissem escrever todos os volumes da Enciclopédia Britânica na cabeça de um alfinete. O físico não imaginava que suas previsões culminariam em um dos domínios tecnológicos mais atrativos e de maior crescimento atual, a nanotecnologia, nomeada primeiramente por Norio Taniguchi somente em 1974 (MARTINS; TRINDADE, 2012).

A nanotecnologia tem desfrutado de grande sucesso devido aos avanços tecnológicos e científicos recentes do século XXI, que vão desde a descoberta de novas rotas de síntese de nanomateriais até o aperfeiçoamento dos microscópios (que possibilitou a caracterização dos sistemas nanoestruturados). No universo "nano", temos, por exemplo, os semicondutores nanocristalinos coloidais, chamados de pontos quânticos ou *quantum dots* (QDs), que representam uma nova classe de sondas fluorescentes, a qual vem atraindo interesse na área acadêmica e comercial, devido a sua vasta aplicação em diversas áreas do conhecimento, dentre elas: a Medicina e a Biologia (MARTINS; TRINDADE, 2012; SMITH; GAO; NIE, 2004).

Segundo teorias descritas por Efros e Brus, em 1982, QDs exibem propriedades ópticas distintas dos mesmos materiais semicondutores quando em escala macroscópica (*bulk*). Para serem consideradas como QDs, as partículas de semicondutores geralmente devem apresentar de 1,5 a 10 nm (sendo,1 nm = 10^{-9} m ou a bilionésima parte de um metro). Assim, as propriedades óptico-eletrônicas dos QDs são fortemente dependentes do tamanho (MARTINS; TRINDADE, 2012; SMITH; GAO; NIE, 2004). As características ópticas dos QDs (espectros de absorção e emissão de luz) são dependentes não só do tamanho, como também da composição dos nanocristais. Além disso, essas características estão relacionadas ao fenômeno/efeito de confinamento quântico (MICHALET; BENTOLILA; WEISS,2008).

Alterando-se a composição química e o tamanho pode-se sintonizar a emissão dos QDs em vários comprimentos de onda diferentes, desde regiões próximas ao ultravioleta (UV), varrendo o espectro de luz visível (400-700 nm), até o infravermelho próximo (*Infrared*

- IR). QDs de tamanhos maiores emitem fluorescência em regiões mais próximas do vermelho, enquanto que, os menores, emitem mais para o azul, como mostra a Figura 1 (SMITH; GAO; NIE,2004).

Figura 1 – *Quantum dots* emitindo fluorescência em diversas regiões do espectro de luz visível, variando-se apenas o tamanho dos nanocristais. Quanto menor o tamanho da partícula mais deslocado para o azul será a sua emissão, por outro lado, quanto maior o tamanho, mais deslocada para o vermelho.

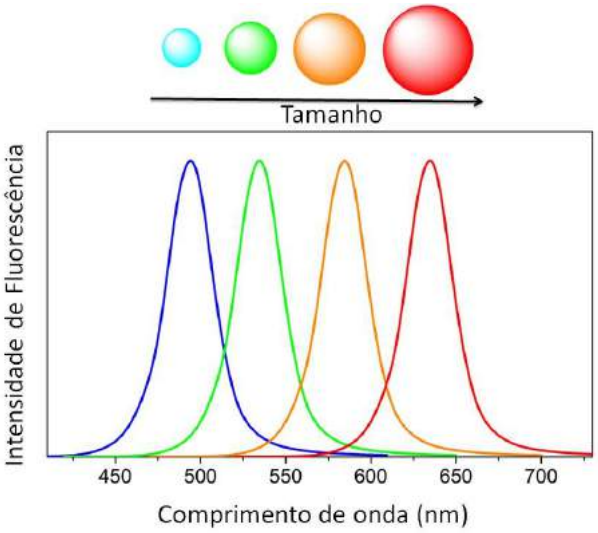

Fonte: PEREIRA, G.

Os sólidos semicondutores apresentam uma estrutura composta por uma banda de valência (BV) e uma banda de condução (BC), que estão separadas por uma diferença de energia chamada *bang gap* (*E*g). A diferença de energia (*E*g) entre as bandas é geralmente expressa em eV (elétron- volt) e refere-se ao mínimo de energia que deve ser fornecida para que os elétrons passem da BV para a BC (Figura 2).

Figura 2 - Esquema de bandas de energia deum semicondutor, sendo BV = banda de valência; BC = banda de condução e *E*g = energia do *bandgap*.

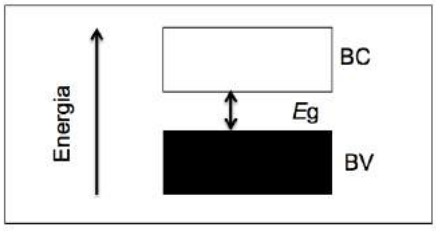

Fonte: A autora (2016).

Nos semicondutores, e consequentemente nos QDs, é possível promover os elétrons para a BC necessitando de uma *E*g normalmente menor que 3 eV, ou seja, neste caso, pode-se utilizar luz no UV ou visível para que esse efeito ocorra à temperatura ambiente (SMITH; GAO; NIE, 2004).

Assim, quando há incidência de energia, na forma de fóton sob o material semicondutor, os elétrons da BV (menor energia) são excitados e vão para a BC (maior energia), deixando um "buraco" na BV, gerando o *éxciton* ou par elétron-buraco. Nessa situação, nem o elétron e nem o buraco constituintes do *éxciton* se movem de maneira independente, devido à atração de Coulomb[1], como mostra a Figura 3 (BRUS, 1984; MICHALET; BENTOLILA; WEISS, 2008).

Figura 3 - Esquema de fotoluminescência de semicondutores. A partir da excitação do elétron (e^-) quando promovido para a banda de condução (BC), há formação de um *éxciton*, que após relaxação e recombinação excitônica, finalmente ocorre a emissão de fluorescência. Onde: h^+ representa o buraco gerado na banda de valência (BV), pela excitação do elétron; *h*υ é a energia E de um fóton necessária para excitar a amostra (E = *h*υ, onde h é a constante de Planck e υ é a frequência da luz).

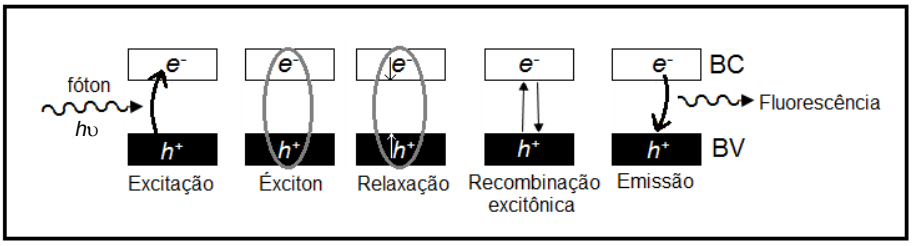

Fonte: A autora (2016).

Após tempos da ordem de nanossegundos, ocorre a recombinação excitônica, os elétrons excitados da BC retornam ao estado fundamental se recombinado com os buracos na BV, gerando assim uma emissão de luz (fluorescência) característica dos semicondutores, isso ocorre tanto na escala nanométrica quanto no *bulk* (sólido macroscópico).

No caso do cristal macroscópico, o elétron pode ocupar uma variedade de estados energéticos que estão distribuídos de modo contínuo. Mas, quando os cristais estão em confinamento quântico, ou seja, quando as três dimensões do material tornam-se fisicamente menores que o raio de Bohr[2], eles são chamados de *quantum dots* e o processo de

[1] A atração de Coulomb é a interação eletrostática que ocorre entre os átomos de carga positiva e negativa, que os mantém a certa distância. Isso é o que mantém o par elétron-buraco (*éxciton*), de modo que estes não se movem de maneira independente. [2]Em analogia aos átomos de hidrogênio (composto por um elétron e um próton), o raio de Bohr é definido como a distância média entre o elétron e o buraco do *éxciton* e é típico de cada semicondutor.

fotoluminescência apresenta propriedades distintas, como será descrito a seguir. Cada semicondutor tem seu raio de Bohr ($a0$) característico, como por exemplo, o cristal macroscópico do Seleneto de Cádmio (CdSe) tem $a0$ = 6 nm. QDs compostos por esse semicondutor são muito usados para aplicações biológicas, então uma nanopartícula desse semicondutor só é considerada um QD quando seu diâmetro for menor que 6 nm (MICHALET; BENTOLILA; WEISS, 2008). Assim, quando o cristal está em um regime de confinamento quântico tridimensional (x, y e z), os estados energéticos tornam-se discretos, como mostra a Figura 4, semelhante aos dos átomos. Por isso, os QDs também são também chamados de "átomos artificiais".

Figura 4 - A redução do tamanho das partículas de semicondutores, quando em regime de confinamento quântico, leva à discretização dos níveis de energia e ao aumento do *bandgap.*

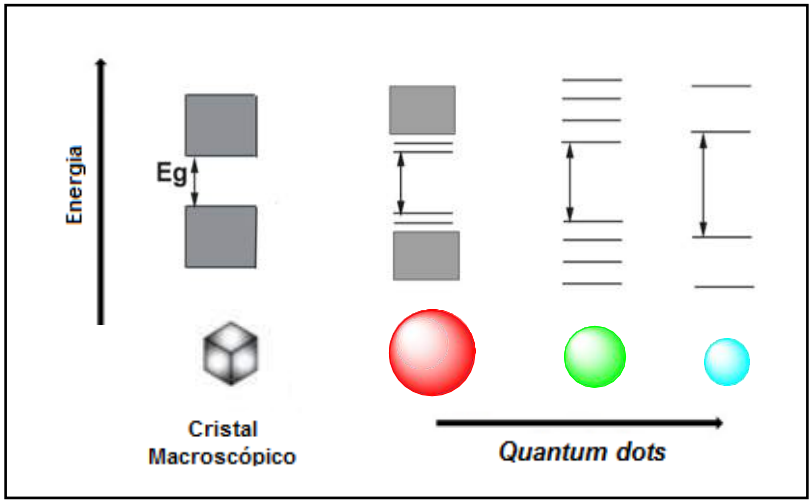

Fonte: A autora (2016).

Como podemos observar, as propriedades ópticas dos QDs são dependentes do seu tamanho, pois o que desempenha um papel chave nessa característica é o regime de confinamento quântico. Isso se deve ao fato do comprimento de onda de emissão estar relacionado à energia do *band gap* (Eg) do nanocristal (YU et al., 2003). Sendo assim, o confinamento quântico, além de gerar discretização dos estados energéticos, gera um aumento da Eg em função da diminuição do tamanho da nanopartícula, assim como mostra a Figura 4. Isso explica o porquê do comprimento de onda de emissão de fluorescência ser sintonizável com o tamanho do nanocristal. Visto que: $Eg\ \alpha 1/d^2$ (sendo, d o diâmetro da nanopartícula) e $Eg\ \alpha 1/\lambda$ (sendo, λ o comprimento de onda de emissão de fluorescência), então d e λ são inversamente proporcionais a Eg. Dessa forma, partículas de semicondutores

menores, emitem na região do azul (menores comprimentos de onda), por terem maior Eg. Enquanto que partículas maiores emitem fluorescência mais para o vermelho (maiores comprimentos de onda), devido à menor *E*g (SANTOS; FARIAS; FONTES, 2008).

Portanto, são essas novas características que esses materiais adquirem, quando em escala "nanométrica", que fazem os QDs serem bastante versáteis para aplicações em Ciências da Vida (SANTOS; FARIAS; FONTES, 2008). A redução do tamanho à escala nanométrica, também favorece a interação desses materiais com os sistemas biológicos, os quais apresentam estruturas e processos nessa escala. Novos dispositivos e técnicas para diagnóstico e terapia vêm sendo impulsionados para monitorar a interação dos nanomateriais com estruturas biológicas. Nesse contexto, as técnicas baseadas em fluorescência são umas das que mais se destacam, como microscopias, fluoroensaios e citometria de fluxo (MARTINS; TRINDADE, 2012).

Quando comparamos os QDs aos corantes convencionais, verificamos que essas nanopartículas apresentam algumas características que as tornam mais vantajosas para serem utilizadas em análises por fluorescência, como: (1) uma única fonte de luz pode excitar a fluorescência dos nanocristais, que poderá emitir em diferentes regiões do espectro, variando-se o tamanho da partícula (corantes convencionais exigem mais de uma fonte de excitação, devido ao seu estreito espectro de absorção – Figura 5); (2) excepcional resistência à fotodegradação (isso permite que as amostras sejam expostas à luz e, que as imagens sejam obtidas com maior intensidade de fluorescência por tempos mais prolongados), como pode ser visto na Figura 6, e (3) são eletrodensos, o que permite a visualização subcelular das nanopartículas por microscopia eletrônica de transmissão (RESCH-GENGER et al.,2008).

Figura 5 - Espectros de absorção e emissão típicos de QDs e corantes convencionais. Os QDs podem ser excitados em vários comprimentos de onda, já os corantes convencionais necessitam de excitação em comprimentos de onda específicos.

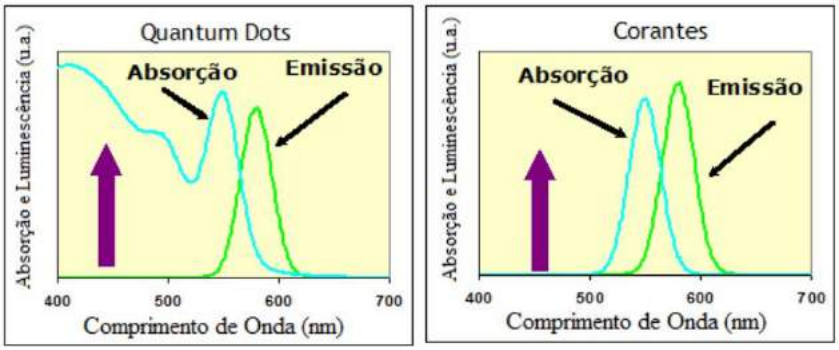

Fonte: Adaptada de FARIAS et al., 2007.

Figura 6 - Resistência à fotodegradação dos QDs ao longo do tempo. Em vermelho, núcleo marcado por QDs (λemi = 630 nm) permaneceram fluorescentes ao longo do estudo. Enquanto que os microtúbulos marcados pelo corante orgânico (AlexaFluor), em verde, tornaram-se indetectáveis a partir de 120 segundos, devido à fotodegradação do corante.

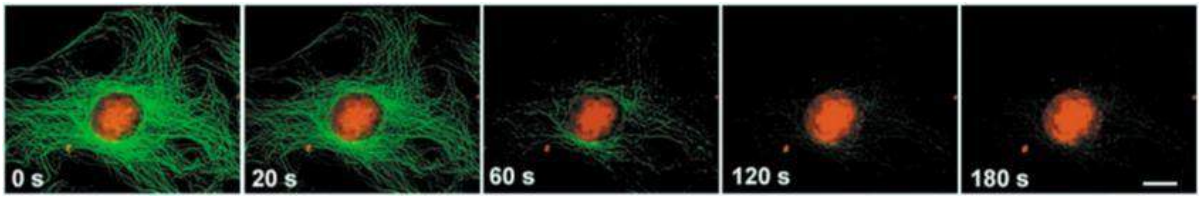

Fonte: Adaptada de WU et al., 2003.

Essas propriedades dos QDs podem melhorar a versatilidade das técnicas de análise baseadas em fluorescência, que são altamente sensíveis, apresentam especificidade bioquímica e permitem o acompanhamento da dinâmica dos eventos biológicos, através de aquisição de imagens ou detecção de sinais.

Com a diminuição do tamanho dessas partículas, também há um aumento da área superficial. O aumento significativo de área superficial contribui com o aumento do número de átomos com ligações não compartilhadas, que são também chamadas de defeitos de superfície, como esquematizado na Figura 7 (MARTINS; TRINDADE, 2012).

Os defeitos diminuem a intensidade de luminescência dos nanocristais, devido à formação de níveis intermediários de energia entre a BV e a BC. Isso favorece a perda de energia do elétron pouco a pouco ao se deslocar da BC para a BV, ao invés do elétron ir diretamente de uma banda à outra. Por isso, essas ligações são chamadas de "armadilhas". Assim, quando há defeitos, há diminuição da intensidade e da qualidade da emissão de fluorescência pelos nanocristais (Figura7).

Uma maneira de solucionar esse problema dos defeitos de superfície, ou minimizá-los, é crescer uma "casca" com outro material semicondutor, geralmente de maior *band gap*, que o semicondutor que forma o núcleo da nanopartícula. Ao final do processo de síntese, tem-se uma estrutura do tipo núcleo/casca. Este processo diminui os defeitos (que comprometeriam a qualidade da emissão desses nanocristais) e otimiza as propriedades fluorescentes (levando a espectros de emissão mais estreitos, com largura à meia altura – FWHM, do inglês *full width at half maximum* – em torno de 40 a 50 nm e com maior intensidade), como mostra a Figura 7 (MARTINS; TRINDADE, 2012; SILVA et al., 2010).

Figura 7 - Presença da camada de passivação nos QDs de estrutura "*core/shell*" promove aprimoramento da emissão de fluorescência, por intensidade e estreitamento da largura do espectro (FWHM). Na ausência dessa camada, os elétrons interagem com "armadilhas" criadas pelos defeitos de superfície, comprometendo a qualidade da fluorescência. À direita da figura temos os espectros de absorção (linha cinza) e emissão (linha preta).

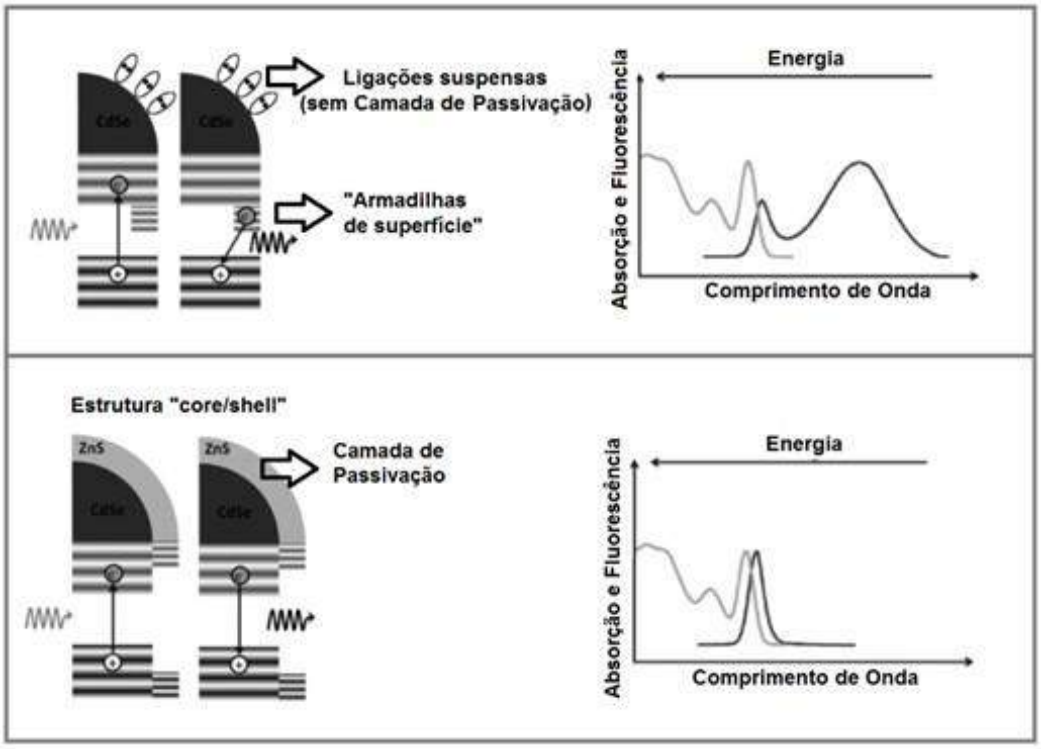

Fonte: Adaptado de MARTINS; TRINDADE, 2012.

Por essas razões, os QDs têm sido sintetizados com o objetivo de aperfeiçoar as suas propriedades ópticas e estabilidade química, obtendo-se nanocristais com distribuição estreita de tamanho (população homogênea) e defeitos de superfície minimizados (SILVA et al., 2010). As sínteses desses materiais podem ser realizadas pelo método *bottom-up*, empregando-se as técnicas de química coloidal, que se baseiam numa reação de precipitação controlada de nanopartículas (fase dispersa), de preferência em água (meio de dispersão ou dispersante). Rogach e colaboradores (2007) iniciaram as primeiras descrições sobre sínteses em meio aquoso que apresentam diversas vantagens, como: boa reprodutibilidade, baixo custo, menor toxicidade, formação de produtos hidrofílicos e, portanto, mais biocompatíveis com sistemas biológicos (HINES; GUYOT- SIONNEST, 1996; ROGACH et al., 2007; SILVA et al.,2010).

Os QDs podem ser feitos de vários tipos de materiais semicondutores baseando-se em combinações dos elementos de diferentes famílias da tabela periódica, podendo ser divididos nos tipos: II – VI, III – V ou IV – VI, segundo a classificação antiga da tabela (SILVA et al.,

2010). Atualmente, os elementos dividem-se em grupos, mas a classificação em famílias ainda permanece em uso. Os QDs hidrofílicos podem ser formados, por exemplo, por elementos das famílias IIB e VIA da tabela periódica. Para exemplificar, temos os nanocristais de CdTe (Telureto de Cádmio) que são do tipo II – VI, pois são formados por Cádmio, que pertence ao grupo 12 (antiga família IIB) e o Telúrio do grupo 16 (antiga família VIA).

No processo de síntese, a nucleação é a primeira etapa e ocorre quando há injeção rápida do precursor calcogênio (como Telúrio) em uma solução homogênea de elevada concentração dos monômeros precursores (como Cádmio). A concentração do precursor e velocidade de reação vai diminuindo à medida que se formam os núcleos iniciais das nanopartículas, como mostra a Figura 8. Essa etapa determina o número de partículas e, em grande parte, o seu tamanho médio, já que núcleos pré-formados crescem gerando partículas isoladas, as quais vão crescendo por consumo dos reagentes. Nesse sistema é importante a presença do agente estabilizante (como o ácido mercaptossuccínico – AMS), que se liga à superfície das partículas, no intuito de prevenir aglomeração de nanopartículas e precipitação e, desligam-se para permitir o crescimento, ou seja, é um comportamento dinâmico (*on*/*off*) em torno dos nanocristais (SILVA et al., 2010; MARTINS; TRINDADE, 2012).

Figura 8 - Síntese dos nanocristais de semicondutores. Etapas de nucleação, crescimento dos núcleos pré-formados, gerando partículas isoladas.

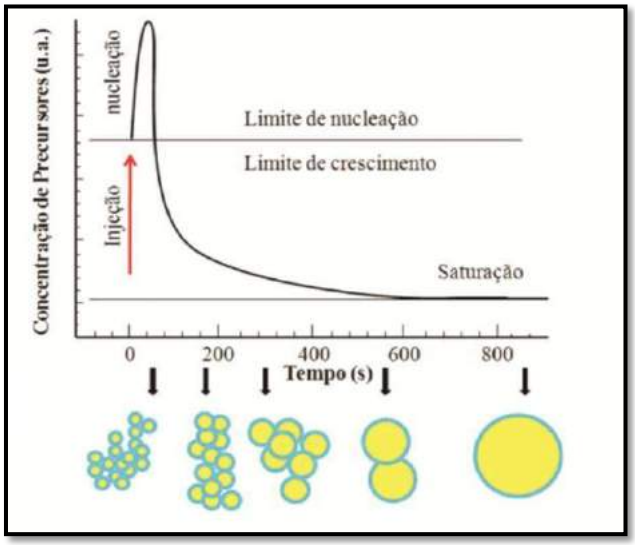

Fonte: Adaptada de SILVA et al., 2010.

Os principais agentes estabilizantes utilizados em QDs coloidais hidrofílicos apresentam o grupamento tiol (–SH) em sua estrutura, tais como: ácido mercaptoacético

(AMA), ácido 3- mercaptopropiônico (AMP), ácido mercaptossuccínico (AMS), L-cisteína (CIS) e cisteamina (CISTM). Componentes contendo esses grupamentos tióis são importantes estabilizantes de nanopartículas, pois o enxofre pode atuar como precursor da camada de passivação. Além disso, os estabilizantes também conferem cargas aos QDs por apresentarem grupos polares, mantendo as partículas afastadas em suspensão e ainda fornecem um grau de funcionalidade às mesmas, atuando como ponte química para interação dos QDs com moléculas orgânicas, por exemplo. Sendo assim, o tipo de interação dos QDs com moléculas depende dos grupos funcionais que estão disponíveis em sua superfície (ácidos carboxílicos ou aminas), os quais são determinados pelo agente estabilizante/funcionalizante escolhido na síntese (FONTES et al., 2012; ROGACH et al.,2007).

Ao final da síntese temos uma nanoestrutura composta por camadas, onde: (1) o núcleo da nanopartícula determina sua emissão, (2) a camada de passivação determina a intensidade e qualidade da emissão e a fotoestabilidade e, por fim, (3) a camada orgânica e mais externa, de agente estabilizante (e funcionalizador), determina a sua estabilidade química e o grau de funcionalidade em relação à marcação do sistema biológico de interesse (Figura 9).

Figura 9 - Esquema de um *quantum dot* funcionalizado quimicamente para sua utilização como marcadores fluorescentes.

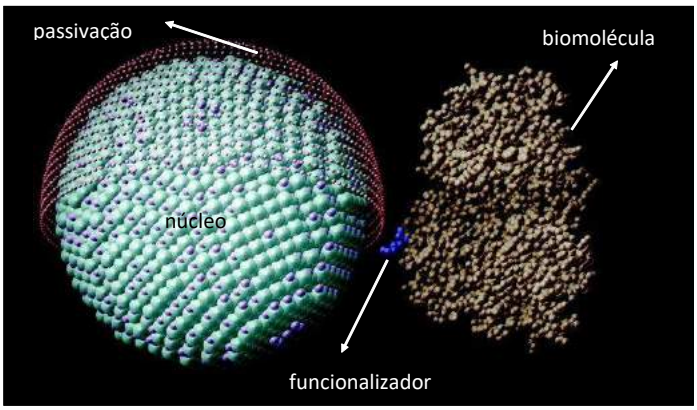

Fonte: Adaptada de MEDINTZ et al., 2004.

Essa superfície ativa dos QDs promovida pelo funcionalizador permite a interação dessas nanopartículas com biomoléculas, tais como anticorpos, proteínas e lectinas, que vão dar um direcionamento biológico mais específico para que essa nanopartícula seja útil em aplicações biológicas sítio-específico. Por isso, QDs têm atraído o interesse de

pesquisadores, sendo úteis em: ensaios bioanalíticos; imagens *in vitro* de células e tecidos; imagens *in vivo* de pequenos animais; diagnóstico e estudo de processos biológicos de câncer e outras doenças e, recentemente, em biossensores e para terapia fotodinâmica (ANDRADE et al., 2013; ESTEVE-TURRILLAS; ABAD- FUENTES, 2013; FONTES et al., 2012; KAIRDOLF et al., 2013). Além disso, é possível conjugar os QDs a outros compostos que possuam grupos funcionais ou a outras nanopartículas, desenvolvendo sistemas inovadores aplicáveis em mais de uma modalidade de imagem (KOKTYSH; BRIGHT; PHAM, 2011; MULDER et al., 2010).

2.2 Tipos e técnicas de processos de conjugação de *quantum dots*

O processo de recobrimento do nanocristal com biomoléculas, ou outros compostos, é chamado de conjugação. A conjugação deve ser realizada de maneira que preserve as propriedades fluorescentes dos QDs e as propriedades funcionais dos demais componentes, os quais podem ser desde aminoácidos, proteínas, anticorpos, fármacos, até mesmo agentes de contraste utilizados clinicamente em IRM (Imagem por Ressonância Magnética), ou outras nanopartículas (MAHMOUD et al., 2011; NA; SONG; HYEON, 2009; SONG; CHAN, 2011).

A superfície dos QDs, com seus funcionalizantes, favorece essa ligação química entre o nanocristal e componentes com grupos funcionais. Essa ligação pode ser obtida por diferentes estratégias, como:

(2) adsorção simples, onde, os próprios agentes funcionalizantes dos QDs, tais como AMP e AMS (que possuem grupos carboxílicos disponíveis) ou CIS (com grupos aminas e carboxílicos) interagem eletrostaticamente com grupos funcionais dos componentes a seremconjugados;

(3) ligação covalente, a qual envolve diferentes agentes de acoplamento, usualmente carbodiimidas e aditivos [1-etil-3-(3-dimetilaminopropil)carbodiimida) (EDC)) e *N*-hidroxisulfosuccinimida (Sulfo-NHS)]; maleimidas[Sulfosuccinimidil-4-(N-maleimidometil) ciclohexano-1-carboxilato (Sulfo-SMCC)] ou glutaraldeído;

(4) interação avidina ou estreptavidina com biotina (HERMANSON,2008).

Em relação à conjugação por adsorção, que é baseada em interações eletrostáticas e/ou hidrofóbicas (Van der Waals), é um método bastante simples e economicamente satisfatório,

por dispensar a utilização de outras substâncias, além de ser vantajoso para conjugações que envolvam biomoléculas, por não desnaturar a proteína. No entanto esse tipo de interação, pode ser menos reprodutível e o conjugado apresentar uma menor durabilidade.

Enquanto que a conjugação do tipo covalente é vantajosa por ser mais reprodutível e duradoura, podendo ocorrer por meio de agentes de acoplamento. Tais agentes são mediadores da interação entre QDs e os outros componentes, e a escolha deles dependem dos grupos funcionais dos componentes envolvidos no processo de conjugação. Para promover ligação carboxil-amina (amida) pode-se utilizar o EDC e Sulfo-NHS, já a ligação amina-tiol pode ser favorecida pelo Sulfo-SMCC, e entre aminas, o glutaraldeído pode contribuir para a conjugação (HERMANSON, 2008).

Em particular, EDC e Sulfo-NHS são agentes altamente reativos com ácidos carboxílicos para promover ligação amida com componentes aminados. Como esquematizado na Figura 10, o EDC interage com a carboxila disponível, por meio da carbodiimida (-N=C=N-), formando *o*-acilisouréia, que é um intermediário altamente reativo e instável, com tempo de vida curto. Assim, para se obter um aumento do rendimento e uma melhora na cinética do processo, adiciona-se o Sulfo-NHS. A hidroxila do Sulfo-NHS interage com o complexo reativo *O*-acilisouréia formando o intermediário Sulfo-NHS éster, o qual apresenta maior estabilidade e interage com as aminas primárias, promovendo a formação da ligação amida e consequentemente conjugação (Figura 10).

Figura 10 - Esquema de conjugação covalente entre componentes carboxilados e aminados. O componente carboxilado é ativado por EDC/Sulfo-NHS para formar uma ligação amida com componente aminado.

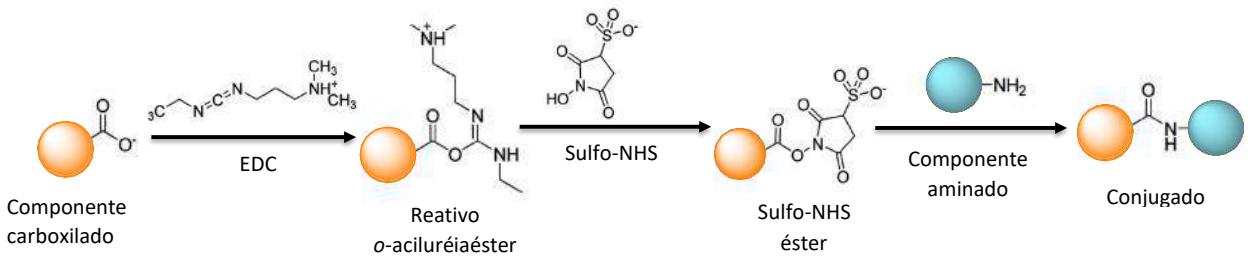

Fonte: Adaptada de WANG et al., 2012.

Esse processo de conjugação ainda é desafiador, pois pode comprometer a qualidade da fluorescência dos nanocristais, bem como a atividade dos componentes que se deseja associar a eles. Assim, é crucial eleger a estratégia de conjugação mais apropriada e investir em

estudos de avaliação da conjugação, a fim de, monitorar e aperfeiçoar esse processo. Para auxiliar nos estudos da conjugação envolvendo QDs, vários métodos têm sido utilizados para avaliar esse processo, tais como: espectroscopia por correlação de fluorescência (FCS – *Fluorescence Correlation Spectroscopy*); dispersão/espalhamento dinâmico de luz (DLS – *Dynamic Light Scattering*), eletroforese, Ensaio Fluorescente em Microplacas (EFM), entre outros (CARVALHO et al., 2014; JANU et al., 2013; SHAO et al., 2009).

A eletroforese e o EFM são comumente utilizados para estudos envolvendo conjugação de QDs a biomoléculas. A técnica de eletroforese avalia a conjugação com base nas diferenças de mobilidade eletroforética dos componentes sozinhos (biomoléculas e QDs) em relação ao conjugado. E, o EFM baseia-se na afinidade dos componentes por uma placa de poliestireno e o sinal fluorescente gerado para o conjugado terá que ser superior a 100 % em relação aos controles para indicar que houve conjugação. Enquanto que a eletroforese é mais laboriosa e qualitativa, o EFM que é um método desenvolvido pelo nosso grupo, tem vantagens por ser mais prático, semi-quantitativo e rápido, permitindo analisar várias amostras ao mesmo tempo (CARVALHO et al., 2014).

Já a técnica de DLS pode informar qualitativamente se há conjugação, para uma amostra de cada vez, com base nos tamanhos médios. No entanto, apresenta baixa resolução e só pode detectar populações de partículas (presentes em uma mesma amostra) se eles diferirem em tamanho, pelo menos, em um fator de 3. No contexto da preparação de sistemas bimodais baseados em QDs e quelatos de íons Gd (III), há trabalhos que utilizaram DLS para analisar essa conjugação, como o de Stasiuk e colaboradores que observaram um aumento de 2 nm dos QDs associados a quelatos, quando comparado aos QDs sozinhos (STASIUK et al., 2011).

A técnica de FCS (espectroscopia por correlação de fluorescência) é mais sensível quando comparada à de DLS. Com o FCS também podemos analisar se houve ou não a conjugação através da análise do tamanho dos sistemas envolvidos. Nessa técnica, partículas ou moléculas fluorescentes passam aleatoriamente no volume focal de detecção e são discriminadas precisamente através das flutuações da intensidade de fluorescência geradas em decorrência de seu movimento browniano, ao entrar e sair desse volume focal (SHAO et al., 2009). O sinal de fluorescência é detectado por uma fotomultiplicadora que gera, em tempo real, um sinal eletrônico formando uma curva de correlação em função do tempo relacionada ao movimento do sistema de interesse no volume focal (THOMAZ, 2013). Além de sensível, a análise é bastante precisa, pois utiliza um microscópio confocal que possui um *pinhole*, o qual restringe o volume focal de detecção e de observação sendo capaz de discriminar cada

partícula ou molécula fluorescentes, mesmo que tenham tamanhos semelhantes. Assim, a FCS é uma ferramenta bastante eficiente e tem sido utilizada para confirmara conjugação de QDs a biomoléculas (CABRAL FILHO et al., 2016), podendo ser estendida para o estudo da conjugação dessas nanopartículas a outros compostos, tais como os quelatos de íons Gd (III).

2.3 Imagem por ressonância magnética nuclear (IRM)

A imagem por ressonância magnética (IRM) é uma das mais poderosas técnicas de diagnóstico utilizada atualmente na prática clínica e está em crescente aprimoramento (BULLMORE, 2012; VAN DER KOLK et al., 2013). Apesar de basear-se no fenômeno da ressonância magnética nuclear (RMN), que foi descrito, em 1946, independentemente, por Felix Bloch e Edward Purcell, a técnica de IRM é relativamente recente (BLOCH; HANSEN; PACKARD, 1946; PURCELL; TORREY; POUND, 1946). Isso porque, a primeira imagem foi demonstrada somente em 1973, por Paul Lauterbur, sendo motivada pela observação de Raymond Damadian (1971), o qual verificou diferenças nos tempos de relaxação nuclear (*T1* e *T2*) dos átomos de hidrogênios (^{1}H) das moléculas de água presentes em tecidos normais e tumorais (DAMADIAN, 1971; LAUTERBUR, 1973).

Na IRM, a obtenção do sinal advém então dos núcleos dos átomos de hidrogênio (^{1}H) presentes no corpo do paciente, visto que: (1) os ^{1}H representam cerca de 80% dos átomos presentes no corpo humano e (2) os ^{1}H são altamente sensíveis ao fenômeno de RMN, que por sua vez é descrito como sendo transições entre níveis de energia de um núcleo com spin nuclear diferente de zero que está exposto a um campo magnético B0. Alguns núcleos com número quântico de spin nuclear *I* diferente de zero que sofrem esse fenômeno são: ^{1}H, ^{2}H, ^{31}P, ^{197}Au, etc.

O ^{1}H é frequentemente referido como próton e se comporta como um minúsculo ímã. Isso porque, como o próton é uma massa com carga em movimento, devido ao seu momento angular de *spin* e ao seu momento magnético, o mesmo age como um dipolo magnético (tendo um polo magnético norte e um sul) e sofre, portanto, interação com campos magnéticos externos (WEISHAUPT; KOCHLI; MARINCEK, 2007).

Segundo a mecânica quântica, o número quântico de *spin* nuclear *I* determina o número de orientações que um núcleo pode assumir diante de um campo magnético externo pela relação $2I + 1$. Para os núcleos de ^{1}H, por exemplo, $I=1/2$ e, portanto há duas orientações possíveis de alinhamento dos spins na presença de B0, denominados: estado α (ou

+½) e estado β (ou -½). O estado de menor energia é aquele que se encontra paralelamente alinhado a B0 [estado α (ou +½)] e o estado de maior energia, antiparalelamente alinhado a B0 [estado β (ou -½)], assim como mostra a Figura 11. Quando um grupo de átomos ^{1}H é colocado sob um campo magnético externo B0, cada *spin* se alinha em uma das duas orientações possíveis (α ou β). Em temperatura ambiente, o número de *spins* no estado de menor energia, N_α (alinhamentos paralelamente), é ligeiramente maior que no estado de maior energia, N_β (alinhados antiparalelamente), o que resulta numa magnetização M0 paralela ao campo magnético. Esta relação é regida pela estatística de Boltzmann, onde ΔE é a diferença de energia entre os dois estados, k é a constante de Boltzmann (k=1,3805x10^{-23} joules/Kelvin), e T é a temperatura em Kelvin:

$$\frac{N_\alpha}{N_\beta} = e^{\frac{-\Delta E}{kT}} \qquad \text{Eq. 1}$$

Figura 11 - Disposição energética dos *spins* nucleares dispostos na ausência (esquerda) e na presença (direita) de um campo magnético externo B0. Onde: (a) indica os *spins* alinhados paralelamente e (b) indica os *spins* alinhados antiparalelamente a B0.

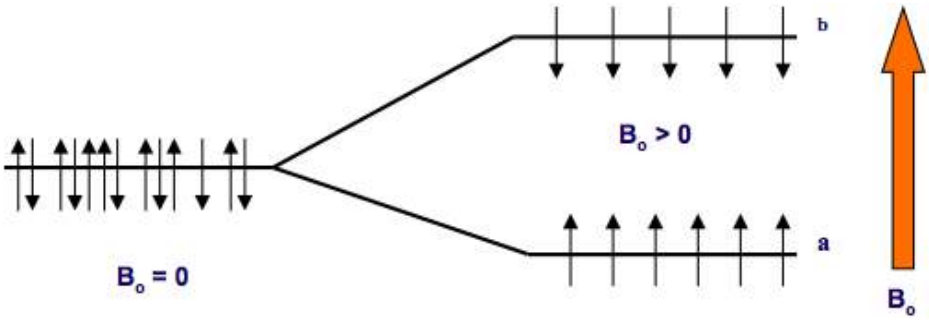

Fonte: A autora (2016).

Dessa forma, na ausência de um campo magnético externo (B0), os *spins* nucleares dos átomos de ^{1}H (ou simplesmente prótons) estão orientados randomicamente. Enquanto que, na presença de B0, os *spins* nucleares orientam-se, paralela e antiparalelamente ao mesmo, resultando em um vetor de magnetização (M0), que é paralelo e proporcional a B0, como mostra a Figura 12. Por exemplo, numa visão simplificada, para um campo de magnético de 1,5 T e na temperatura média do tecido humano, a diferença entre os spins que ocupam o estado de menor energia e o de maior energia é de aproximadamente 5 para 1 milhão. Do ponto de vista prático é somente com estes 5 spins resultantes que se trabalhará na IRM (MAZZOLA, 2009).

Figura 12 – Orientação dos núcleos dos átomos de ^{1}H sem e com um campo magnético externo aplicado. Quando um campo magnético (B0) é aplicado, há alinhamento da maior parte dos núcleos na direção paralela ao campo.

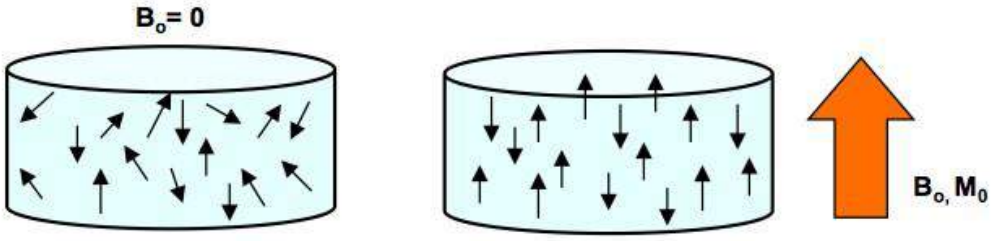

Fonte: A autora (2016).

Na tentativa de alinhamento dos ^{1}H com o campo magnético B_0, e por possuírem *spin*, surge um segundo movimento chamado de precessão (WEISHAUPT; KOCHLI; MARINCEK, 2007). Esse movimento de precessão remete ao movimento de um pião sob o campo gravitacional, que faz um movimento de "cambalear". A frequência de precessão nos prótons [chamada de frequência de Larmor (ν)] é o resultado do torque produzido pela ação de um campo magnético B_0 sobre o seu momento magnético associado, sendo a mesma determinada pela equação 2:

$$\nu = \gamma'.B_0 \qquad \text{Eq. 2}$$

onde $\gamma' = \gamma/2\pi$, sendo γ é a razão giromagnética,e B_0 é o valor do campo magnético aplicado. Sabendo-se que $\gamma/2\pi$ para o hidrogênio é 42,58 MHz/T, então ao aplicar um campo magnético de 1,4 T, os núcleos irão precessionar a uma frequência de 59,6 MHz (WEISHAUPT; KOCHLI; MARINCEK, 2007). Caso o campo magnético seja maior, por exemplo, 6,3 T, então a frequência também aumentará, neste caso para 268,25 MHz. Sendo assim, a frequência de precessão é influenciada diretamente pelo campo magnético aplicado.

Estando num estado de equilíbrio, tem-se $M_0 = M_z$, onde z é o eixo z ou longitudinal e também a direção do campo B_0. Para que seja possível obter um *sinal* de RMN, é necessário aplicar um pulso de radiofrequência (chamada de B_1), perpendicular a B_0, ressonante com a frequência de Larmor ν do átomo de ^{1}H, de modo a perturbar M_0 e consequentemente desviá-lo para plano xy (transversal). Após cessar o pulso de radiofrequência, os núcleos excitados tendem a voltar ao estado de equilíbrio $M_0 = M_z$, através de um processo de perda de energia que é conhecido como processo de relaxação, o qual é modulado por duas constantes exponenciais de tempo, que por sua vez refletem a relaxação devido à perda de energia para o

ambiente (tempo de relaxação longitudinal ou *spin-rede*, T_1) e a relaxação devido a interações entre os *spins* (tempo de relaxação transversal ou *spin-spin*, T_2).

Dependendo da composição das estruturas anatômicas, em uma imagem por RM, teremos uma variação no contraste observado (em tons de cinza) que é dado em função do retorno ao equilíbrio dos ^1H. Assim, se a estrutura é constituída basicamente por gordura (por exemplo: a massa encefálica), que possuem átomos de ^1H ligados ao carbono, o *spin* retorna mais lentamente para M_z. Isso fornece imagem com contraste claro, quando ponderadas em T_1, devido ao sinal hiperintenso. Enquanto que, nas estruturas constituídas basicamente por água, como o líquor, onde a maior concentração de núcleos de ^1H está ligada ao oxigênio, o *spin* retorna mais rapidamente para M_z. Assim, quando ponderadas em T_1 irão fornecer um contraste mais escuro, devido ao sinal hipointenso, como podemos ver na Figura 13A. Se dessas estruturas forem obtidas imagens com ponderação em T_2 (Figura 13B), ocorrerá o inverso, aquelas estruturas constituídas por gordura (como a massa encefálica) apresentarão contraste escuro, exibindo sinal hipointenso. E aquelas compostas por água (como o líquor) apresentarão contraste claro, devido ao sinal hiperintenso.

Figura 13 - Imagens representativas da mesma secção do cérebro obtidas através da ponderação pelo tempo de relaxação longitudinal (T_1) e transversal (T_2). Á esquerda (A), imagem com áreas mais claras, obtida em T_1. À direita (B), imagem com áreas mais escuras, obtida em T_2.

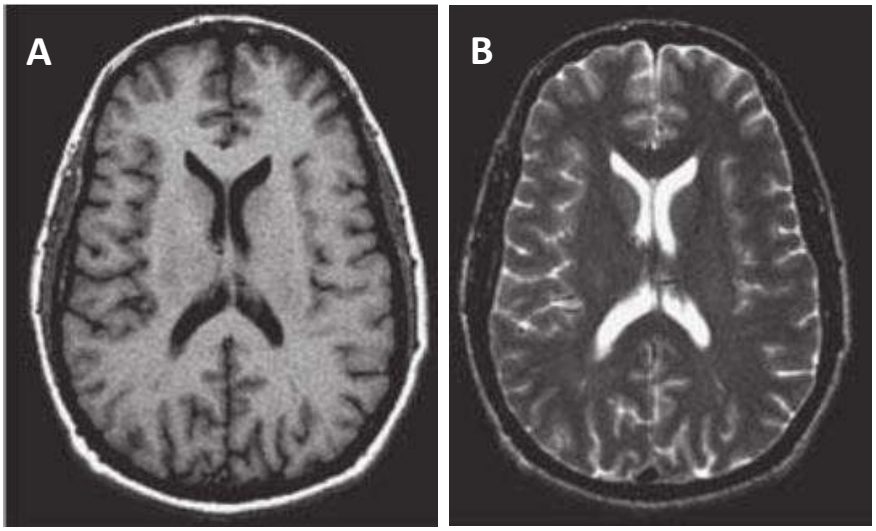

Fonte: Adaptadas de BUXTON, 2002.

A propriedade de fornecer contraste permite então a visualização e distinção de tecidos moles, como matérias brancas e cinzentas do cérebro, como já foi mostrado acima na Figura 13 (KERR, 2002; LANGKAMMER et al., 2012). Além disso, a técnica de IRM possui boa

resolução espacial, na clínica da ordem de 0,8 mm (PEREIRA; GERALDES, 2007). Quando comparada a microscopia, essa apresenta um poder de resolução maior que a IRM, em torno de 0,2 µm, sendo então uma técnica interessante para estudos a nível molecular e celular. Considerando a importância da IRM e sua principal desvantagem: a baixa sensibilidade, pesquisadores têm investigado o papel de agentes de contraste nanoparticulados, como os paramagnéticos e as nanopartículas de ferro superparamagnéticas (SPIONs) para superar essa limitação (SHOKROLLAHI, 2013).

Para a formação da imagem e diferenciação das estruturas com base no contraste, algumas características intrínsecas dos tecidos influenciam, incluindo: densidade de prótons (DP), que está relacionada com a quantidade de água ou gordura, que por sua vez influencia nos respectivos tempos de relaxação T_1 e T_2 (PEREIRA; GERALDES, 2007). A IRM permite, ainda, a reconstrução de imagens projetadas em três ângulos distintos (sagital, coronal e transversal) obtidas por rotação eletrônica do magneto e reconfiguração das bobinas emissoras e receptoras no ângulo desejado para captar o sinal das estruturas de interesse, em torno do paciente. Assim, a IRM fornece imagens multiplanares e definição de estruturas anatômicas com boa resolução (MANSFIELD, 1977; TARDIF et al., 2015).

2.4 Agentes de contraste

Sabe-se que para melhorar o contraste observável e a qualidade das imagens na RMN empregam-se os chamados agentes de contraste (ACs). Normalmente, esses ACs pertencem a uma classe de compostos que permitem a obtenção de imagens mais realçadas, possibilitando a diferenciação entre tecidos saudáveis e aqueles que possuem alguns tipos de alterações morfológicas e metabólicas com melhor precisão (HERMANN et al.,2008).

Em aproximadamente 35% dos exames de IRM, a utilização dos ACs é suficiente para se obter a devida diferenciação entre as estruturas analisadas (SHOKROLLAHI, 2013). Devido à importância clínica da técnica de ressonância magnética tem-se buscado por ACs cada vez mais seguros, no que diz respeito à toxicidade *in vivo*, e eficientes, em termos de relaxividade, que será melhor discutido posteriormente (DE HAËN, 2001).

Os ACs são geralmente baseados em compostos paramagnéticos ou superparamagnéticos, que despertam o interesse clínico por serem altamente susceptíveis à magnetização (BUXTON, 2002). Isto é, quando eles interagem com os ^{1}H das moléculas da água, que formam os tecidos de interesse, promovem redução dos respectivos tempos de

relaxação nuclear (SHOKROLLAHI,2013).

Os ACs também são classificados de acordo com os seus mecanismos associados ao processo de relaxação nuclear, como sendo atuantes em T_1 ou T_2 (NA; SONG; HYEON, 2009). Quando eles promovem uma diminuição do tempo de relaxação em T_1, ocorre um aumento da intensidade do sinal, por isso são ACs que geram um contraste claro nas imagens (HERMANN et al., 2008). Isto é o que ocorre com a utilização de íons paramagnéticos, tais como os quelatos de gadolínio [Gd (III)]. Diferindo da ação das nanopartículas superparamagnéticas de óxido de ferro, por exemplo, que são normalmente atuantes em T_2, gerando um contraste escuro nas imagens (CARAVAN et al., 1999; LAM et al.,2013).

A eficiência dos ACs em diminuir os tempos de relaxação dos núcleos de ^{1}H, por unidade de concentração (mM) de íon paramagnético/superparamagnético é mensurada em termos de relaxividade (r_i, dada em s^{-1} por mM de íon; considerando i = 1,2). Essa relaxividade está relacionada com o aumento da taxa de relaxação ($1/T_i$) dos ^{1}H das moléculas de água provocado por 1 $mmol.L^{-1}$ de íon para- ou superparamagnético (LAURENT et al., 2008). Podendo, então, ser obtida pela seguinte equação:

$$r_{1,2} = \frac{R_{1,2}^{obs} - R_{1,2}^{dia}}{C} \qquad \text{(Eq. 3)}$$

onde, C é a concentração dos íons para- ou superparamagnético e $R_{1,2}^{obs}$ é a taxa de relaxação longitudinal ou transversal ($1/T_{1,2}$) dos ^{1}H da água observada na presença de íons para- ou superparamagnético. Enquanto que $R_{1,2}^{dia}$ refere-se à contribuição diamagnética, ou seja, a taxa de relação dos núcleos de ^{1}H na ausência dos íons para- ou superparamagnéticos. De acordo com a equação, quanto menor forem os valores dos tempos (T_1 e T_2), maior será a relaxividade obtida (r_1 e r_2). Assim, quanto maior a relaxividade, mais eficiente é o AC.

O tempo de relaxação dos prótons da água é considerado como referencial para avaliar a eficiência dos agentes de contraste, sendo eles: *ca.* 3000 ms (T_1) e *ca.* 2500 ms (T_2). Como a relaxividade depende da estrutura molecular e dinâmica do agente de contraste, a relação r_2/r_1 é dependente, por exemplo, do tamanho das estruturas dos ACs, teor de água e porosidade. Determina-se que os ACs são atuantes em T_1 se r_2/r_1 é cerca de 1 ou 2, ou T_2 se r_2/r_1 é superior a 10 (GOSSUIN et al., 2009; HERMANN et al., 2008).

2.5 Quelatos paramagnéticos contendo íons gadolínio

Geralmente, os ACs comumente utilizados em meio clínico contêm metais de transição, como íons ferro e manganês, e também metais de transição interna, nomeadamente o íon gadolínio (SHOKROLLAHI, 2013). Eles possuem um momento magnético efetivo elevado, de pelo menos duas ordens de grandeza maior que o próton, podendo reduzir esses tempos de relaxação do mesmo com base na susceptibilidade magnética (MERBACH; HELM; TÓTH, 2013). O íon gadolínio [Gd (III)] se destaca devido a seu elevado paramagnetismo, consequência dos sete elétrons desemparelhados (maior densidade de *spin*), reduzindo o tempo de relaxação T_1 dos H^1 da água com máxima eficácia (SHOKROLLAHI, 2013).

Entre os ACs paramagnéticos, os quelatos baseados em íons Gd (III) possuem algumas propriedades características que os tornam interessantes, tais como: solubilidade em água (hidrossolúveis), estabilidade química, alta relaxividade em meio aquoso, baixa toxicidade *in vivo* e excreção rápida e completa após procedimento diagnóstico (AIME; BOTTA; TERRENO, 2005). Além disso, os ACs que são baseados em quelatos apresentam uma biodistribuição diferenciada e algumas características podem potencializar seus efeitos, tais como a forma e a movimentação desses ACs até atingirem os tecidos-alvos. Além disso, a capacidade de ficarem retidos no local de interesse influencia diretamente na quantidade da dose do AC necessária a ser administrada (WEISSLEDER; BOGDANOV; PAPISOV, 1992).

Após administração intravenosa desses quelatos de Gd (III), caso o mesmo não seja suficientemente estável cinética e termodinamicamente, pode ocorrer liberação do íon Gd (III), devido à competição com cobre e o zinco intravasculares, processo designado de transmetalação, ou transquelação/reoxidação (HERMANN et al., 2008). Quando em pH fisiológico, o Gd (III) sofre hidrólise rapidamente, tornando-se insolúvel na forma de $Gd(OH)_3$ (PEREIRA; GERALDES, 2007). Ainda, devido à possível competição entre os íons Gd (III) e Ca (II), o primeiro pode depositar-se em ossos em desenvolvimento, como nos de fetos e de crianças, acumulando-se tanto nos ossos, como em outros tecidos, a exemplo disso, no fígado (JUNIOR et al., 2008).

Além disso, os ligantes que constituem os quelatos tem maior seletividade para Gd (III) do que para os cátions endógenos. Sendo assim, esses quelatos garantem uma maior segurança, são bem tolerados e os efeitos tóxicos são praticamente inexistentes. Principalmente, pelo fato da maioria dos quelatos possuírem elevada estabilidade

termodinâmica, cinética e baixo risco de dissociação em fluidos biológicos, em especial os cíclicos (AIME; BOTTA; TERRENO, 2005). Devido a estas propriedades, a partir do início da década de 1980, muitos dos ACs usados em imagem por ressonância magnética possuem os quelatos de Gd (III) como seu principal componente ativo (DE HAËN,2001).

Os quelatos de Gd (III) utilizados para IRM são compostos de coordenação, onde o íon é complexado por ligantes orgânicos multidentados, geralmente os poliaminocarboxilados. De acordo com a sua estrutura, eles são classificados como (i) lineares, que são triaminas acíclicas derivados da dietilenotriamina, e (ii) cíclicos (ou tetraazamacrocíclicos), que derivam do cicleno (cicleno = 1,4,7,10-tetraazaciclododecano), sendo esses últimos mais estáveis que os lineares (HERMANN et al., 2008). Compostos de coordenação contendo íons lantanídeos possuem elevados números de coordenação (entre 8 e 12), o que permite, além da coordenação dos referidos íons com os vários sítios (átomos) disponíveis no ligante, a presença de pelo menos uma molécula de água na esfera interna de coordenação, assim como será explicado mais adiante. Esse fato influencia positivamente na eficiência de um AC, pois a taxa de troca entre a molécula de água coordenada ao íon metálico central (na esfera interna), com moléculas de água presentes no meio (*bulk*) é um dos parâmetros associados aos mecanismos que explicam o processo de relaxação paramagnético desses sistemas (HERMANN et al.,2008).

Atualmente, os principais quelatos de Gd (III) macrocíclicos utilizados clinicamente são:

-Dotarem® [Gd-DOTA (*tetraazacyclododecane tetraacetic acid*)],

-ProHance® [Gd(HP-DO3A)] e

-Gadovist® (Gd-BT-DO3A).

Enquanto que os que possuem estrutura linear são:

-Magnevist® (Gd-DTPA (*diethylenetriamine pentaacetic acid*),

-Omniscan® [Gd(DTPA-BMA)],

-OptiMARK (Gd-DTPA-BMEA),

-MultiHance® (Gd-BOPTA) e

-Eovist® ou Primovist® [Gd(EOB-DTPA)].

A estrutura química e os respectivos valores de relaxividade a um campo de 1.5 T desses quelatos estão apresentados na Figura 14 abaixo.

Figura 14 – Estrutura química dos principais ACs baseados em quelatos de Gd (III) com seus respectivos valores de relaxividade a 1,5 T.

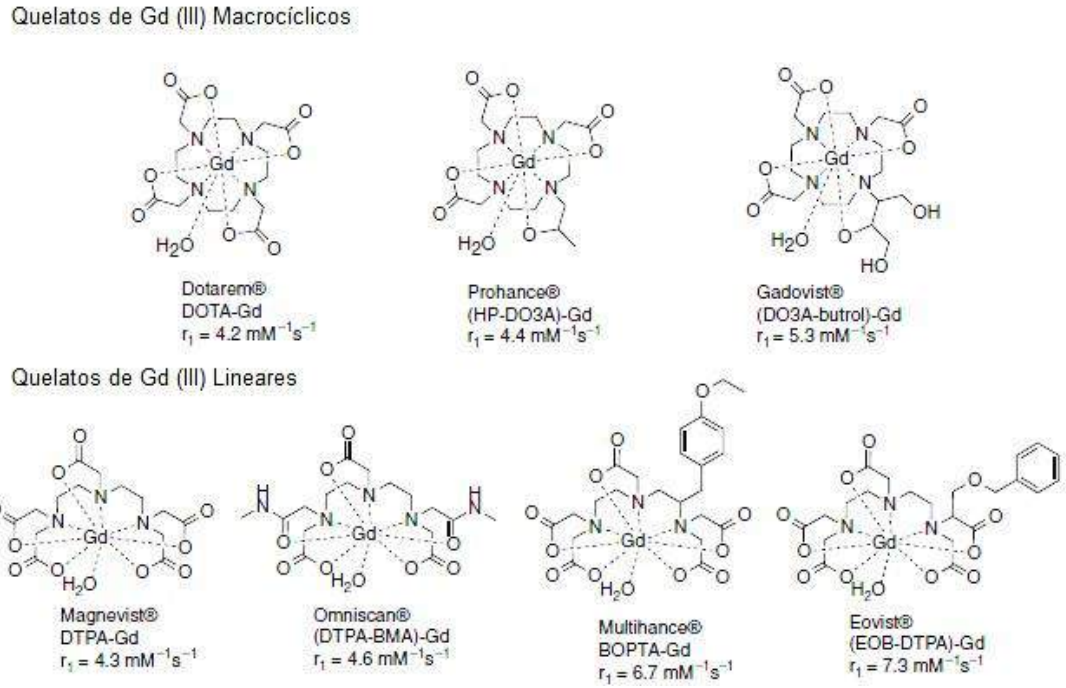

Fonte: Adaptada de HERMANN et al. (2008).

O valor da relaxividade obtida para um determinado AC, ou seja, a eficiência do mesmo em obter o contraste adequado para uma análise clínica é consequência de uma combinação de parâmetros que estão diretamente relacionados à respectiva estrutura molecular. Logo, o processo de relaxação paramagnético é descrito com base em um modelo que considera duas contribuições distintas: (i) a contribuição de "esfera interna", que está relacionada com a troca entre a(s) molécula(s) de água coordenada(s) (*q*) diretamente ao íon metálico e aquelas presentes no meio, e (ii) a contribuição de "esfera externa", resultante da difusão de moléculas de água nas proximidades do íon metálico (CARAVAN et al., 1999; TOTH; HELM; MERBACH, 2002). Como observamos no esquema da Figura 15, um dos parâmetros a ser considerado é o tempo de residência da água coordenada ao centro paramagnético (τ_M), o qual determina a taxa de troca da mesma. Além disso, o número de moléculas de água na esfera interna de coordenação (*q*), o tempo rotacional da molécula (τ_R) e o tempo de difusão de moléculas de água nas proximidades do íon metálico (τ_D) também influenciam na relaxividade observada desses sistemas (Figura15).

Figura 15 – Quelato de Gd (III) em solução. O esquema evidencia a localização das moléculas de água (representadas pelas esferas azuis) que interagem diretamente com o centro paramagnético (ao nível de esfera interna), bem como o tempo de residência da água coordenada (τM), o tempo rotacional do complexo (τR) e de difusão da água nas proximidades do íon (τD).

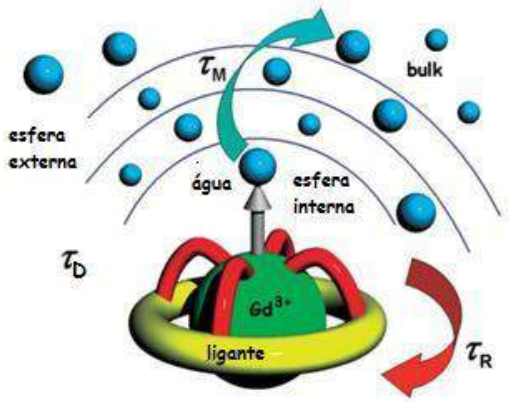

Fonte: Adaptada de HERMANN et al.(2008).

É importante salientar que todos esses parâmetros estão correlacionados e influenciam na resposta de interesse, que é a relaxividade obtida a partir dos valores de T_1 e T_2 medidos. Por exemplo, a contribuição de esfera interna está relacionada com os parâmetros *q*, τM e τR (BLOEMBERGEN; MORGAN, 1961; SOLOMON, 1955). A presença de pelo menos uma molécula de água na primeira esfera de coordenação (*q*) é fundamental para a eficiência dos ACs, sendo o número de *q* é intrínseco à estrutura molecular do quelato. O valor de τM determina a taxa de troca e deve estar num intervalo de tempo que seja ideal para que haja a transferência do efeito paramagnético para a água coordenada e subsequente transferência desse efeito para o *bulk*.

Em termos experimentais, a modificação estrutural do complexo permite alcançar esse objetivo, como, por exemplo, adicionando ou removendo grupos funcionais específicos que aumentam ou diminuem τ_M, seja por impedimento estérico adicional, ou ausência do mesmo. Para o caso de τ_R, que é um parâmetro que está relacionado com movimento do complexo como um todo, é conhecido que quanto maior τ_R, melhor a relaxividade observada. Logo, a diminuição da mobilidade do complexo paramagnético aumenta o tempo rotacional do mesmo, favorecendo mais uma vez a eficiência do referido AC. Nesse caso, é possível aumentar τ_R, ligando o complexo a sistemas bastante maiores, como macromoléculas (proteínas e polissacarídeos) ou nanopartículas (ACCARDO et al., 2004; CORSI et al., 2001).

Os parâmetros que governam a relaxividade são muitos e por isso são necessárias algumas técnicas experimentais associadas com ajustes matemáticos para obtê-los. Dentre as técnicas, cita-se as curvas de relaxividades, medidas em função do campo magnético aplicado, que são asconhecidas curvas de NMRD (*nuclear magnetic resonance dispersion*), além de medidas de RMN de ^{17}O (GONZALEZ et al., 1994; MICSKEI et al.,1993).

Esse papel de coordenação e troca das moléculas de água na relaxividade dos AC têm sido bastante estudado, quando estão em contato direto com o meio e quando encapsulados em vesículas. Sendo menor nessa última condição, devido à barreira de permeabilidade imposta pela membrana, que diminui a troca de água do *bulk* com aquela complexada com o Gd (III) (ZHOU; LU, 2013). Ghaghanda e colaboradores observaram um aumento considerável na relaxividade, quando os quelatos são conjugados na superfície das nanoestruturas (GHAGHANDA et al., 2009). Isso porque a mobilidade dos quelatos torna-se limitada, aumentando, por sua vez, o valor de τ_R. Uma outra consequência da conjugação está relacionada à possibilidade de variação da taxa de troca entre a água coordenada e águas do *bulk*, o que também influencia na relaxividade do sistema, como descrito anteriormente.

Quando o nanocarreador contém tanto quelatos de Gd (III) encapsulados quanto ligados na superfície, como mostra a Figura 16, observa-se uma maior relaxividade (GHAGHANDA et al., 2009). Isso ocorre devido, mais uma vez, à variação da taxa troca da água ($1/\tau_M$), do tempo de rotacional do quelato (τ_R), além de uma maior concentração de Gd (III) por unidade lipossomal, o que é vantajoso, por reduzir a dose do AC para obtenção de um contraste ideal (GHAGHANDA et al., 2009). Diferentemente do que já se espera com a utilização de Gd (III), ou seja, o aumento da relaxividade em T_1, há também um potente efeito na relaxividade transversal (r_2) (KARATHANASIS et al., 2008). Neste caso, a presença de estruturas nanoparticuladas altera o tempo de difusão de moléculas de água próximas ao sistema (τD), parâmetro que está relacionado com a contribuição de esfera externa, que por sua vez influencia significativamente os valores de r_2 (FREED, 1978).

Figura 16 – Esquema de lipossoma como carreador de quelatos de Gd (III). De acordo com o esquema os quelatos de Gd (III) podem estar presentes: (1) livres no interior do lipossoma; (2) conjugados na superfície interna e externa; (3) livres no interior e também conjugados à superfície interna e externa do lipossoma.

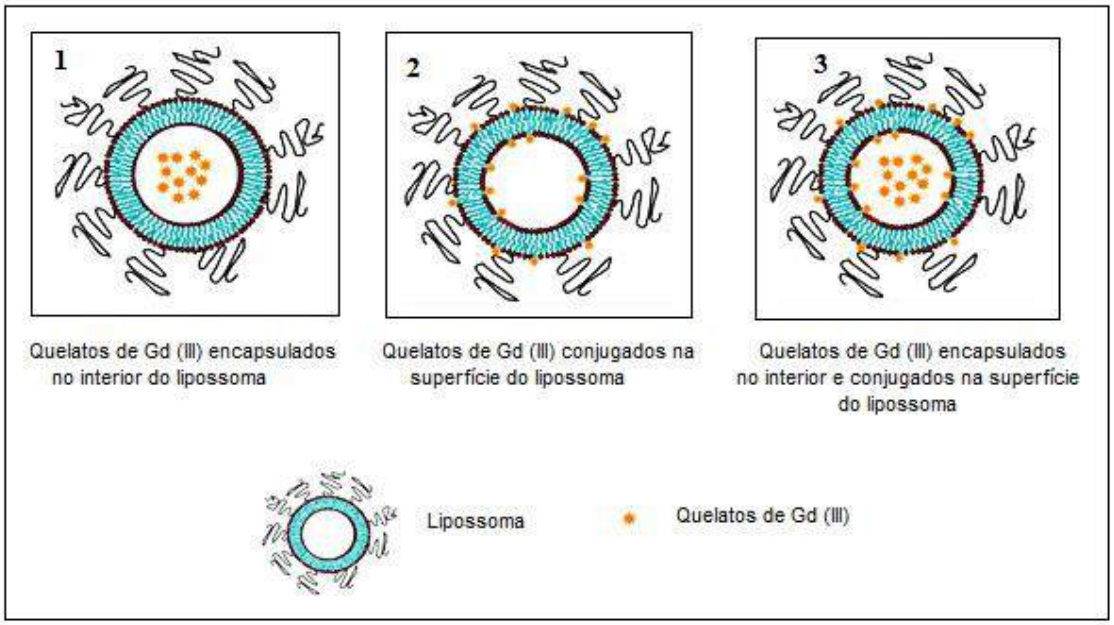

Fonte: Adaptada de GHAGHANDA et al. (2009).

2.6 Sistemas bimodais baseados em QDs e quelatos de Gd (III)

Considerando a importância da imagem por ressonância magnética no diagnóstico e a necessidade de se melhorar o conhecimento sobre os processos e a dinâmica de doenças, a nanotecnologia tem contribuído para a produção de agentes de contraste nanoparticulados multimodais para imagem a nível molecular e celular. Algumas abordagens recentes parecem ser promissoras, por combinar a técnica de IRM com outras modalidades de imagem, tais como as baseadas em fluorescência, aliando assim, as vantagens de ambas as técnicas (PAN et al., 2009).

Vários nanocarreadores têm agregado os íons Gd (III) como componente magnético em sua estrutura, desde nanomicelas (LIU et al., 2011) e QDs (PRINZEN et al., 2007), até sistemas maiores com centenas de nanômetros, como os lipossomas (GHAGHANDA et al., 2009). Muitos desses sistemas híbridos envolvem biomoléculas, para fornecer direcionamento específico ao sistema, através de proteínas, como a albumina

(BHUJWALLA et al., 2003) e peptídeos, como RGD (arginina-glicina-ácido aspártico) (KOOLE et al., 2008; MULDER et al., 2006). Além disso, podem ser utilizados polímeros, para melhorar a sua biocompatibilização, como, por exemplo, o dextran e o PEG (LIU et al., 2011), além dos dendrímeros (SATO et al.,2001).

Esse tipo de combinação integra as vantagens de cada componente e a contribuição de cada técnica de imageamento, em um único sistema nanoparticulado, tornando a nova nanossonda muito mais versátil. As vantagens de um sistema nanoparticulado, em particular, também visam a produção de sondas com elevada concentração de material paramagnético, podendo aumentar a relaxividade por partícula, cerca de 100 vezes mais. Dada a baixa sensibilidade da IRM, estratégias como essa favorecem as aplicações em imagem a nível molecular por amplificarem e otimizarem o sinal para RM (MERBACH; HELM; TÓTH, 2013). Dessa forma, seria possível diminuir a dosagem necessária do AC e mesmo assim se atingir um contraste adequado nas imagens por RM (PEREIRA; GERALDES, 2007).

Nesse contexto, os QDs, que são nanopartículas já aplicadas como sondas de imagem molecular por fluorescência, quando combinados a compostos paramagnéticos, agregam em uma única partícula a capacidade de possuir sinais para várias modalidades (isto é, óptica e magnética) (AIME et al., 2002; YI et al., 2005; JIN et al., 2008; STASIUK et al., 2011). Essa associação pode ser interessante, por exemplo, para estudos *in vivo*, focados na compreensão de processos biológicos, diagnóstico e orientação de procedimentos cirúrgicos, de maneira que a remoção de tecidos patológicos seja guiada por uma delimitação mais precisa, minimizando os danos aos tecidos saudáveis adjacentes (KIM etal., 2008; KIRCHER et al., 2003).

Além disso, a fluorescência dos QDs permite detectar alvos moleculares e celulares, em tempo real, com elevada sensibilidade. Devido a sua superfície ativa, a conjugação de vários ACs ao QD, pode contribuir para uma boa definição anatômica nas imagens obtidas, enquanto que a conjugação deles com biomoléculas fornece especificidade para o sistema nanoparticulado, possibilitando um direcionamento mais efetivo para locais de interesse (YANG; CHUANG, 2012, HARRISON et al.,2015).

De acordo com a maneira com que os QDs estão sendo relacionados com os íons paramagnéticos para construção dos sistemas bimodais, pode-se categorizá-los em: (A) QDs revestidos com moléculas contendo Gd (III); (B) encapsulação de QDs livres

juntamente com quelatos em nanoestruturas e (C) conjugação direta dos quelatos na superfície dos QDs, como esquematizado abaixo (Figura 17).

Figura 17 – Representação esquemática das classes de sistemas baseados em QDs e compostos paramagnéticos. Em: (A) QDs revestidos com moléculas, como lipídeos, contendo Gd (III); (B) encapsulação de QDs livres juntamente com quelatos de Gd (III) em nanoestruturas, que podem ser micelas ou lipídeos, e (C) conjugação direta dos quelatos na superfície dos QDs.

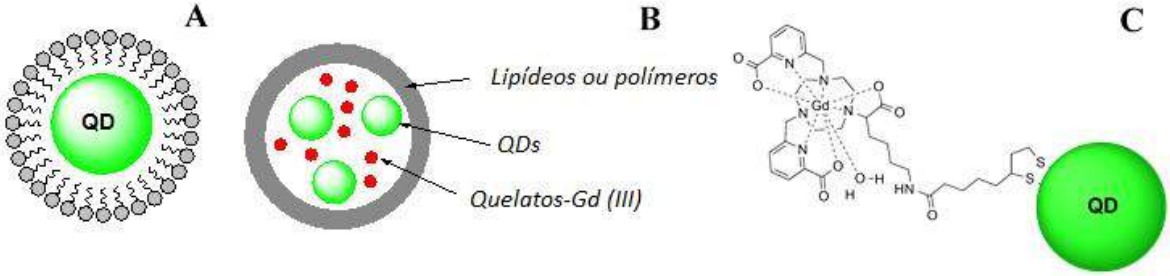

Fonte: PEREIRA, G. (2016).

A abordagem de conjugar diretamente os quelatos de Gd (III) na superfície dos QDs é uma das que vem sendo explorada pelos pesquisadores (STASIUK et al., 2011) e será abordada com mais detalhes na próxima seção. Visto que é com esse tipo de associação que estamos desenvolvendo nossos sistemas bimodais, por favorecer um processo crucial para eficiência da relaxividade, que é a troca da água entre a esfera interna e a esfera externa (*bulk*).

É possível conseguir um aumento do sinal para IRM por conjugação de vários ACs na superfície de cada nanopartícula de QD. Além de se objetivar um sistema bimodal que amplifique o sinal para IRM, também é preciso que essas sondas preservem e otimizem o sinal fluorescente dos QDs favorecendo análises com maior sensibilidade e acurácia de detecção. Para avaliar a eficiência desses sistemas bimodais nanoparticulados, avalia-se a relaxividade por cada íon, bem como por cada partícula de QD, que é um parâmetro exclusivo dessa abordagem. Ainda há poucos trabalhos nessa linha, e os que existem utilizam QDs sintetizados em meio hidrofóbico, e por isso necessitam de processos elaborados para torná-los hidrofílicos, os quais ainda podem diminuir consideravelmente a sua fluorescência (STASIUK et al., 2011). Isso demonstra a necessidade de mais trabalhos

envolvendo QDs sintetizados em meio aquoso, que não necessitem de etapas laboriosas de biocompatilização e que apresentem boa intensidade fluorescente, além de bom sinal para RM.

2.6.1 Conjugação direta dos quelatos na superfície dos QDs

Stasiuk e colaboradores utilizaram sondas de imagem bimodal por ligação covalente de quelatos de Gd (III) na superfície de QDs hidrofóbicos de Fosfeto de Índio funcionalizados com Sulfeto de Zinco (InP/ZnS), por troca de estabilizante (STASIUK et al., 2011). Os quelatos de Gd (III) foram preparados pela reação de derivados de *1,4,7*-triazaciclononano (TACN) e ácido lipóico. Os autores confirmaram a ligação de íons de Gd (III) na superfície dos QDs com base em medidas de susceptibilidade magnética e espectroscopia de UV-visível. Essa ligação dos quelatos aos QDs provocou aumento do diâmetro hidrodinâmico das nanopartículas de 6,9 a 8,6 nm, obtido a partir de medidas de DLS. Além disso, de acordo com os estudos fotofísicos, os quelatos não afetaram a luminescência dos QDs, mantendo o pico de emissão em torno de 620 nm, embora tenha sido constatada umasignificativa diminuição no rendimento quântico no processo de torná-los hidrofílicos. Por isso, o desenvolvimento de sistemas nanoparticulados é desafiador, pois devem manter as propriedades de ambos oscomponentes.

Ainda neste trabalho, os autores conjugaram um peptídeo de penetração celular (*maurocalcine*, MCa) aos QDs com quelatos-Gd (III), com o intuito de promover a internalização deste sistema QDs-Gd-MCa na célula e monitorar os eventos biológicos. Os sistemas foram incubados com células de ovário de hamster chinês (células CHO), durante 2 horas, para análise por microscopia confocal (Figura 18). Eles observaram o aparecimento de marcações pontuais dentro das células incubadas com QDs-Gd-MCa, sugerindo que eles foram internalizados em endossomos pelo mecanismo de endocitose (Figura 18 - E). Para definir os limites das células na microscopia, os autores marcaram a membrana plasmática, em vermelho, com rodamina conjugada a concanavalina A, que possui afinidade pelos carboidratos α-D-glicose e manose (Figura 18 – A, D). Em relação aos estudos de IRM, o sinal dos QDs-Gd-MCa, após 15 minutos de injetados em cérebro de rato, foi distinto quando comparado com o Dotarem®, mostrando que a sonda bimodal tem um elevado

tempo de retenção, além de manter a intensidade de sinal ainda mensurável após 4 horas (Figura 19).

Figura 18 – Imagem óptica de células CHO. As células foram incubadas com (A, D) rodamina-concanavalina A (em vermelho); (B) QDs-Gd (em verde); (E) QDs-Gd-MCa (em verde). Em C: sobreposição da imagem A e B. Em F: sobreposição da imagem D e E.

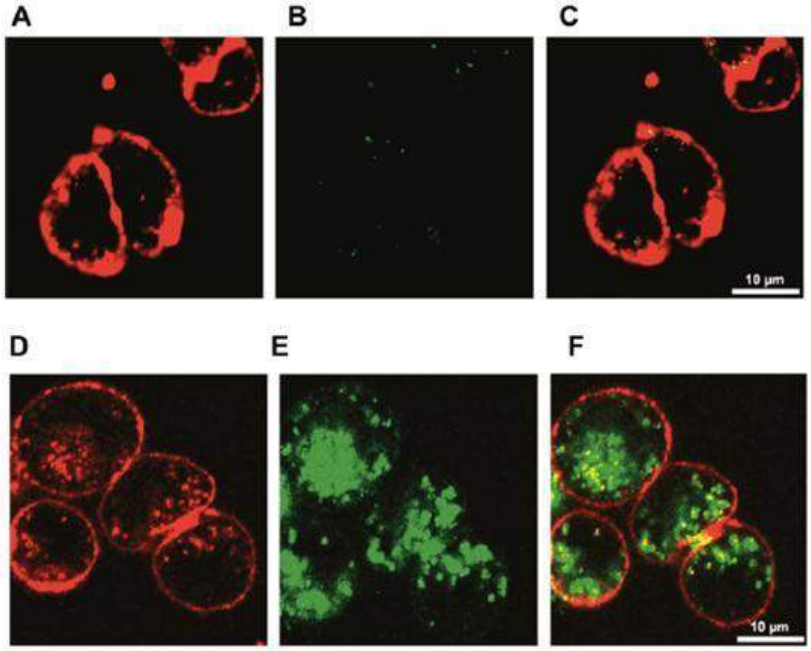

Fonte: Adaptada de STASIUK et al. (2011).

Figura 19 – IRM ponderadas em T_1 de cérebro de rato incubadas com (A) QDs-Gd-MCa e (B) com Dotarem®, depois de 15 min (esquerda) e depois de 4 h (direita). As imagens foram obtidas a 7 T. Adaptadas de Stasiuk et al. (2011).

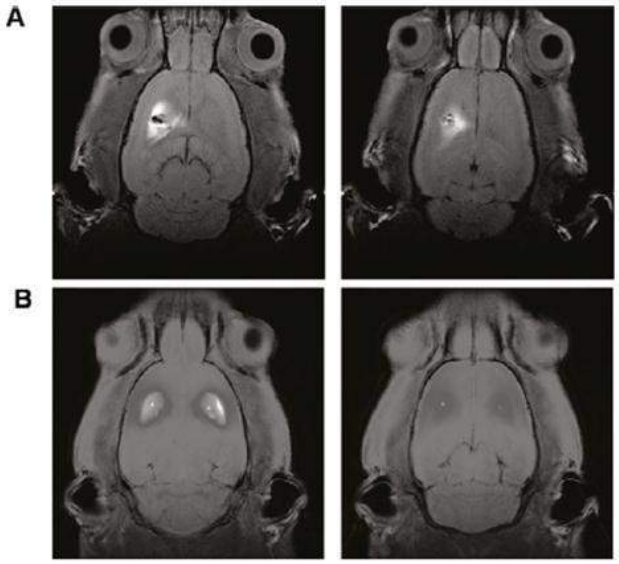

Fonte: Adaptada de STASIUK et al. (2011).

Nos sistemas nanoparticulados, em que os quelatos de Gd (III) estão ligados na superfície dos QDs, há uma restrição da rotação interna do complexo, favorecendo uma rápida troca de água coordenada com o centro do quelato, que é onde está localizado o íon Gd (III), e moléculas de água do *bulk* ao redor do complexo, resultando em aumento da relaxividade (HERMANN et al., 2008). Stasiuk e colaboradores obtiveram as seguintes medidas relaxométricas: r_1 por QD de 900 $mM^{-1}s^{-1}$ (a 0,81 T e 25º C) e r_1 por Gd (III) de 4,9 $mM^{-1}s^{-1}$ (a 0,81 T e 25º C) (STASIUK et al.,2011).

Com o intuito de otimizar a relaxividade de quelatos de Gd (III) conjugados aos QDs de InP/ZnS, os mesmos autores mencionados anteriormente, preparam três ligantes, como representados na Figura 20 abaixo.

Figura 20 – Esquema dos ligantes preparados por Stasiuk e colaboradores (STASIUK et al., 2013). Os ligantes referem-se a: ácido lipóico (L1), ácido mercaptopropiônico (L2) e ácido mercaptobenzóico (L3).

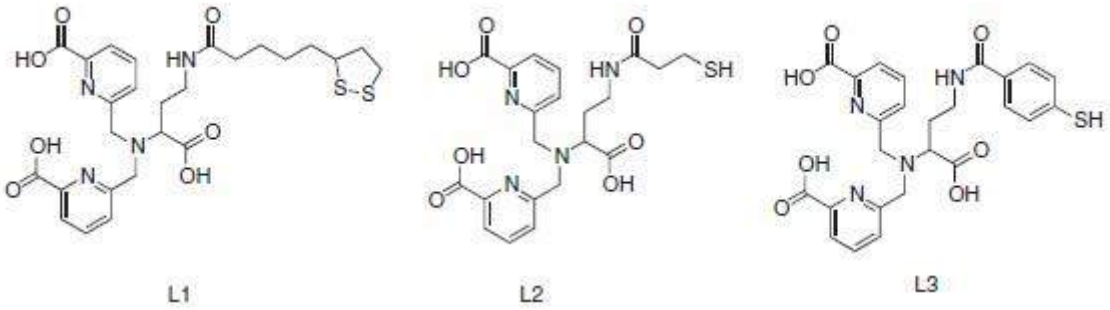

Fonte: PEREIRA, G. (2016)

Eles utilizaram “ligantes adaptadores” com diferentes graus de flexibilidades: ácido lipóico (L1), que tem um ditiol promovendo uma forte ligação com a superfície dos QDs; ácido mercaptopropiônico (L2), que provavelmente irá reduzir a mobilidade do complexo, devido a sua cadeia alifática ser mais curta; e ácido mercaptobenzóico (L3), que possui um sistema rígido que pode reduzir a rotação interna do complexo. Os QDs foram os mesmos do trabalho anterior (STASIUK et al., 2011), e essas novas associações não interferiram na fluorescência, quando os espectros de emissão foram comparados aos QDs já biocompatibilizados. Em relação às medidas relaxométricas, obtiveram os seguintes valores de r_1 por QD: 932, 342 e 487 $mM^{-1}s^{-1}$ (a 6,3 T e 25 ºC) para QDs-L1, QDs-L2 e QDs-L3,

respectivamente. E, por íon Gd (III): 8, 5 e 6,5 $mM^{-1}s^{-1}$ (a 6,3 T, 200 MHz e 25º C) para QDs-L1, QDs-L2 e QDs-L3, respectivamente (STASIUK et al., 2011).

De acordo com esses resultados de relaxometria obtidos por Stasiuk e colaboradores, os QDs-L3 apresentaram relaxividade mais elevada por íon e por partícula de QDs do que os demais sistemas. Isso porque a ligação entre os QDs e o complexo via ligante benzóico (L3) é mais rígida, diminuindo significativamente a rotação interna, e consequentemente, alterando a taxa de troca ($1/\tau_M$) de moléculas de água coordenadas, resultando em relaxividade mais elevada.

Outro importante fator que se deve considerar para a aplicação desse tipo de sonda em sistemas biológicos refere-se a alterações das propriedades quando estão em ambiente intracelular. Isso foi estudado por Starmans *et al*., que observaram que os p-QDs-RGD internalizados apresentaram relaxividade longitudinal (T_1) inferior, quando comparado com os mesmos sistemas em solução (STARMANS et al., 2011). Isto pode ter ocorrido em decorrência do mecanismo de endocitose, através do qual as células internalizaram o sistema bimodal em unidades de endossomos, aprisionando o AC e dificultando a troca de água por eles com o ambiente.

Nesse contexto, como nosso grupo de pesquisa tem experiência na área de nanotecnologia biomédica, desde a síntese dos QDs a aplicações deles em sistemas biológicos, a partir da versatilidade e visando as propriedades únicas dessas nanopartículas, nesse trabalho tivemos o intuito de desenvolver sistemas bimodais que promovam melhor resolução, contraste, especificidade bioquímica e multimodalidade a fim de aprimorar qualidade e funcionalidade de técnicas de baseadas em fluorescência e por IRM.

CAPÍTULO III

3. OBJETIVOS

3.1 Objetivo geral

Desenvolvimento de sistemas bimodais nanoparticulados baseados na conjugação direta de QDs de CdTe a quelatos de Gd (III) com potencialidades para aplicações como sondas para imagens óptica e magnética.

3.2 Objetivos específicos

- Sintetizar Quantum dots (QDs) de CdTe carboxilados, em meio aquoso, estabilizados e funcionalizados com AMS (ácido mercaptosuccínico);
- Caracterizar opticamente os QDs;
- Preparar e caracterizar quelatos paramagnéticos contendo íons gadolínio [Gd (III)] e DOTA como ligante;
- Desenvolver nanossistemas bimodais por ativação dos grupos carboxílicos dos QDs e conjugação direta a quelatos DOTA-Gd (III);
- Caracterizar óptica e relaxometricamente os nanossistemas bimodais para verificar as respectivas propriedades ópticas e paramagnéticas;
- Confirmar a conjugação dos nanossistemas bimodais por FCS (*Fluorescence Correlation Spectroscopy*);
- Avaliar a citotoxicidade dos nanossistemas bimodais após 24 h de incubação com células HeLa;
- Incubar os nanossistemas bimodais com células HeLa para analisar o seu potencial como sonda fluorescente através de análises por microscopia de fluorescência.

CAPÍTULO IV

Bimodal nanoparticulate contrast agents... (artigo para ser submetido ao *Journal Royal Society of Chemistry Advances)*

Artigo para ser submetido ao *Journal Royal Society of Chemistry Advances*

RSC Advances

ARTICLE

Bimodal nanoparticulate contrast agents based on CdTe Quantum dots and Gd (III)-DOTA chelates for optical and magnetic resonance imaging

Received 00th January 20xx,
Accepted 00th January 20xx

DOI: 10.1039/x0xx00000x

www.rsc.org/advances

M. I. A. Pereira,[1] P. E. Cabral Filho,[1] G. Pereira,[2] C. A. P. Monteiro,[1] G. M. Albuquerque,[1] B. S. Santos,[2] G. A. L. Pereira,[3] A. Fontes[1*]

Abstract: In a search for a better resolution, contrast, biochemical specificity and multimodality, the nanotechnology has been applied to develop efficient nanoprobes for improving the quality and functionality of imaging techniques. Magnetic resonance imaging (MRI) is a powerful diagnostic tool that enables distinguishing healthy from pathological tissues, with high anatomical details. However, MRI is limited for investigations of biochemical molecular and cellular events, which can be achieved by fluorescence techniques. Thus, in order to combine advantages of these both imaging tools, here, we developed a bimodal nanoparticle based on the direct conjugation of Gd (III)-chelates and hydrophilic CdTe quantum dots (QDs). Besides the bimodality, this nanoparticulate system can also help to improve the contrast and specificity in MRI, by increasing locally the paramagnetic chelate concentrations. QDs-Gd (III)-chelates showed chemical stability, bright fluorescence and effective relaxivities. By relaxometric measurements (at 7 T and 298 K), the nanosystem with 30 chelates was the most promising, presenting relaxivities of 535 and 103 $mM^{-1}.s^{-1}$ per QD and per ion, respectively. Moreover, bimodal nanoparticles labeled efficiently HeLa cells as showed the fluorescence microscopy and did not present significant cytotoxicity. Concluding, the nanosystems developed in this study showed to be potential probes for acquiring images by fluorescence and magnetic resonance, and useful for investigating a variety of biological process.

1. Introduction

The majority of diseases are multifactorial, which have motivated investigations related to the development of new tools, such as diagnosis methods and therapeutic procedures able to detect, distinguish and understand the various mechanisms, mainly at cellular and molecular levels, involved in each stage of diseases. While some researchers have explored and looked for specific biomarkers, others are focusing on designing novel tools to experimental and clinical imaging, hoping to contribute to the location, activity and dynamics of biological processes, preferably in real-time, associated with these biomarkers.[1]

Among the available imaging techniques, the one that is based on magnetic resonance imaging (MRI) has been widely used as a non-invasive diagnosis to discriminate healthy from pathological tissues with high anatomical details. However, in order to obtain a suitable distinction in MRI, the use of contrast agents (CAs) may be required, which can, for instance provide a white highlight in the images, by reducing the nuclear longitudinal relaxation time (T_1-weighted) of the surrounding water proton molecules. Commonly, T_1-weighted CAs are based on paramagnetic chelates, whose efficiency is determined in terms of the relaxivity r_1 ($mM^{-1}.s^{-1}$). However, even applying CAs, MRI is still limited for investigations of biochemical events, at molecular and cellular levels.[2]

In a search for a better resolution, contrast, biochemical specificity and multimodality, the nanotechnology has developed nanoprobes for improving the quality and functionality of imaging techniques. Various approaches have been applied aiming to design bimodal nanosystems, that can combine advantages of more than one imaging modality, being the association of MRI with fluorescence analyses one of the most intended, especially due to the resolution and the biochemical specificity of optical techniques. In this context, the quantum dots (QDs) have attracted the interest of nanomedicine, since they can be applied in the development of such bimodal nanoprobes. QDs are particular promising for this purpose, as they have unique properties, such as: (i) a high resistance to photodegradation, allowing to monitor real-time biological mechanisms and (ii) an active surface, which enables conjugation with several biomolecules, drugs, other nanoparticles, and also with paramagnetic compounds containing gadolinium ions [Gd (III)].[3–6]

Many studies have been conducted to develop bimodal nanosystems based on QDs associated with Gd (III) coordination compounds, by applying different strategies. Among them, the most exploited, are: coating QDs with molecules usually consisted of paramagnetic lipids containing Gd (III), and encapsulating QDs

[a] *Department of Biophysics and Radiobiology, Federal University of Pernambuco, Recife, PE, Brazil.*
E-mail: adriana.fontes.biofisica@gmail.com
[b] *Department of Pharmaceutical Sciences, Federal University of Pernambuco, Recife, PE, Brazil.*
[c] *Department of Fundamental Chemistry, Federal University of Pernambuco, Recife, PE, Brazil.*
Electronic Supplementary Information (ESI) available: details about xylenol orange test and Figures S1 and S2 for consult.

and bare Gd (III) chelates into a single nanoparticle, such as liposomes.[7–10] However, in general the bimodal nanoprobes, prepared by these strategies, display some limitations. For instance, they: (i) can be not so effective in reducing the T_1 relaxation time, mainly due to restricted water exchange processes, especially when encapsulated; (ii) can not present an proper nanometric size for biological applications; and/or (iii) can demand laborious procedures for their preparation. [7,11]

Thus, recently another strategy based on direct conjugation between QDs and Gd (III) chelates was reported.[5,12] Although there are still few studies of this nature in literature, this approach promises to maintain a smaller hydrodynamic diameter and favor an effective dynamic water exchange, between the bound water molecules and bulk water, without barriers, allowing to reach higher r_1 relaxivities. Stasiuk and collaborators, for example, have tested this approach and obtained nanosystems (*ca.* 10 nm) with bright fluorescence and improved relaxivity by using hydrophobic QDs and Gd (III) chelates, which were directly attached the Gd (III) chelates directly to the QDs' surface.[5]

In this context, here we report the development of a fluorescent paramagnetic nanoparticulate bimodal system based on hydrophilic CdTe QDs and Gd (III)-DOTA chelates through obtained covalent conjugation. We evaluated the coordination efficiency of the Gd (III) ions on the ligand by the xylenol orange method and the effective of conjugation process by using the fluorescence correlation spectroscopy (FCS). We also analyzed the nanosystems optical properties, as well as their cytotoxicity and their ability to label HeLa cells. Moreover, we determined the relaxivities of the bimodal nanoparticles per ion and per QD at 300 MHz and 298 K. We believe that the nanoprobes developed in this study are promising tools for acquiring images by fluorescence and magnetic resonance, in order to understand a variety of biological processes.

2. Experimental Section

2.1 Synthesis of CdTe-MSA QDs

Cadmium Telluride (CdTe) QDs were synthesized in an aqueous medium using the 3-mercaptossuccinic acid (MSA) as functionalizing/stabilizing agent in a molar ratio of 5:1:6 (Cd:Te:MSA) according to the method previously reported by some of us.[13] Briefly, metallic tellurium (0.1 mmol – Sigma-Aldrich) was reduced by reaction with sodium borohydride ($NaBH_4$ – 3 mmol – Sigma-Aldrich) at high pH > 10 and inert atmosphere (N_2). The Te^{2-} was added into a previously prepared solution of Cd^{2+}/MSA [0.5 mmol of cadmium chloride ($CdCl_2$ – Alfa Aesar) and 0.6 mmol of MSA (Sigma-Aldrich)] at pH ~ 10.5. After that, QDs suspension remained for 5 h under constant stirring at 90°C to form a colloidal dispersion of carboxyl-coated CdTe QDs.

2.2 Preparation of Gd (III) chelates

Gd (III) chelates were prepared using DOTA (1,4,7,10-tetraazaciclododecano-1,4,7,10-tetraacetic acid) as ligand and a gadolinium chloride solution ($GdCl_3 \bullet 6H_2O$– Alfa Aesar), with a 10% stoichiometric excess of ligand. Firstly, the pH of a DOTA ligand solution (10 µmol) was adjusted to 5.5 with NaOH, which was followed by the activation of one carboxyl group of each DOTA, using of N-ethyl-N'-(3-dimethylaminopropyl) carbodiimide hydrochloride (EDC – Sigma-Aldrich) and of N-hydroxysulfosuccinimide sodium salt (Sulfo-NHS – Sigma-Aldrich), both with final concentration of 0.01 M. After, the Gd (III) solution (9 µmol) was added to the ligand solution, remaining under overnight stirring at room temperature, obtaining the amine-reactive complex Gd (III)-DOTA-NHS.

2.3 Coordination efficiency evaluation by xylenol orange method

The coordination efficiency between Gd (III) and DOTA ligand was tested using the xylenol orange method proposed by Barge and colleagues.[14] This method was used to determine free Gd (III) ions by absorbance spectroscopy measurements (UV-Vis 1800 spectrophotometer - Shimadzu). As higher is the free gadolinium concentration, more displaced to the violet will be the color of the solution.[14] By the relation between the spectrophotometric changes of xylenol orange absorptions in the presence of different Gd (III) concentrations (Figure S1-Support Information), we obtained the calibration curve (Figure S2 – Support Information). The presence of free Gd ions in the complex was determined by using this calibration curve. Thus, for the evaluation of the coordination efficiency of the Gd (III) by the ligand, 10 µL of the chelate was added to 2 mL of a xylenol solution to detect free ions, in a final concentration of 25 µM de Gd (III).

2.4 Preparation of the bimodal nanosystems

The bimodal nanosystems based on QDs and Gd (III) chelates were obtained by covalent coupling. In order to obtain an improved bimodal system, we tested various molar ratio of QDs/Gd (III) chelates, from 10 to 100 Gd (III) chelates per QDs. The systems that remained visually stable, with bright fluorescence and without precipitation, were those that contained 1/10, 1/20 and 1/30 (CdTe QDs particles per Gd (III) chelates molecules). Therefore, only those systems were characterized and further studied by us. We prepared the systems, by adding the following volumes of each chemical compound [EDC (0.01 M), Sulfo-NHS (0.01 M), ethylenediamine (0.1 M) and Gd (III) chelate solutions (0.01 M)]: 3 µL to 1/10 system, 6µL to 1/20 system and 9 µL to 1/30 system, as schematized in Figure 1. Briefly, firstly, we adjusted the pH of 0.5 mL of carboxyl-coated CdTe QDs (3 µM) to approximately 5.5 using a MSA solution (4.9 % w/v). After, the respective aliquots of coupling agents, as described above, were added to obtain the QDs' NHS ester (CdTe-NHS). Then, the CdTe-NHS was reacted with the ethylenediamine and the Gd (III)-DOTA-NHS chelate, prepared previously as described in section 2.2, was added to the system.

2.5 QDs and bimodal systems optical characterization

Bare QDs and Gd (III)-DOTA-QDs were characterized by absorption and emission spectroscopy, by using, respectively, a UV-Vis 1800 spectrophotometer (Shimadzu) and a LS 55 spectrofluorometer (PerkinElmer, at λ_{exc} = 365 nm). These characterizations provide information about the QDs optical quality before and after conjugation with ethylenediamine and subsequently with Gd (III) chelates. We estimated the QDs' diameter (d) from the wavelength (λ) at the first peak of absorption spectrum and by applying of the Equation 1 below.[15]

$$d = \frac{(1.3845 - 0.00066\,\lambda)}{(1 - 0.00121\,\lambda)} \qquad \text{Eq.1}$$

By using the average d obtained above and the CdTe QDs' extinction coefficient (ε) by Yu et al. (2003) - Eq. 2, we estimated the QD concentration in the suspension by Lambert–Beer's law (Eq. 3).[16]

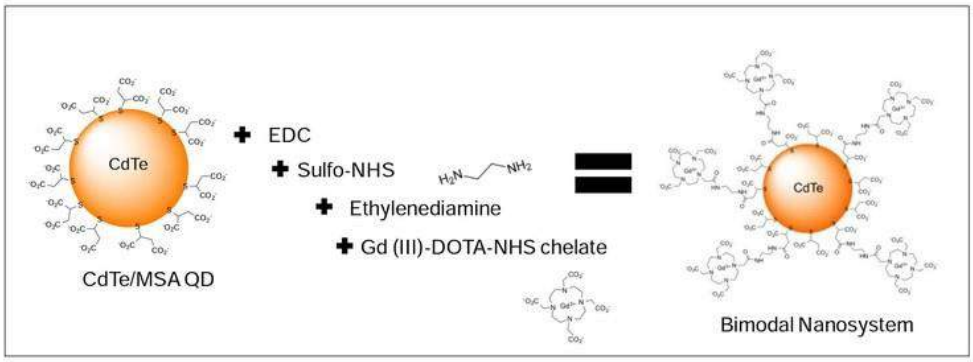

Fig. 1 Scheme of the conjugation process of the Gd (III)-DOTA-NHS chelates with the QDs via EDC, Sulfo-NHS, and ethylenediamine.

$$\varepsilon = 10043(d)^{2.12} \quad \text{Eq. 2}$$

$$A = \varepsilon CL \quad \text{Eq. 3}$$

where A is the absorbance at the first peak and L is the width of the cuvette or light path that is usually 1 cm.

Emission spectra were acquired in order to verify QDs' fluorescent properties before and after the conjugation. It was performed by using the same slits for all systems, in a pH of approximately 6.0.

2.6 Fluorescence correlation spectroscopy

The Fluorescence Correlation Spectroscopy (FCS) analysis was performed in a confocal microscopy (LSM 780, Carl Zeiss Meditec AG, Jena, Germany) by using 40× water immersion objective (NA = 1.0, WD = 2.5 mm) and pinhole aperture of 35 µm.[17] Correlation curves were obtained, at 514 nm excitation, for both bare QDs and bimodal systems. From the curves, we obtained the diffusion time (τ_D) for each sample and then the Eq. 4 was used to determine the hydrodynamic radius (R).

$$R = \frac{4\, k_B T\, \tau_D}{6\pi\eta\omega_x^2} \quad \text{Eq. 4}$$

where k_B is Boltzmann Constant, T is temperature of the sample under laser irradiation (we used T≈303 K), τ_D is diffusion time, η is medium viscosity (in this case, we used water η = 7.98×10−4 Pa•s) and ω_x is lateral radius of the focal volume (300 nm for excitation used here – 514 nm). FCS allows confirming the conjugation though the determination of R, since the τ_D is higher for conjugate sample when compared to bare QD.[17] Results were evaluated by statistical Wilcoxon test.

2.7 Relaxometric measurements

The relaxometric properties QDs-Gd (III) chelates bimodal nanosystems were also evaluated by measuring the proton water longitudinal relaxation (T_1) on a Varian Unity Plus spectrometer at high magnetic field (7 T, 298 K) and using an inversion recovery pulse sequence. Before the measurements, samples were purified by ultrafiltration columns of 10.000 MWCO (Vivaspin, GE Health), in order to eliminate any excess of free Gd (III) ions or even free DOTA-Gd (III) chelates. The Gd (III) concentrations of the systems were determined using by ICP-MS (NeXIon 300D).

Thus, the longitudinal relaxivities (r_1) of the bimodal systems were obtained by using T_1 and the Gd (III) concentration (mM), as described in Eq.5:

$$r_1 = \frac{R_1^{obs} - R_1^{dia}}{C} \quad \text{Eq. 5}$$

where C is the concentration of paramagnetic ion, R_1^{obs} is the longitudinal relaxation rate ($1/T_1$) of the water protons molecules in the presence of the paramagnetic ions and R_1^{dia} is the diamagnetic longitudinal relaxation rate ($1/T_1$) of the water protons (in the absence of the paramagnetic ions). The relaxivity indicates the efficiency of the contrast agent to decrease the relaxation time of water protons per unit of concentration (mM). In this study we calculated the relaxivity per ion Gd (III) and per QD.

2.8 Cells culture

HeLa cells (human epithelial cervical carcinoma) were obtained from ATCC (American Type Culture Collection, Manassas, VA, USA) and cultured in Dulbecco's modified Eagle's medium (DMEM – Sigma-Aldrich) supplemented with fetal bovine serum (FBS - Gibco), streptomycin and penicillin (Sigma-Aldrich) in humidified atmosphere with 5% CO_2 at 37 °C. When reaching 90% confluence, cells were detached with 0.25% of trypsin (Sigma-Aldrich) and followed by neutralization with DMEM.

2.9 Fluorescence microscopy analysis

The non-specific labeling of the HeLa cells by the bimodal nanosystems was studied by fluorescence microscopy. For this, we seeded 3 x 10^4 cells/well in a 4-wells plate (Greiner Bio-One, Germany) and incubated them for 24 h. After this time, the cells were washed and incubated in the following conditions: (I) control cells and (II) cells with QDs-Gd (III) chelates bimodal nanosystems at 100 nM for 1 h (at 37 °C and 5% CO_2). After the incubation, cells were washed with PBS three times.

Cells were analyzed in a conventional fluorescence microscope (Leica DMI4000B) using the excitation filter BP 560/40 nm and the emission filter in BP 645/75 nm to evaluate the labeling of HeLa cells by the bimodal QDs-Gd (III) chelates systems. Moreover, the excitation filter BP 360 nm/40 nm and the emission filter BP 470/40 nm were applied to display the cell nuclei stained by DAPI (4',6-Diamidino-2-Phenylindole, Dihydrochloride – Life Technologies). For this, cells were incubated for 5 min at a final concentration of 1 μg•mL−1.[13]

2.10 Resazurin viability assay

Cell viability was also evaluated for QDs, Gd (III) chelates and bimodal QDs-Gd (III) chelates systems at concentrations of 1000 nM, 500 nM, 250 nM, 125 nM and 62.5 nM in triplicate. For the negative control was used PBS (50% v/v in DMEM) since all nanosystems were diluted in PBS. On the other hand, for positive controls, cells were incubated with dimethyl sulfoxide (DMSO - 20% v/v in DMEM) to validate the test. For this, we seeded 5 x 10^4 cells/well in a 24-wells plate (Greiner Bio-One, Brazil) and incubated them for 24 h. After 24 h, the wells were washed and the cells were incubated for more 24h with the samples at 37 °C. The cell activity was revealed using the resazurin reduction obtained after approximately 40 min of incubation.[18] For this, the supernatant was removed, the wells were washed and the amount of 10 mg•mL^{-1} of the resazurin was added to the wells. Finally, after 40 min of incubation, the supernatant was added in a 96-weels plate to measure the absorbance of resorufin at 570 nm and of the resazurin at 600 nm in a μQuant™ microplate spectrophotometer (BioTek, Inc.) equipped with Gen5 2.06 software. Results were evaluated by statistical Wilcoxon test. The cell viability was calculated using the equation 6:

$$cell\ viability\ (\%) = \frac{(A_{570}-A_{600})\ treated\ cells}{(A_{570}-A_{600})\ control\ cells} x\ 100 \quad \text{Eq. 6}$$

3. Results and Discussion

3.1 Optical characterization of QDs and QDs-Gd (III) chelates bimodal nanosystems

According to the absorption spectrum, QDs showed a typical profile with a first absorption peak at 575 nm, as can be seen in Figure 2. The average diameter estimated for these nanocrystals was about 3.3 nm and the QDs concentration was estimated as 6 μM, that corresponds to 4.5 x 10^{14} nanoparticles·mL^{-1}.[15,16,19]

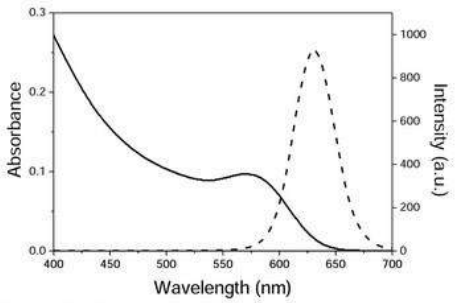

Fig. 2 CdTe QDs optical characterizations: absorption (full line) and emission spectra (dashed line). The emission spectrum was acquired at λ_{exc}= 365 nm.

Furthermore, QDs showed a maximum emission in the orange region around 612 nm with a usual full width at a half maximum (FWHM) of *ca.* 53 nm (Figure 2).

We also characterized the QDs after the conjugation with Gd (III) chelates, in order to evaluate the effects of the conjugation process on their optical properties. The bimodal nanoparticles absorption spectra did not change compared to the one obtained for bare QDs.

Also, the emission spectra for all QDs-Gd (III) chelates bimodal nanosystems presented an average red shift of approximately 14 nm. The bimodal nanosystems also presented a slightly narrower FWHM, showing an average value of *ca.* 43 nm. Thus, both of these behaviors suggest that some modifications occur on the QD surface due to the conjugation process. Moreover, the bimodal nanoparticles remained with a bright fluorescence, as can be observed in Figure 3 and in the respective inset. Therefore, these results showed that the conjugation process does not affect QDs optical properties, making them potential luminescent probes.

3.2 Coordination efficiency evaluation by xylenol orange method

According to Xylenol test, the absorbance ratio between the peaks at 577 and 434.5 nm, with known concentrations, originate the calibration curve (Figure S1 – Support Information), which allowed us to quantify the free gadolinium ions.[14] According to the calibration curve (r^2 = 0.9958), we found the amount of 0.6 μM of free Gd (III) in the solution of Gd (III) chelates, which corresponds to 2.4% of the total Gd (III) added (25 μM). Thus, nearly 97.6% of gadolinium ion was successfully incorporated by the DOTA-NHS ligand.

3.3 Relaxometric characterization

The measurements for the longitudinal relaxation time (T_1) of the bimodal nanosystems QDs-Gd (III) chelates, in milliseconds (ms), were: 1995 (1/10), 1395 (1/20) and 1069 (1/30), as shown in Table 1. From T_1 values, we obtained the relaxivities per Gd (III) and per QD, which are also presented in Table 1. The percentage of Gd (III) ions, determined by ICP (Table 1), that remained coordinated to the ligands onto the QDs surface, was of approximately: 16% (1/10), 22% (1/20) and 18% (1/30) of the initial Gd (III) amount added in each one of the systems.

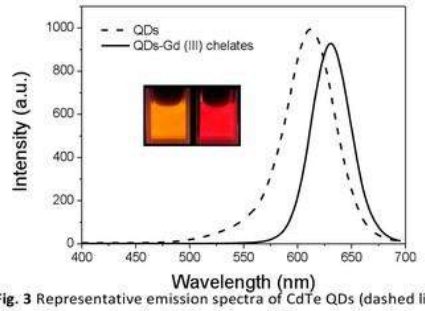

Fig. 3 Representative emission spectra of CdTe QDs (dashed line) and a bimodal nanosystem(solid line), λ_{exc}= 365 nm. In the pictures (inset), we can observe the bright fluorescence of bare QDs (in orange) and of a bimodal nanosystem (in red), under lamp UV excitation at 365 nm.

Table 1 Values of longitudinal water proton relaxation times (T_1) at 7 T and 298 K, concentrations of Gd (III) and the respective relaxivities given per QDs and per Gd (III).

QDs-Gd (III) chelates	T_1 (ms)	Concentration of Gd (III) (x 10^{-3} mM)	Relaxivity per QDs ($mM^{-1}.s^{-1}$)	Relaxivity per Gd (III) ($mM^{-1}.s^{-1}$)
1/10	1995	1.5	101	68
1/20	1395	4.0	317	78
1/30	1069	5.2	535	103

*An error of *ca*. 10% was evaluated for the measurements of the T_1. The concentration of Gd (III) was obtained by ICP, as described in the Experimental Procedure section. The final QDs concentration, obtained by the absorption spectrum, was of 1 mM in all the systems.

From Table 1, the best relaxivities, at 300 MHz, were obtained by the 1/30 system, which were 535 $mM^{-1}.s^{-1}$ per QD and 103 $mM^{-1}.s^{-1}$ per paramagnetic ion. Moreover, as expected, all the values of r_1 per QD for the bimodal nanosystems, schematized in Figure 1, were better than those ones obtained by the bare chelate, at the same magnetic field, *ca*.2 $mM^{-1}.s^{-1}$.

It is important to remember that the search for more effective contrast agents involves the optimization of various parameters governing the relaxivity. Since the relation between the molecular structure and the electronic relaxation is not well known, particularly concerning to the inner sphere proton relaxivity (r_1), this task is focused on the optimization of three parameters, which are the number of water molecules coordinated to the metal ion (q), the exchange lifetime (τ_M) and the re-orientational correlation time (τ_R).[20] Thus, all the approaches used by researches until now, are dedicated mainly to reduce the mobility (and then increasing τ_R) of paramagnetic chelates, by attaching them to nanoparticles that, at least, are of one order of magnitude higher than the molecular systems. Consequently, the exchange rate ($1/\tau_M$) between water molecules bound to Gd (III) and bulk water molecules is also affected.

Some works have prepared bimodal systems based on QDs conjugated to paramagnetic chelates in a search to reach better relaxivities in comparison to the molecular CAs used clinically, in order to reduce the applied dosage and improve the image contrast. Stasiuk et al. (2011) have prepared a system through direct covalent attachment of DPAA-Gd (III) chelates onto InP/ZnS-QDs.[12] Our value of r_1 per QD for the 1/30 system (535 $mM^{-1}.s^{-1}$, 300 MHz, 7 T) was higher when compared to the bimodal system developed initially by them, which was 200 $mM^{-1}.s^{-1}$ at 200 MHz (4.7 T). However, these same authors optimized their systems in 2013, through a restriction of the internal chelate rotation by using QD linkers of different flexibility and thus obtaining an r_1, per QDs, of 932 $mM^{-1}.s^{-1}$.[5] Nevertheless, our value of r_1 per Gd (III) of our system 1/30, 103 $mM^{-1}.s^{-1}$ at 300 MHz, are still higher than the 8$mM^{-1}.s^{-1}$ obtained by them at 200 MHz. Furthermore, they used hydrophobic QDs that require post-synthesis procedures to reach the hydrophilicity necessary to work with biological systems. In our case, QDs were prepared in aqueous medium, and they can be functionalized with the paramagnetic chelate, without previously surface modification.

Besides direct conjugation strategy, other approaches have been reported to develop bimodal systems consisted of QDs and paramagnetic ions: (1) by coating the QDs with molecules, such as lipids or polymers, containing Gd (III), and (2) by encapsulating various free QDs together with paramagnetic chelates into a single nanostructure.[10,21] However, the direct conjugation approach can be particularly advantageous compared to the others, mainly because paramagnetic chelates are attached on the QDs surface. It allows a direct access to the bulk water molecules and thus, facilitates the water exchange between them and the water molecule(s) bound to Gd (III), without any barrier that could hinders this mechanism. Additionally, the conjugation is a practical and simple approach that does not change considerably the size of the bimodal nanoparticle compared to QDs, which is more interesting for biological applications. A hydrodynamic diameter smaller than *ca*. 10 nm is crucial to decrease in vivo toxicity, since nanoparticles will be more easily eliminated by renal clearance.[11]

According to these relaxometric measurements, our bimodal nanosystems are promising T_1-weighting CAs and have the potential to improve images of clinical interest by MRI.

3.3 FCS results

According to correlation curves shown in Figure 4, the average diffusion times (τ_D) were calculated as approximately 124 µs for bare QDs and 242 µs for the 1/30 bimodal nanosystem. We choose to evaluate this bimodal system, since it presented the best relaxivity compared to the others. Using these results and applying the Eq. 4, we obtained the hydrodynamic diameter of the samples (Table 2): *ca*.3 nm for bare QDs and *ca*.6 nm for the bimodal nanosystem. These results were statistically significant with $p < 0.0001$. Thus, FCS analysis indicates that QDs were conjugated with Gd (III) chelates.

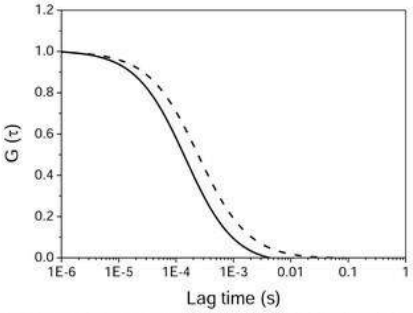

Fig. 4 FCS correlation curves of bare QDs (solid line) and the bimodal nanosystem (dashed line).

Table 2 Data from FCS: diffusion times and hydrodynamic diameters.

Sample	Diffusion time (μs)	Hydrodynamic diameter (nm)
Control	**124.4 ± 10.7**	**3.1 ± 0.3**
Bimodal Nanosystem	**241.9 ± 22.1**	**6.0 ± 0.5**

3.4 Biological interaction of the bimodal systems

3.4.1 Resazurin viability assay

The resazurin assay, offered us a simple and sensitive cytotoxicity evaluation of the bimodal nanosystems based on QDs and Gd (III) chelates, applied to HeLa cells. We used HeLa cells as concept proof, since they are frequently used as model in studies related to cancer, which also is one of the principal targets motivating the development of bimodal nanosystems.[13] This test indicates that the cells are metabolically active, being capable of reducing the resazurin (oxidized form) to resorufin (reduced form). We found that the bimodal systems developed by us present low toxicity, as can be observed by the relative percentage of cell viability in Figure 5: 84.7 ± 4.5% [1000 nM of QDs-Gd (III) chelates] to 96.3 ± 4.3% (62.5 nM). The maxima concentration tested in the viability assay was ten times higher (1000 nM) that one applied in the labeling procedure (100 nM) and it was not sufficient to induce cytotoxic effects on cells.

Su et al. (2010) also studied toxicity of CdTe QDs by MTT assay in the concentrations up to 300 nM, which showed to be toxic for HEK293 cells. Even testing higher concentrations than the authors above, our results showed that the cells remained viable. We believe that the purification performed with the ultrafiltration tubes was an important step to reach this result, since decreases the excess of reagents from the synthesis and conjugation. In the viability assays that evaluate directly the cells, such as MTT, the optical properties of the internalized QDs can interfere in the viability data, leading to false positive results, principally at high concentrations of QDs.[22] This is one of the reasons through which we choose to use the resazurin assay, as alternative in order to eliminate the interferences of the QDs' optical properties, since it uses the supernatant without QDs for the analysis.

3.4.2 Fluorescence microscopy

According to the conventional fluorescence microscopy, bimodal nanosystems labeled efficiently HeLa cells by unspecific interaction, as we can seein Figure 6 (B, C). Probably, this labeling was due to the QDs carboxylic groups activated by NHS esters, which allow the interaction of these nanoparticles with the amine groups of the membrane proteins and/or to the QDs endocytosis by the cells. We observed that all systems (1/10, 1/20 and 1/30) presented a similar labeling profile. Therefore, these systems were able to label the cells efficiently, presenting a bright optical signal, indicating that our nanosystems can be used as probes for optical imaging.

Conclusions

As conclusion, we developed a fluorescent/paramagnetic bimodal nanosystem through direct conjugation of Gd (III)-DOTA chelates on hydrophilic CdTe QDs' surfaces, without requiring laborious procedures to make these nanoparticles more biocompatible. Our best nanosystem, prepared with 30 Gd (III)-DOTA, presented a hydrodynamic diameter of ca. 6 nm and effective longitudinal relaxivities (r_1, 7 T, 298 K) of 535 and 103 $mM^{-1}.s^{-1}$ per QD and per ion, respectively, suitable for acquiring T1-weighted MR images. Besides, all bifunctional nanoparticles preserved a bright fluorescence, labeling efficiently HeLa cells, practically without any toxicity in a 24 h assay. Thus, our systems can be considered as promising bimodal nanoprobes, versatile to be conjugated to biomolecules with different specificities, enabling a variety of biological studies at molecular and cellular levels by fluorescence and magnetic resonance.

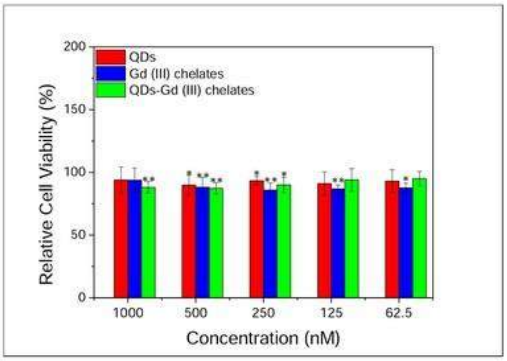

Fig. 5 Relative cell viability analysis using the resazurin assay. HeLa cells remained viable after being incubated with 62.5 nM to 1000 nM of: bare QDs, bare Gd (III) chelates and QDs-Gd (III) chelates. Results were statistically significant with $p < 0.05$ (*) and $p < 0.01$ (**).

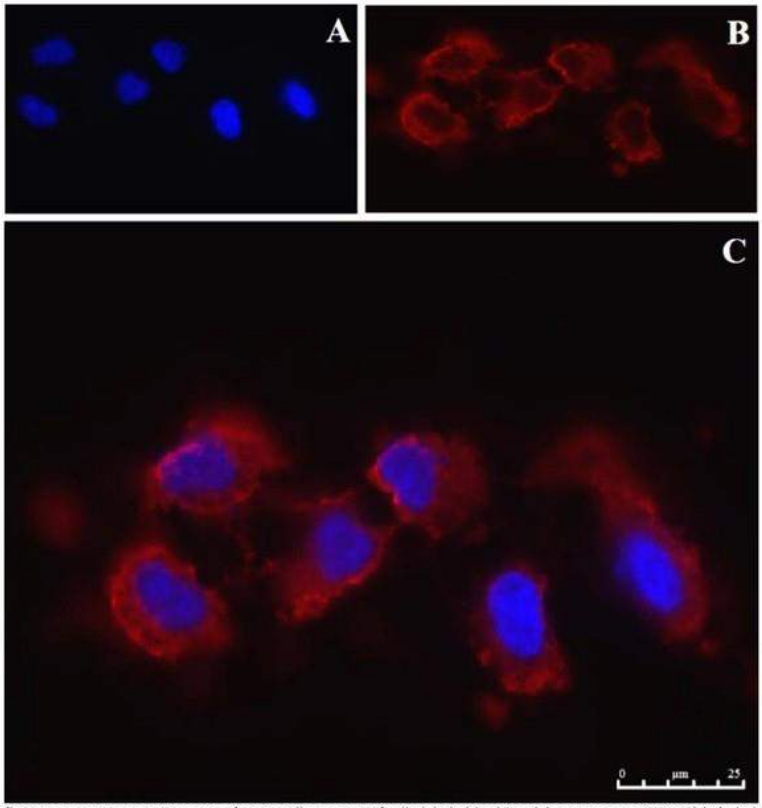

Fig. 6 Conventional fluorescence microscopy images of HeLa cells non-specifically labeled by bimodal nanosystems QDs-Gd (III) chelates. (A) cells nuclei stained in blue by DAPI, (B) cells labeled by QDs- Gd (III) chelates in red and (C) merge of the previous images (B and A). Scale Bar: 25 μm.

Acknowledgements

The authors acknowledge the financial support from Brazilian agencies FACEPE, CNPq and the staff of the Regional Center for Nuclear Sciences for the ICP-MS analysis.

Notes and references

1 R. Weissleder and M. J. Pittet, *Nature*, 2008, **452**, 580–589.
2 H. Shokrollahi, *Mater. Sci. Eng. C. Mater. Biol. Appl.*, 2013, **33**, 4485–97.
3 W. J. M. Mulder, G. J. Strijkers, K. Nicolay and A. W. Griffioen, *Angiogenesis*, 2010, **13**, 131–4.
4 C. E. Probst, P. Zrazhevskiy, V. Bagalkot and X. Gao, *Adv. Drug Deliv. Rev.*, 2013, **65**, 703–18.
5 G. J. Stasiuk, S. Tamang, D. Imbert, C. Gateau, P. Reiss, P. Fries and M. Mazzanti, *Dalt. Trans.*, 2013, **42**, 8197–200.
6 B. a Kairdolf, A. M. Smith, T. H. Stokes, M. D. Wang, A. N. Young and S. Nie, *Annu. Rev. Anal. Chem.*, 2013, **6**, 143–162.
7 K. B. Ghaghanda, M. Ravoori, D. Sabapathy, J. Bankson, V. Kundra and A. Annapraganda, *PLoS One*, 2009, **4**, e7628.
8 L. Liu, W.-C. Law, K.-T. Yong, I. Roy, H. Ding, F. Erogbogbo, X. Zhang and P. N. Prasad, *Analyst*, 2011, **136**, 1881–6.
9 W. J. M. Mulder, R. Koole, R. J. Brandwijk, G. Storm, P. T. K. Chin and G. J. Strijkers, 2006, 1–6.
10 W. B. Tan and Y. Zhang, *Adv. Mater.*, 2005, **17**, 2375–2380.
11 H. S. Choi, W. Liu, P. Misra, E. Tanaka, J. P. Zimmer, B. Itty Ipe, M. G. Bawendi and J. V Frangioni, *Nat. Biotechnol.*, 2007, **25**, 1165–1170.
12 G. J. Stasiuk, S. Tamang, D. Imbert, C. Poillot, M. Giardiello, E. L. Barbier, P. H. Fries, M. De Waard, P. Reiss and M. Mazzanti, 2011, 8193–8201.
13 P. E. Cabral Filho, A. L. C. Cardoso, M. I. A. Pereira, A. P. M. Ramos, F. Hallwass, M. M. C. A. Castro, C. F. G. C. Geraldes, B. S. Santos, M. C. Pedroso de Lima, G. A. L. Pereira and A.

Support information (Journal Royal Society of Chemistry Advances)

The xylenol orange solution is yellow either in the acid or neutral pH, and when the pH becomes basic, its color changes to violet. This effect is due to deprotonation of the phenolic hydroxyl group, which also occurs in the presence of coordination metals, such as the Gd (III). As consequence a shift of the absorption wavelength to higher values is observed in the presence of free Gd (III) and the solution becomes violet.[1]

Briefly, it was prepared an acetate buffer solution (250 mL), the pH was adjusted to 5.8 with NaOH (2 M) and the xylenol orange (3 mg) was dissolved. The spectrophotometric changes of xylenol orange absorptions observed in the Figure S1 was recorded by using xylenol orange and $GdCl_3$ solutions (0.001 M) in the following Gd (III) concentrations: 0, 0.1, 0.5, 1, 1.5, 2, 2.5 and 3 µM. By relating the maxima of these absorbance profiles in the presence of different concentrations of Gd (III), we obtained the calibration curve (Figure S2). Free Gd ions in solution were determined using this calibration curve. The acetate buffer solution was used as the reference in the analysis.

Fig.1 SI - Determination of free Gd (III) by xylenol orange. With the increase of the amount of free gadolinium, there is a decrease in the intensity of the peak 434.5 nm and increase of the 577 nm. Spectra were recorded by using an acetic buffer solution at pH 5.8 in the presence of 0, 0.5, 1, 1.5, 2, 2.5 and 3 µM of Gd (III).

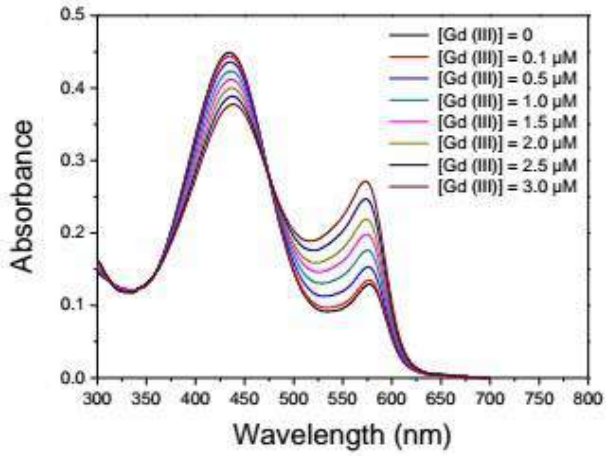

Fig.2 SI - Calibration curve obtained by spectrophotometric changes of xylenol orange absorptions in the presence of different concentration of Gd (III).

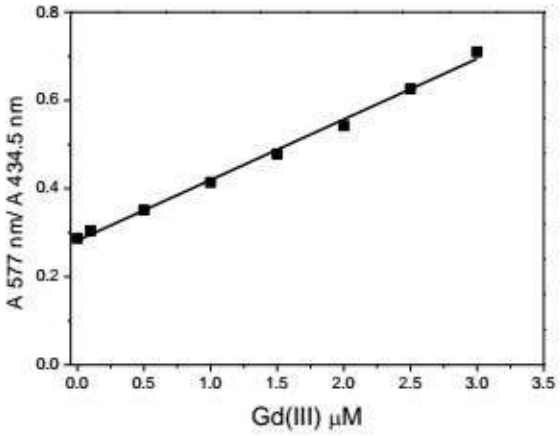

References

[1] A. Barge, G. Cravotto, E. Gianolio and F. Fedeli, 2006, 188, 184–188.

CAPÍTULO V

5. CONCLUSÕES

A partir do desenvolvimento desse trabalho, obtivemos as seguintes conclusões:

• Os QDs sintetizados apresentaram espectro de absorção característico e a partir do seu primeiro máximo, verificamos um diâmetro médio de aproximadamente 3,3 nm para esses nanocristais. Os espectros de emissão indicaram boa intensidade de fluorescência na região espectral do laranja em 614 nm;

• De acordo com o teste do Xylenol Orange, mais de 97% dos íons Gd (III) foram eficientemente coordenados ao ligante DOTA-NHS;

• Os nanossistemas bimodais, preparados com 10, 20 e 30 quelatos de Gd (III) por QD, apresentaram-se como suspensões estáveis, sem precipitação e aglomerados e mantiveram uma boa intensidade de fluorescência, semelhante à dos QDs sozinhos, com um red shift de aproximadamente 14 nm;

• Através das medidas relaxométricas (7 T, 25 °C) todos os sistemas levaram a diminuições nos tempos de relaxação longitudinal (T_1), sendo o sistema preparado com 30 quelatos por QD o mais eficiente, apresentando relaxividade (r_1) de 535 e 103 mM^{-1} $.s^{-1}$ por QD e por íon Gd (III), respectivamente;

• Medidas de FCS confirmaram que houve a conjugação para o melhor sistema obtido, que foi preparado com 30 quelatos de Gd (III) por QD. Esse sistema bimodal apresentou um tamanho médio de *ca*. 6 nm;

• Após 24 h de incubação com células tumorais HeLa, os nanossistemas não apresentaram citotoxicidade significativa e marcaram essas células inespecificamente.

6. PERSPECTIVAS

Temos como perspectivas desse trabalho:

• Otimização da relaxividade (r_1) por nanopartícula e por íon Gd (III) dos nanossistemas bimodais por meio de análises relaxométricas, a 20 e 60 MHz.

• Verificar os efeitos dos nanossistemas sob o tempo de relaxação transversal (T_2).

• Estudar o efeito da relaxividade em função do campo magnético, por meio de curvas de NMRD (nuclear magnetic resonance dispersion) de modo a se obter informações sobre quais dos parâmetros (τ_M, τ_D e τ_R) que dominam os mecanismos associados à relaxação paramagnética.

• Conjugar os nanossistemas com biomoléculas, como transferrina e ácido fólico, para estudar a dinâmica de receptores em células cancerígenas por fluorescência e ressonância magnética nuclear.

• Assim, os nanossistemas bimodais desenvolvidos nesse trabalho apresentam-se como sondas promissoras para estudos a nível molecular e celular por meio de análises baseadas em fluorescência e ressonância magnética nuclear.

• Como os nanossistemas são versáteis podemos testar a metodologia com outros ligantes, QDs com diferentes comprimentos de onda emissão, para marcações múltiplas, bem como conjugar biomoléculas com diferentes especificidades bioquímicas, a fim de desenvolver sistemas mais eficientes quanto às suas propriedades ópticas e magnéticas, com ampla aplicabilidade na biologia.

REFERÊNCIAS

ACCARDO, A. et al. Physicochemical properties of mixed micellar aggregates containing CCK peptides and Gd complexes designed as tumor specific contrast agents in MRI. *Journal of the American Chemical Society*, v. 126, p. 3097 – 107, 2004.

AIME, S.; BOTTA, M.; TERRENO, E. Gd(III)-based contrast agents for MRI. *Advances in Inorganic Chemistry*, v. 57, n. 5, p. 173 – 237, 2005.

AIME, S. et al. Insights into the use of paramagnetic Gd(III) complexes in MR-molecular imaging investigations. Journal of magnetic resonance imaging. *JMRI*, v. 16, p. 394 – 406, 2002.

ANDRADE, C. G. et al. Evaluation of glycophenotype in breast cancer by quantum dot-lectin histochemistry. *International journal of nanomedicine*, v. 8, p. 4623 – 9, 2013.

BHUJWALLA, Z. M. et al. Reduction of vascular and permeable regions in solid tumors detected by macromolecular contrast magnetic resonance imaging after treatment with antiangiogenic agent TNP-470. *Clinical cancer research: an official journal of the American Association for Cancer Research*, v. 9, p. 355 – 62, 2003.

BLOCH, F.; HANSEN, W. W.; PACKARD, M. The Nuclear Induction Experiment. *Phys. Rev*., v. 70, 1946.

BLOEMBERGEN, N.; MORGAN, L. O. Proton Relaxation Times in Paramagnetic Solutions. Effects of Electron Spin Relaxation. *J. Chem. Phys*., v. 34, p. 842 – 842, 1961.

BRUS, L. E. Electron–electron and electronhole interactions in small semiconductor crystallites: The size dependence of the lowest excited electronic state. *J. Chem. Phys*., v. 80, p. 4403 – 4403, 1984.

BULLMORE, E. The future of functional MRI in clinical medicine. *Neuroimage*, v. 62, n. 2, p. 1267 – 71, 2012.

BUXTON, R. B. Introduction to Functional Magnetic Resonance Imaging: Principles and Techniques. 2002.

CABRAL FILHO, P. E. et al. CdTe quantum dots as fluorescent probes to study transferrin receptors in glioblastoma cells. *Biochimica et biophysica acta*, v. 1860, p. 28 – 35, 2015.

CARAVAN, P. et al. Gadolinium(III) Chelates as MRI Contrast Agents: Structure, Dynamics, and Applications. *Chemical reviews*, v. 99, p. 2293 – 352, 2001.

CARVALHO, K. H. G. et al. Fluorescence plate reader for quantum dot-protein bioconjugation analysis. *Journal of nanoscience and nanotechnology*, v. 14, p. 3320 – 7, 2014.

CHOI, H. S. et al. Renal clearance of quantum dots. *Nature biotechnology*, v. 25, p. 1165 – 70, 2007.

CORSI, D. M. et al. Determination of paramagnetic lanthanide(III) concentrations from bulk magnetic susceptibility shifts in NMR spectra. *Magnetic Resonance in Chemistry*, v. 39, n. 11, p. 723 – 726, 2001.

DAMADIAN, R. Tumor detection by nuclear magnetic resonance. *Science* (New York, N.Y.), v. 171, p. 1151 – 3, 1971.

ELIAS JUNIOR, J. et al. Complicações do uso intravenoso de agentes de contraste à base de gadolínio para ressonância magnética. Radiologia Brasileira, *Scielo*, v. 41, p. 263 – 267, 2008. ISSN 0100-3984.

ESTEVE-TURRILLAS, F. A.; ABAD-FUENTES, A. Applications of quantum dots as probes in immunosensing of small-sized analytes. *Biosensors & bioelectronics*, v. 41, p. 12 – 29, 2012.

FONTES, A. et al. Quantum Dots in Biomedical Research. *Biomedical Engineering - Technical Applications in Medicine*, Cap. 2, InTech, 2012.

FREED, J. H. Dynamic effects of pair correlation functions on spin relaxation by translational diffusion in liquids. II. Finite jumps and independent T_1 processes. *J. Chem. Phys.*, v. 68, p. 4034 – 4037, 1978.

GHAGHADA, K. B. et al. New dual mode gadolinium nanoparticle contrast agent for magnetic resonance imaging. *PloS one*, v. 4, p. e7628 – None, 2009.

GIEPMANS, B. N. G. et al. The fluorescent toolbox for assessing protein location and function. *Science* (New York, N.Y.), v. 312, p. 217 – 24, 2006.

GONZALEZ, G. et al. Water-Exchange, Electronic Relaxation, and Rotational Dynamics of the MRI Contrast Agent [Gd(Dtpa-Bma)(H2O)] in Aqueous-Solution - a Variable-Pressure, Temperature, and Magnetic-Field O-17 NMR-Study. *J. Phys. Chem.*, v. 98, n. 1, p. 53 – 59, 1994.

GOSSUIN, Y. et al. Magnetic resonance relaxation properties of superparamagnetic particles. Wiley interdisciplinary reviews. *Nanomedicine and nanobiotechnology*, v. 1, p. 299 – 310, 2010.

HAËN, C. de. Conception of the first magnetic resonance imaging contrast agents: a brief history. v. 12, n. 4, p. 221 – 230, 2001.

HERMANN, P. et al. Gadolinium(III) complexes as MRI contrast agents: ligand design and properties of the complexes. *Dalton transactions* (Cambridge, England : 2003), p. 3027 – 47, 2008.

HERMANSON, G. T. Zero-Length Crosslinkers. Bioconjugate techniques. *Elsevier*, p. 213 – 233, 2008.

HINES, M. A.; GUYOT-SIONNEST, P. Synthesis and characterization of strongly luminescing ZnS-capped CdSe nanocrystals. *J. Phys. Chem.*, v. 2, n. 100, p. 468 – 471, 1996.

JANU, L. et al. Electrophoretic study of peptide-mediated quantum dot-human immunoglobulin bioconjugation. *Electrophoresis*, v. 34, p. 2725 – 32, 2013.

JIN, T. et al. Gd^{3+}-functionalized near-infrared quantum dots for in vivo dual modal (fluorescence/magnetic resonance) imaging. *Chemical communications* (Cambridge, England), p. 5764 – 6, 2008.

KAIRDOLF, B. A. et al. Semiconductor quantum dots for bioimaging and biodiagnostic applications. *Annual review of analytical chemistry* (Palo Alto, Calif.), v. 6, p. 143 – 62, 2013.

KARATHANASIS, E. et al. MRI mediated, non-invasive tracking of intratumoral distribution of nanocarriers in rat glioma. *Nanotechnology*, v. 19, p. 315101 –, 2011.

KERR, R. MRI of soft tissue disorders of the ankle. *Clinics in podiatric medicine and surgery*, v. 19, p. 285 – 307, 2002.

KIM, J. S. et al. Sentinel lymph node mapping of the stomach using fluorescent magnetic nanoparticles in rabbits. *Korean J. Gastroenterol*., v. 51, n. 1, p. 19 – 24, 2008.

KIRCHER, M. F. et al. A multimodal nanoparticle for preoperative magnetic resonance imaging and intraoperative optical brain tumor delineation. *Cancer research*, v. 63, p. 8122 – 5, 2003.

KOKTYSH, D.; BRIGHT, V.; PHAM, W. Fluorescent magnetic hybrid nanoprobe for multimodal bioimaging. *Nanotechnology*, v. 22, p. 275606 –, 2011.

KOLK, A. G. van der et al. Clinical applications of 7 T MRI in the brain. *European journal of radiology*, v. 82, p. 708 – 18, 2011.

KOOLE, R. et al. Paramagnetic lipid-coated silica nanoparticles with a fluorescent quantum dot core: a new contrast agent platform for multimodality imaging. *Bioconjugate chemistry*, v. 19, p. 2471 – 9, 2008.

KOOLE, R. et al. Paramagnetic lipid-coated silica nanoparticles with a fluorescent quantum dot core: a new contrast agent platform for multimodality imaging. *Bioconjug. Chem*., v. 19, n. 12, p. 2471 – 2479, 2008.

LAM, T. et al. Superparamagnetic iron oxide based nanoprobes for imaging and theranostics. *Advances in colloid and interface science*, v. 199-200, p. 95 – 113, 2013.

LANGKAMMER, C. et al. Susceptibility induced gray-white matter MRI contrast in the human brain. *NeuroImage*, v. 59, p. 1413 – 9, 2011.

LAURENT, S. et al. Magnetic iron oxide nanoparticles: synthesis, stabilization, vectorization, physicochemical characterizations, and biological applications. *Chemical reviews*, v. 108, p. 2064 – 110, 2008.

LAUTERBUR, P. C. Image formation by induced local interactions: Examples Employing Nuclear Magnetic Resonance. *Clin. Orthop. Relat. Res*., v. 244, p. 3 – 6, 1989.

LIU, L. et al. Multimodal imaging probes based on Gd-DOTA conjugated quantum dot nanomicelles. *The Analyst*, v. 136, p. 1881 – 6, 2011.

MAHMOUD, W. et al. Advanced procedures for labeling of antibodies with quantum dots. *Analytical biochemistry*, v. 416, p. 180 – 5, 2011.

MANSFIELD, P. Multi-planar image formation using NMR spin echoes. *J. Phys. C: Solid State Phys*., v. 10, p. L55 – L58, 1977.

MARTINS, M. A.; TRINDADE, T. Os nanomateriais e a descoberta de novos mundos na bancada do químico. *Química Nova*, v. 35, p. 1434 – 1446, 2012.

MAZZOLA, A. A. Ressonância magnética: princípios de formação da imagem e aplicações em imagem funcional. *Revista Brasileira de Física Médica*, v. 3, n. 1, p. 117 – 129, 2009.

MERBACH, A.; HELM, L.; TÓTH, E. The Chemistry of Contrast Agents in Medical Magnetic Resonance Imaging. 2013.

MICHALET, X.; BENTOLILA, L. A.; WEISS, S. Molecular Imaging: Physics and Bioapplications of Quantum Dots. *Advances in Medical Physics*, cap. 8, v. 2, p. 111 – 127, 2008.

MICSKEI, K. et al. Oxygen-17 NMR study of water exchange on gadolinium polyaminopolyacetates [Gd(DTPA)(H2O)]2- and [Gd(DOTA)(H2O)]- related to NMR imaging. *Inorganic Chemistry*, v. 32, n. 18, p. 3844 – 3850, 1993.

MULDER, W. J. M. et al. Quantum dots for multimodal molecular imaging of angiogenesis. *Angiogenesis*, v. 13, p. 131 – 4, 6 2010.

MULDER, W. J. M. et al. Lipid-based nanoparticles for contrast-enhanced MRI and molecular imaging. *NMR in biomedicine*, v. 19, p. 142 – 64, 2 2006.

NA, H. B.; SONG, I. C.; HYEON, T. Inorganic Nanoparticles for MRI Contrast Agents. *Advanced Materials*, v. 21, n. 21, p. 2133 – 2148, 2009.

PAN, D. et al. Nanomedicine: perspective and promises with ligand-directed molecular imaging. *European journal of radiology*, v. 70, p. 274 – 85, 3 2009.

PEREIRA, G.; GERALDES, C. F. G. C. Design and Optimization of Gadolinium Based Contrast Agents for Magnetic Resonance Imaging. *Ann. Magn. Reson.*, v. 6, p. 1 – 33, 2007.

PRINZEN, L. et al. Optical and magnetic resonance imaging of cell death and platelet activation using annexin a5-functionalized quantum dots. *Nano letters*, v. 7, p. 93 – 100, 2007.

PURCELL, E. M.; TORREY, H. C.; POUND, R. V. Resonance Absorption by Nuclear Magnetic Moments in a Solid. *Phys. Rev*., v. 69, p. 37 – 38, 1946.

RESCH-GENGER, U. et al. Quantum dots versus organic dyes as fluorescent labels. *Nature Methods*, v. 5, p. 763 – 775, 2008.

ROGACH, A. L. et al. Aqueous Synthesis of Thiol-Capped CdTe Nanocrystals: State-of-the-Art. *J. Phys. Chem. C*, v. 111, n. 40, p. 14628 – 14637, 2007.

SANTOS, B. S.; FARIAS, P. M. A.; FONTES, A. Semiconductor Quantum Dots for Biological Applications. *Handbook of Self Assembled Semiconductor Nanostructures Novel Devices in Photonics and Electronics*, Mohamed Henine (Ed.), *Amsterdam: Elsevier*, p. 773 – 798, 2008.

SATO, N. et al. Pharmacokinetics and enhancement patterns of macromolecular MR contrast agents with various sizes of polyamidoamine dendrimer cores. *Magnetic resonance in medicine*, v. 46, p. 1169 – 73, 2001.

SHAO, L. et al. Studies on interaction of CdTe quantum dots with bovine serum albumin using fluorescence correlation spectroscopy. *Journal of fluorescence*, v. 19, p. 151 – 7, 2008.

SHOKROLLAHI, H. Contrast agents for MRI. v. 33, n. 8, p. 4485 – 4497, 2013.

SILVA, F. O. et al. O estado da arte da síntese de semicondutores nanocristalinos coloidais. *Química Nova*, v. 33, p. 1933 – 1939, 2010. ISSN 0100-4042.

SMITH, A. M.; GAO, X.; NIE, S. Quantum dot nanocrystals for in vivo molecular and cellular imaging. *Photochemistry and photobiology*, v. 80, p. 377 – 85, 2004.

SOLOMON, I. Relaxation processes in a system of two spins. *Phys. Rev.*, v. 99, p. 559 – 559, 1955.

SONG, F.; CHAN, W. C. W. Principles of conjugating quantum dots to proteins via carbodiimide chemistry. *Nanotechnology*, v. 22, p. 494006 –, 2011.

STARMANS, L. W. E. et al. Influence of cell-internalization on relaxometric, optical and compositional properties of targeted paramagnetic quantum dot micelles. *Contrast media & molecular imaging*, v. 6, p. 100 – 9, 2010.

STASIUK, G. J. et al. Cell-permeable Ln(III) chelate-functionalized InP quantum dots as multimodal imaging agents. *ACS nano*, v. 5, p. 8193 – 201, 2011.

STASIUK, G. J. et al. Optimizing the relaxivity of Gd III complexes appended to InP/ZnS quantum dots by linker tuning. *Dalton transactions* (*Cambridge, England*), v. 42, p. 8197 – 200, 2013.

TAN, W. B.; ZHANG, Y. Multifunctional Quantum-Dot-Based Magnetic Chitosan Nanobeads. v. 17, p. 2375 – 2380, 2005.

TARDIF, C. L. et al. Advanced MRI techniques to improve our understanding of experience-induced neuroplasticity. *NeuroImage*, v. 131, p. 55 – 72, 2015.

THOMAZ, A. A. Plataforma Fotônica Integrada e suas Aplicações em Estudos de Quantum Dots e Processos Biológicos. Tese (Programa de Pós Graduação do Instituto de Física "Gleb Wataghin") — Universidade Estadual de Campinas. 240 p. 2013.

WEISHAUPT, D.; KÖCHLI, V. D.; MARINCEK, B. How does MRI work?: An Introduction to the Physics and Function of Magnetic Resonance Imaging. 2008.

WEISSLEDER, R.; BOGDANOV, A.; PAPISOV, M. Drug targeting in magnetic resonance imaging. Magnetic resonance quarterly, v. 8, p. 55 – 63, 1992.

WEISSLEDER, R.; PITTET, M. J. Imaging in the era of molecular oncology. *Nature*, v. 452, p. 580 – 9, 2008.

XIE; LEE, S.; CHEN, X. Nanoparticle-based theranostic agents. *Advanced drug delivery reviews*, v. 62, p. 1064 – 79, 2010.

YI, D. K. et al. Silica-coated nanocomposites of magnetic nanoparticles and quantum dots. *Journal of the American Chemical Society*, v. 127, p. 4990 – 1, 2005.

YU, W. W. et al. Experimental Determination of the Extinction Coefficient of CdTe, CdSe, and CdS Nanocrystals. *Chem. Mater.*, v. 15, n. 14, p. 2854 – 2860, 2003.

ZHOU, Z.; LU, Z. Gadolinium-based contrast agents for magnetic resonance cancer imaging. Wiley interdisciplinary reviews. *Nanomedicine and nanobiotechnology*, v. 5, p. 1 – 18, 2012.

ANEXO A

Normas para submissão ao *Journal Royal Society of Chemistry Advances*

Journal Name

ARTICLE

Title

A. N. Authorname,[a] A. N. Authorname[b] and A. N. Authorname[c]

Received 00th January 20xx,
Accepted 00th January 20xx

DOI: 10.1039/x0xx00000x

www.rsc.org/

Abstract text goes here. The abstract should be a single paragraph that summarises the content of the article

A Headings are the primary heading type e.g. Introduction, Results and discussion, Experimental

B Headings should always be subordinate to A headings e.g. Synthetic procedures, Materials and methods, Crystallography.

C headings should always be subordinate to B headings e.g. General procedure for synthesis of compound X. The main paragraph text follows directly on here.

The main text of the article should appear here with headings as appropriate.

Conclusions

The conclusions section should come in this section at the end of the article, before the acknowledgements.

Acknowledgements

The acknowledgements come at the end of an article after the conclusions and before the notes and references.

Notes and references

‡ Footnotes relating to the main text should appear here. These might include comments relevant to but not central to the matter under discussion, limited experimental and spectral data, and crystallographic data.

§
§§
etc.
1 Citations should appear here in the format A. Name, B. Name and C. Name, *Journal Title*, 2000, **35**, 3523; A. Name, B. Name and C. Name, *Journal Title*, 2000, **35**, 3523.
2 ...

Formatting – please delete this box prior to submission

- Graphics, including tables, will be located at the top or bottom of the column following their first citation in the text during production (unless they are equations, which appear in the flow of the text). They can be single column or double column as appropriate and require appropriate captions.
- Text is not wrapped around any of the graphics.
- During production, sufficient space will be inserted around graphics for clarity of reading; a horizontal bar will also be used to separate all inserted graphics, tables and their captions from the text:

- Please consult the Styles menu for recommended formatting for all text, including footnotes, references, tables, images and captions.

[a] *Address here.*
[b] *Address here.*
[c] *Address here.*

† Footnotes relating to the title and/or authors should appear here.
Electronic Supplementary Information (ESI) available: [details of any supplementary information available should be included here]. See DOI: 10.1039/x0xx00000x

ANEXO B

*CdTe quantum dots as fluorescent probes… (*artigo publicado no *Journal Biochimica et Biophysica Acta*)

Biochimica et Biophysica Acta 1860 (2016) 28–35

Contents lists available at ScienceDirect

Biochimica et Biophysica Acta

journal homepage: www.elsevier.com/locate/bbagen

CdTe quantum dots as fluorescent probes to study transferrin receptors in glioblastoma cells

Paulo E. Cabral Filho [a], Ana L.C. Cardoso [b], Maria I.A. Pereira [a], Ana P.M. Ramos [a], Fernando Hallwass [c], M. Margarida C.A. Castro [d,e], Carlos F.G.C. Geraldes [d,e], Beate S. Santos [f], Maria C. Pedroso de Lima [b], Giovannia A.L. Pereira [c], Adriana Fontes [a,*]

[a] Biophysics and Radiobiology Department, Federal University of Pernambuco, Recife, PE, Brazil
[b] CNC- Center for Neuroscience and Cell Biology, University of Coimbra, Coimbra, Portugal
[c] Department of Fundamental Chemistry, Federal University of Pernambuco, Recife, PE, Brazil
[d] Department of Life Sciences, Faculty of Science and Technology, University of Coimbra, Coimbra, Portugal
[e] Coimbra Chemistry Center, University of Coimbra, Coimbra, Portugal
[f] Department of Pharmaceutical Sciences, Federal University of Pernambuco, Recife, PE, Brazil

ARTICLE INFO

Article history:
Received 30 June 2015
Received in revised form 18 September 2015
Accepted 30 September 2015
Available online 3 October 2015

Keywords:
Nanoparticles
Cancer cells
Transferrin
Receptors
Bioconjugation
Covalent binding

ABSTRACT

Background: Overexpression of transferrin receptors (TfRs), which are responsible for the intracellular uptake of ferric transferrin (Tf), has been described in various cancers. Although molecular biology methods allow the identification of different types of receptors in cancer cells, they do not provide features about TfRs internalization, quantification and distribution on cell surface. This information can, however, be accessed by fluorescence techniques. In this work, the quantum dots (QDs)' unique properties were explored to strengthen our understanding of TfRs in cancer cells.
Methods: QDs were conjugated to Tf by covalent coupling and QDs-(Tf) bioconjugates were applied to quantify and evaluate the distribution of TfRs in two human glioblastoma cells lines, U87 and DBTRG-05MG, and also in HeLa cells by using flow cytometry and confocal microscopy.
Results: HeLa and DBTRG-05MG cells showed practically the same TfR labeling profile by QDs-(Tf), while U87 cells were less labeled by bioconjugates. Furthermore, inhibition studies demonstrated that QDs-(Tf) were able to label cells with high specificity.
Conclusions: HeLa and DBTRG-05MG cells presented a similar and a higher amount of TfR than U87 cells. Moreover, DBTRG-05MG cells are more efficient in recycling the TfR than the other two cells types.
General significance: This is the first study about TfRs in human glioblastoma cells using QDs. This new fluorescent tool can contribute to our understanding of the cancer cell biology and can help in the development of new therapies targeting these receptors.

1. Introduction

Transferrin (Tf) is a β-globin with approximately 670–700 amino acids, which binds to a cell surface receptor (TfR) expressed by most proliferating cells with particularly high expression on tumor cells, being one of the biomolecules most applied to cancer cell targeting [1]. The TfR is also known as CD71 and promotes the cellular uptake of ferric Tf [2], by clathrin-mediated endocytosis [3]. Nanotechnology approaches have taken advantage of the potential use of the TfRs to improve therapy and diagnostic procedures related to cancer. The most common systems employed for these purposes are liposomes [4,5], metallic nanoparticles [6,7] and magnetic nanoparticles [3]. These nanosystems have been functionalized with Tf to target the TfR in order to improve diagnostic methods, as well as the efficacy of chemotherapeutics, since cancer cells and tissues overexpress TfR on their surface with respect to normal cells. Zhai et al. [4], for instance, used TfRs as targets of liposomes conjugated to Tf and loaded with docetaxel, showing that these nanocarriers are a promising chemotherapeutic delivery vehicle for cancer therapeutics, when compared to liposomes lacking Tf. Therefore, studies related to the TfR can provide a better understanding of the cell biology of cancer and also help to improve its treatment.

TfRs have been widely studied by molecular biology approaches, which proved to be a valuable tool in the identification of different types of receptors in cancer cells [8–10]. However, molecular biology methods do not provide information about the cellular internalization of the receptor, its quantification and distribution. Fluorescence-based techniques have high sensitivity to quantify biomolecules with

* Corresponding author at: Av. Prof. Moraes Rego, S/N. Departamento de Biofísica e Radiobiologia, CCB, UFPE, 50670-901, Recife, PE, Brazil.
E-mail address: adriana.fontes.biofisica@gmail.com (A. Fontes).

http://dx.doi.org/10.1016/j.bbagen.2015.09.021
0304-4165/

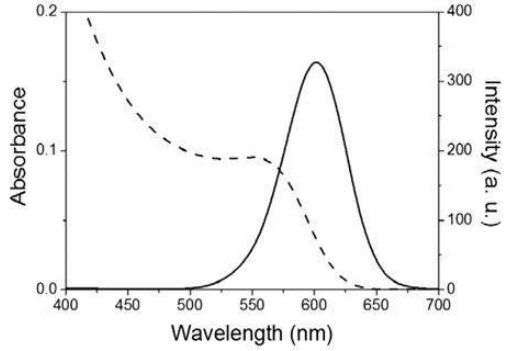

Fig. 1. Optical characterization of CdTe QDs aqueous colloidal suspension: absorption (dashed line) and emission (solid line) spectra. The excitation wavelength (λ_{exc}) for the emission spectrum was 365 nm.

high specificity and thus can be used as innovative and attractive methods to investigate receptor intracellular trafficking and distribution, complementing molecular biology studies [11]. Among the most promising probes that can be applied in fluorescence-based research are the quantum dots (QDs), which are semiconductor fluorescent nanoparticles that have great potential for biological research due to their unique optical and chemical properties. QDs present exceptional resistance to photobleaching, enabling long-term studies, and their active surface allows their functionalization with biomolecules in order to reach biological targets with a high specificity [12–15]. These QDs' features can be employed to strengthen our understanding of cellular receptors, such as the TfR.

The aim of this work was to apply CdTe QDs conjugated to Tf (QDs-Tf) as probes to study the TfRs in human glioblastoma cells, by using the complementary analyzes provided by fluorescence confocal microscopy and flow cytometry. The TfR was quantified and its distribution was analyzed in two different human glioma cells lines, U87 (glioblastoma) and DBTRG-05MG (recurrent glioblastoma). HeLa cells (human epithelial cervical carcinoma) were used as a control cellular model in this work, since QDs associated to Tf have already been applied to study the TfR in these cells [16–19]. However, the specificity of such conjugates has not been fully proved in those previous works. Here, the bioconjugation procedure of QDs to Tf was improved and the specificity of the labeling was demonstrated by TfR saturation assays. Moreover, to our knowledge, this is the first study that not

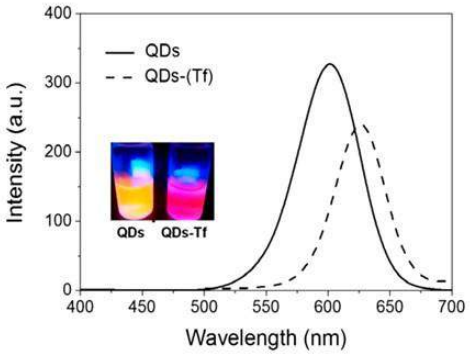

Fig. 2. Emission spectra of bare QDs (solid line) and QDs-(Tf) (dashed line). Pictures of the QDs (orange emission) and the bioconjugates (red emission) show their fluorescence under UV–Vis excitation (λ_{exc} = 365 nm).

Table 1
Fluorescence Microplate Assay results obtained from the average signal of fluorescence intensities (controls and bioconjugates) and percentage of relative fluorescence intensity of the bioconjugates.

Systems	Average of signal 4 days	RF (%) 4 days	Average of signal 10 days	RF (%) 10 days
Transferrin	151.6	–	122.6	–
QDs	212.0	–	258.0	–
QDs-(Tf)	698.0	283.9	41,615.0	21,764.0

only investigates the TfR in these two glioblastoma cell lines, but also compares the amount and the distribution of TfRs on these types of tumor cells, using the HeLa cell line as reference.

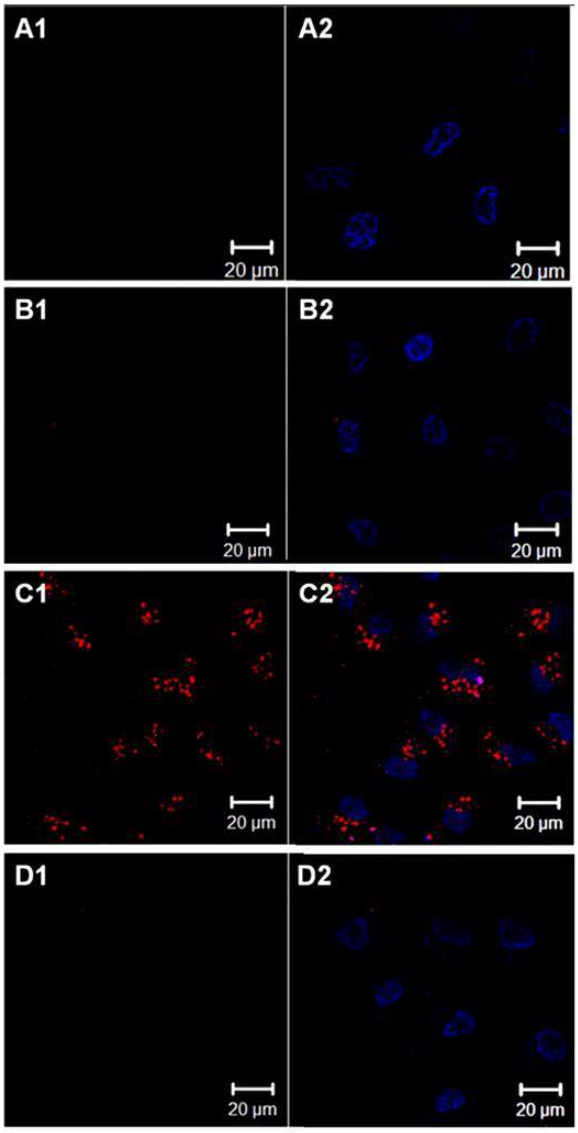

Fig. 3. Confocal microscopy images of HeLa cells labeled by QDs-(Tf). (A) Control HeLa cells, (B) HeLa cells incubated with bare QDs, (C) HeLa cells incubated with QDs-(Tf) and (D) HeLa cells incubated with QDs-(Tf) after TfR saturation. The identification (1) refers to the confocal emission channel LP 565 nm and the identification (2) refers to the overlap of LP 565 nm and Hoechst emission channel (BP 420-480 nm). Scale Bar: 20 μm.

2. Experimental procedures

2.1. Synthesis and characterization of CdTe-MSA QDs

CdTe-MSA QDs were synthesized as an aqueous colloidal dispersion according to a previously reported method, with some modifications [20]. Briefly, QDs were prepared by adding Te^{2-} ions to a $Cd(ClO_4)_2$ solution at pH > 10 in the presence of MSA (mercaptosuccinic acid) as stabilizing agent in a molar ratio of 5:1:6 (Cd:Te:MSA, respectively). The Te^{2-} aqueous solution was prepared by reducing metallic tellurium with $NaBH_4$ at a high pH and under nitrogen saturated inert atmosphere. The reaction proceeded under constant stirring and heating at 90 °C during 5 h.

After their synthesis, QDs were optically characterized by absorption and emission spectroscopy carried out on a spectrophotometer Evolution 600 UV–Vis (Thermo Scientific) and on spectrometer LS 55 (PerkinElmer, at $\lambda_{exc} = 365$ nm), respectively.

2.2. CdTe-MSA QDs conjugation to transferrin

CdTe-MSA QDs were conjugated with human holo transferrin (Tf) (Sigma Aldrich) by using N-ethyl-3-(3-dimethylaminopropyl)carbo diimide hydrochloride (EDC — Fluka) and N-hydroxysulfosuccinimide sodium salt (Sulfo-NHS — Sigma Aldrich) as coupling reagents.

First, the pH of 2 mL of the CdTe-MSA QDs dispersion (at 0.84 μM) was adjusted to 5.5 by using MSA at 4.9% (*w*/*v*). Then, 1 mL of EDC (at 4 $mg \cdot mL^{-1}$) was added and after 5 min, 1 mL of Sulfo-NHS (at 5.5 $mg \cdot mL^{-1}$) was also added to the QDs aqueous suspension [21,22]. Then, 15 min later, 194 μL of Tf (at 1 $mg \cdot mL^{-1}$) was added to reach a ratio of QDs:Tf 1:2 (particle:molecule).

Before cell labeling, the QDs-(Tf) conjugated system was incubated with 50 μL of TRIS base (at 1 mM) for 2 h under slow agitation. This procedure was used to quench the free carboxyl groups of non-conjugated QDs in order to minimize unspecific labeling. QDs-(Tf) were optically characterized by emission spectroscopy at $\lambda_{exc} = 365$ nm by using the same spectrometer mentioned above (LS 55, PerkinElmer).

2.3. Confirmation of conjugation QDs-(Tf) by Fluorescence Microplate Assay (FMA)

To confirm the efficiency of the bioconjugation process, we employed the Fluorescence Microplate Assay (FMA) [23]. Briefly, all the systems (Tf, bare QDs and QDs-(Tf)) were placed in a polystyrene microplate (black 96-well Optiplate F HB microplates — PerkinElmer) in triplicates, at the same concentration used for the bioconjugation assay. The plate was maintained for 2 h in an incubator (water bath, humid chamber) at 37 °C. After this period, the plate was washed three times with a phosphate buffered saline solution, PBS 1× (from now on named as PBS). We analyzed the conjugates as a function of time by evaluating the QDs-(Tf) samples at 4th and 10th days after the initial bioconjugation assay.

Fluorescence measurements were performed on a WALLAC 1420 Plate Reader, equipped with the software Victor² (PerkinElmer). The excitation band pass filter used was the BP 405 nm ± 2.5 nm and the emission band pass filter was the BP 595 nm ± 15 nm. The acquisition time was 1 s, the lamp was set to 20,000 and normal slits were used for the excitation of samples and for collecting the emission.

2.4. Cell culture

HeLa cells (human epithelial cervical carcinoma) were obtained from the American Type Culture Collection (Manassas, VA, USA) and the U87 (human glioblastoma) and DBTRG-05MG (human recurrent glioblastoma) cells were kindly provided by Dr. Peter Canoll (Columbia University, New York, NY) and Dr. Massimiliano Salerno (Siena Biotech, Italy). HeLa and U87 cells were cultured in Dulbecco's modified Eagle's medium with high glucose (DMEM — Sigma Aldrich) supplemented with 10% of fetal bovine serum (FBS — Gibco), 100 $mg \cdot mL^{-1}$ streptomycin and 100 units $\cdot mL^{-1}$ penicillin (Sigma Aldrich) at 37 °C in a humidified atmosphere with 5% CO_2. DBTRG-05MG cells were cultured in Roswell Park Memorial Institute (RPMI — Sigma Aldrich) 1640 medium supplemented with 10% of FBS, 100 $mg \cdot mL^{-1}$streptomycin and 100 units $\cdot mL^{-1}$ penicillin at 37 °C in a humidified atmosphere with 5% CO_2. When HeLa cells reached 90% confluence in the culture

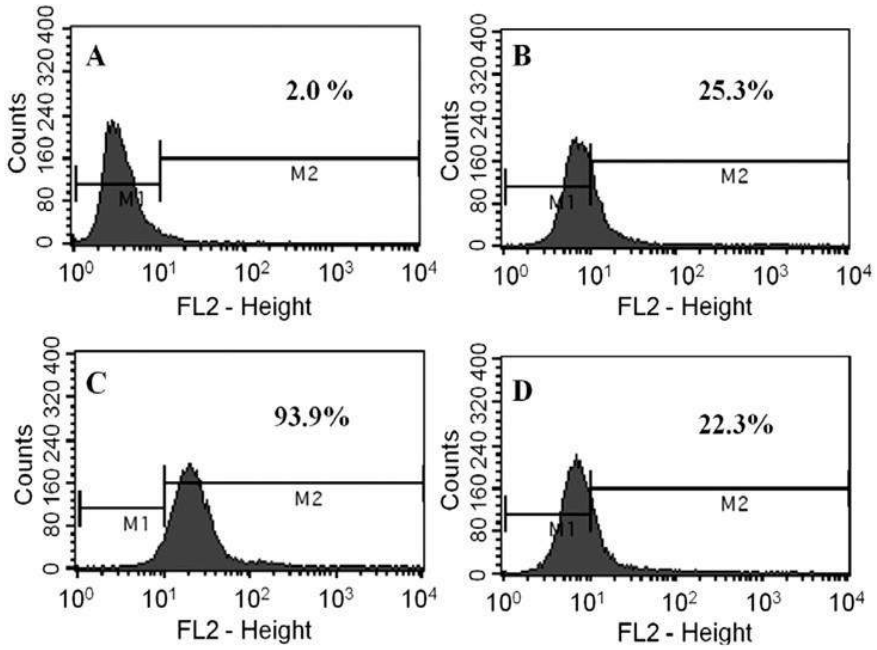

Fig. 4. Flow cytometry analysis of HeLa cells. In (A) HeLa cells in PBS, (B) HeLa cells incubated with bare QDs (C) HeLa cells incubated with QDs-(Tf) and (D) HeLa cells incubated with QDs-(Tf) after Tf-receptor saturation.

flask, they were detached with 0.25% of trypsin (Sigma Aldrich) in Dissociation Buffer (Gibco). Detachment of U87 and DBTRG cells was performed exclusively with Dissociation Buffer. The cells were then seeded onto a 6-well plate (1.5×10^5 cells/well – Thermo Scientific™ BioLite) and incubated for 24 h for flow cytometry studies and in an 8-well plate (2.0×10^4 cells/well – μSlide IbiTreat, Germany) for confocal microscopy analysis. At this time point, cells exhibited a confluence of around 80–90% in the wells.

2.5. Labeling cancer cells with QDs-(Tf)

After incubation for 24 h in 6-well or 8-well plates, the cells were washed with PBS and the following experimental conditions were assayed: (I) control cells with PBS; (II) PBS and bare QDs (1:1 *v/v*); (III) PBS and QDs-(Tf) (1:1 *v/v*). After 1 h of incubation at 37 °C, the cells were washed with PBS before flow cytometry and confocal microscopy analysis to remove any residual labeling on the cell surface by bare QDs.

The percentage of labeled cells was determined by flow cytometry (FACSCalibur™, Becton Dickinson). In these studies, HeLa cells were detached from the 6-well plate upon incubation with trypsin 0.25% in Dissociation Buffer followed by trypsin inactivation with DMEM and then placed in suspension. U87 and DBTRG cells were detached exclusively with Dissociation Buffer. The cell suspensions were washed 3 times with PBS and pelleted by centrifugation at 1200 × *g*, 30 s (MiniSpin – Eppendorf). Around 20,000 events were acquired for each experimental condition following excitation at 488 nm. The emission was detected with the band pass filter 585/20 nm and the collected data were processed by the Cell Pro Software (Cell Quest™, Becton-Dickinson).

For confocal analysis, and following the establishment of different experimental conditions, the cells plated onto 8-well plates were washed three times with PBS. The cell nuclei were stained for 5 min with the fluorescent DNA-binding dye Hoechst 33,342 (at a final concentration of 1 $\mu g \cdot mL^{-1}$), and the cells were washed with PBS three times before being observed under a confocal microscope (Zeiss LSM 510 META).

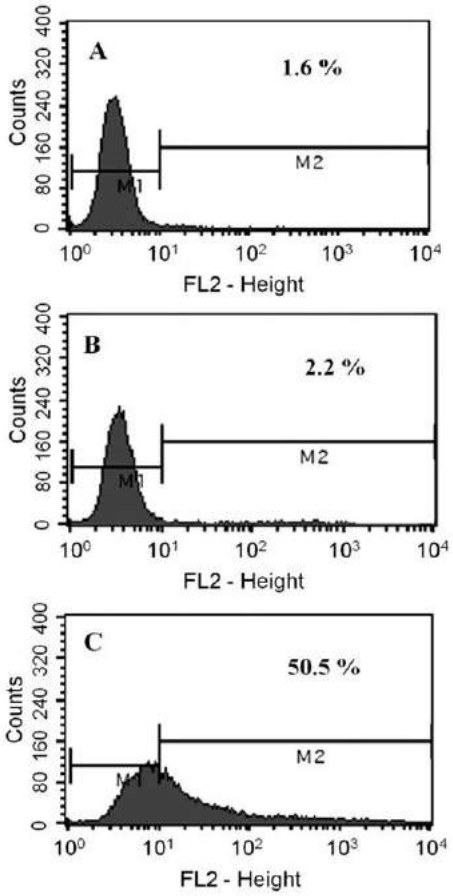

Fig. 5. Flow cytometry analysis of HeLa cells following incubation at 4 °C. (A) HeLa cells in PBS. (B) HeLa cells incubated with bare QDs, and (C) HeLa cells incubated with QDs-(Tf).

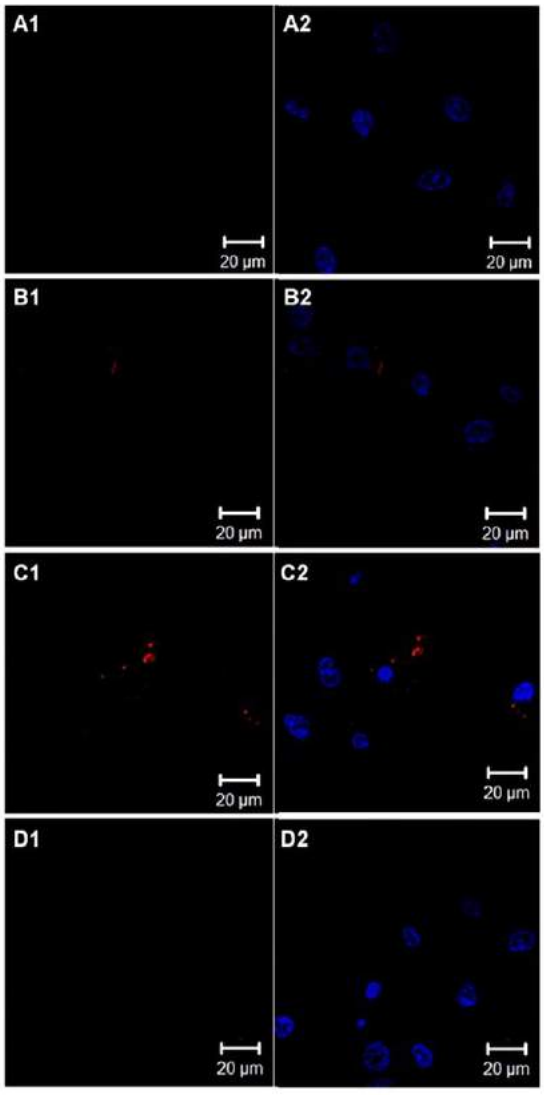

Fig. 6. Confocal microscopy images of U87 cells labeled by QDs-(Tf). (A) Control U87 cells, (B) U87 cells incubated with bare QDs, (C) U87 cells incubated with QDs-(Tf) and (D) U87 cells incubated with QDs-(Tf) after TfR saturation. The identification (1) refers to the confocal emission channel LP 565 nm and the identification (2) refers to the overlap of LP 565 nm and Hoechst emission channel (BP 420-480 nm). Scale Bar: 20 μm.

In order to confirm the specificity of the labeling, as well as the efficiency of the bioconjugation, cells were also incubated with excess of free human holo transferrin (at a final concentration of 10 mg·mL^{-1}) for 1 h at 37 °C, aiming at saturating the TFRs [24], before the confocal analysis. After this period, the cells were incubated with QDs-(Tf) for 1 additional hour at a final QDs-(Tf): free Tf ratio of 1:1 (v/v).

3. Results and discussion

3.1. Characterization of CdTe QDs and bioconjugates

According to optical characterizations, MSA QDs aqueous suspension presented a first maximum absorption peak at 548 nm, as can be observed in Fig. 1. By using the Dagtepe et al. [25] equation and the Rogach et al. [26] approximation, we estimated an average diameter of approximately 3.1 nm for these nanoparticles. Furthermore, taking into account the absorbance at the first maximum absorption peak, the CdTe QDs molar extinction coefficient proposed by Yu et al., [27] and the Lambert-Beer equation, we also estimated the QDs concentration as approximately 4.8 μM. The QDs colloidal suspension showed an emission maximum at 602 nm and a full width at a half maximum (FWHM) of about 58 nm, indicating a narrow emission spectrum (Fig. 1) which is ascribed to the exciton recombination.

Bare QDs and QDs-(Tf) (bioconjugates) exhibited similar emission spectra profiles for emission spectra (Fig. 2, $\lambda_{exc} = 365$ nm), however QDs-(Tf) showed a maximum emission at 626 nm. The observed red shift for the QDs-(Tf) suggests modifications on the QDs surface due to the bioconjugation process. The same behavior was observed in previous works using hydrophilic QDs conjugated to Concanavalin A [28] and to *Ulex europaeus* lectins [29]. In both cases the red shift of the emission peak was observed. Despite the red shift, QDs bioconjugates suspension remained highly fluorescent, as shown in Fig. 2.

3.2. Fluorescence Microplate Assay

The *FMA* results are presented in Table 1 as the average of the fluorescent signal of triplicate wells for controls and conjugates. The data analysis was carried out according to Carvalho et al. [23]. The relative fluorescence (RF) results for QDs-(Tf) were 283.9% and 21,764.0%, for the 4th and 10th days after bioconjugation, respectively. According to Carvalho et al. [23] the bioconjugation process is efficient when the bioconjugates show a RF higher than 100%. Therefore, our results (Table 1) indicate that the bioconjugation was efficient after four days and improved over time. The Sigma Aldrich product information indicates that Tf should remain active at 4 °C for 5–10 days after dilution.

3.3. Labeling HeLa cells by using QDs-(Tf)

As shown in Fig. 3, efficient and specific labeling of the TfR was observed in HeLa cells using QDs-(Tf) (Fig. 3, C1 and C2). HeLa cells, incubated with bare QDs (Fig. 3, B1 and B2), as well as after TfR saturation by free Tf (Fig. 3, D1 and D2), did not show considerable labeling, resulting in an image profile similar to the one obtained for control (in the absence of QDs) HeLa cells (Fig. 3, A1 and A2). The use of the DNA-binding dye Hoechst allowed to detect the intracellular localization of the receptor, indicating that 1 h of cell incubation with the QDs-(Tf) was sufficient to promote the internalization of the TfR by HeLa cells.

The confocal microscopy results were confirmed by flow cytometry analysis. As shown in Fig. 4C, about 94% of HeLa cells were labeled by QDs-(Tf), while incubation of the cells with bare QDs (Fig. 4B) or after inhibiting the specific interaction of QDs-(Tf) with TfRs (Fig. 4D), resulted in less than 26% of cell labeling. The residual labeling, less than 26%, may be attributed to QDs internalization by a TfR-independent pathway. This type of unspecific interaction between the cells and nanoparticles has been previously reported [30–32].

These results were confirmed by incubating the cells at 4 °C (Fig. 5), under which conditions endocytosis is compromised [33]. As shown in Fig. 5B, HeLa cells labeling by bare QDs was inhibited. On the other hand, QDs-(Tf) labeled 50.5% of HeLa cells (Fig. 5C) corresponding to the labeling of TfRs that remained on the cell surface, since the receptors cannot be internalized at this temperature, resulting in a decrease of labeled cells of approximately 43%, when compared to what was observed at 37 °C (Fig. 4C). Therefore, our results demonstrated specific

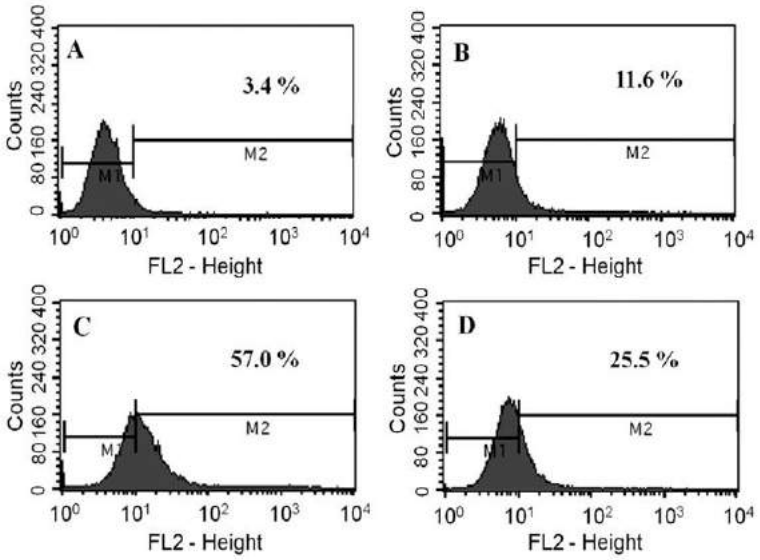

Fig. 7. Flow cytometry analysis of U87 cells. (A) U87 cells in PBS, (B) U87 cells incubated with bare QDs (C) U87 cells incubated with QDs-(Tf) and (D) U87 cells incubated with QDs-(Tf) after TfR saturation.

interaction of QDs- (Tf) with TfRs, which promoted cellular internalization of the QDs-(Tf).

In this work, HeLa cells were used as a model cell system and experimental approaches involving the blocking of TfR or inhibition of TfR-mediated endocytosis were employed to confirm the efficiency and specificity of QDs-(Tf) conjugates. Indeed, although the TfR has been studied by fluorescence assays with QDs [16,18,34,35], the targeting specificity of such conjugates has not been fully demonstrated. Sahoo et al. used polymeric nanoparticles (NPs) conjugated to Tf and showed that when NPs-Tf were incubated with an excess of Tf (50 μg), the percentage of labeled MCF-7 cells (a breast cancer cell line) was similar to that obtained when the cells were incubated with bare NPs [36]. These results are in agreement with our findings showing the specificity of the TfR labeling by QDs-Tf in HeLa cells. In this regard, less than 23% of HeLa cells were labeled after TfR saturation (Fig. 4D), this labeling being most likely attributed to QDs-(Tf) non-specific endocytosis, consistent with the results observed when HeLa cells were incubated with bare QDs, which do not exhibit affinity to TfR (Fig. 4B). To our knowledge, this is the first study addressing TfR saturation through competitive inhibition experiments with free Tf to confirm that the cell internalization of QDs-(Tf) bioconjugates is specific for TfRs.

Our results showed that 1 h of incubation with QDs-(Tf) was sufficient to promote their internalization through specific interaction with TfRs in HeLa cells. These achievements agree with those presented by Chan et al. and Tekle et al. that applied QDs-(Tf) to label specifically the TfR in HeLa cells [16,19]. Guan et al. carried out three different types of conjugations by using QDs and Tf, and showed that the most efficient was the one using EDC as coupling agent [18]. The authors demonstrated that approximately 85.5% of cells were labeled by QDs-Tf. Our results using EDC and Sulfo-NHS presented an improvement relative to these previous studies, showing a labeling percentage of about 93%. To our best knowledge, this is the first work that used EDC and Sulfo-NHS simultaneously as coupling agents to conjugate MSA-QDs to Tf. According to Hermanson [22], the simultaneous use of these coupling agents improves the bioconjugation process by minimizing the generation of reactive species, when compared to the individual use of EDC for bioconjugation purposes.

3.4. Labeling glioblastoma cells by using QDs-(Tf)

In studies addressing the TfR in glioblastoma cells, we employed the U87 human glioblastoma cell line, extensively reported as a relevant glioblastoma cellular model and the DBTRG-05MG cell line, established from a glioblastoma patient treated with local brain irradiation and multidrug chemotherapy. Confocal microscopy images of U87 cells, displayed in Fig. 6, show that the TfR is present in a minimal amount, since a very small amount of labeling could be observed following incubation with QDs-(Tf) (Fig. 6, C1 and C2). Blocking Tf-receptor by adding excess of free Tf decreased even further the cell labeling (Fig. 6, D1 and D2), and similar results were obtained after cell incubation with bare QDs (Fig. 6, B1 and B2).

The confocal microscopy results were confirmed by quantitative flow cytometry analysis of U87 cells, as illustrated in Fig. 7. Fig. 7C shows that 57.0% of U87 cells were labeled when incubated with QDs-(Tf). On the other hand, only 25.5% of cells were labeled after TfR saturation (Fig. 7D).

According to Dixit et al. [7], when U87 cells were incubated with gold nanoparticles functionalized by the Tf peptide, an accumulation of these nanostructures was observed inside the cells after 1 h, which increased until 24 h. The results of that study indicated that the endocytic activity of U87 cells occurs at a slower rate when compared to that of LN299 cells, another human glioma cell line, with an uptake plateau after 1 h. In agreement with the findings reported by Dixit et al., our results showed that U87 cells internalize QDs-(Tf) at a low extent which also seem to have a small amount of TfRs at the plasma membrane.

In contrast with U87 cells, confocal microscopy images of DBTRG-05MG cells incubated with QDs-(Tf) (Fig. 8, C1 and C2) showed that TfR internalization was very effective in these cells. After 1 h incubation with QDs-(Tf), DBTRG-05MG cells showed a similar profile to that in HeLa cells, regarding the presence of the TfR (Fig. 8C and Fig. 3C, respectively). Furthermore, when DBTRG-05MG cells were incubated with bare QDs (Fig. 8, B1 and B2) no significant unspecific labeling was observed. However, when these cells were incubated with QDs-(Tf), after TfR saturation with free Tf (Fig. 8, D1 and D2), fluorescent labeling in some cells was detected.

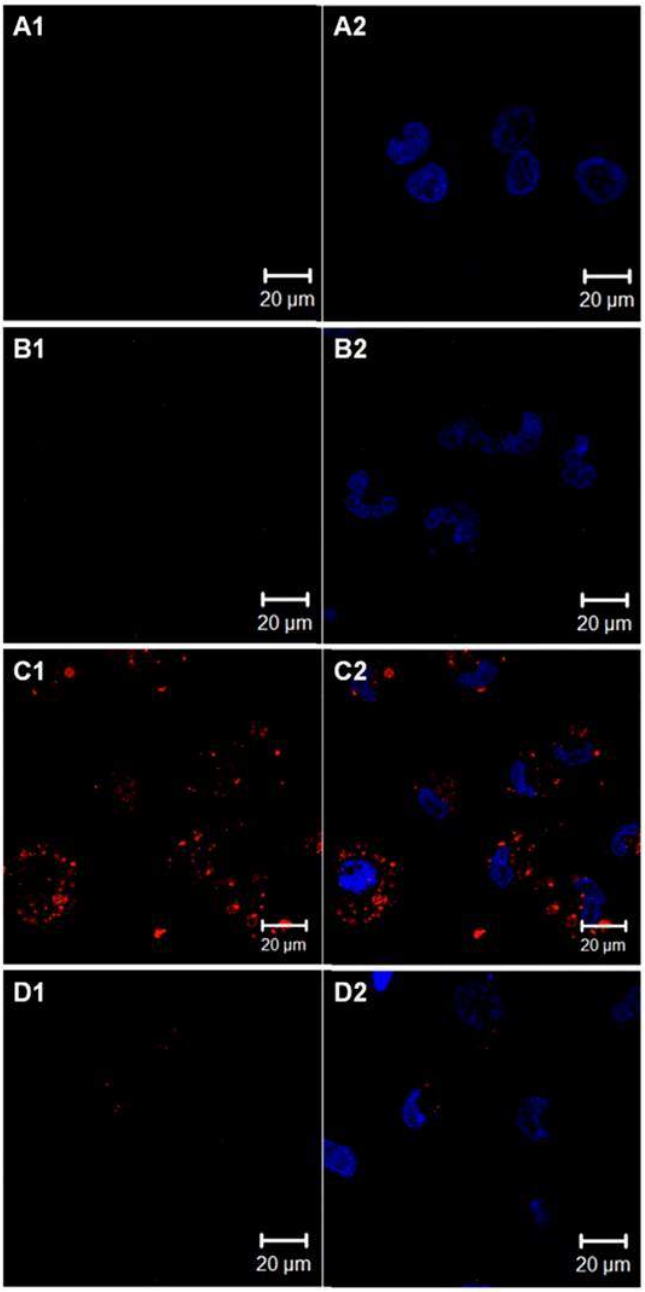

Fig. 8. Confocal microscopy images of DBTRG-05MG cells labeled by QDs-(Tf). (A) Control DBTRG-05MG cells (B) DBTRG-05MG cells incubated with bare QDs, (C) DBTRG-05MG cells incubated with QDs-(Tf) and (D) DBTRG-05MG cells incubated with QDs-(Tf) after TfR saturation. The identification (1) refers to the confocal emission channel LP 565 nm and the identification (2) refers to the overlap of LP 565 nm and Hoechst emission channel (BP 420-480 nm). Scale Bar: 20 μm.

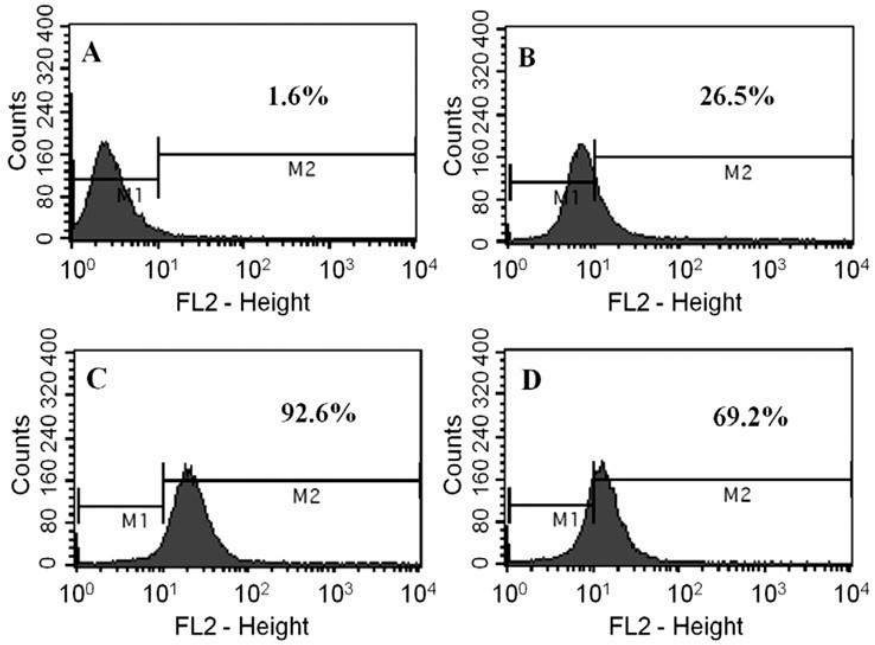

Fig. 9. Flow cytometry analysis in DBTRG-05MG cells. (A) DBTRG-05MG cells in PBS, (B) DBTRG-05MG cells incubated with bare QDs, (C) DBTRG-05MG cells incubated with QDs-(Tf) and (D) DBTRG-05MG cells incubated with QDs-(Tf) after TfR saturation.

These results obtained by confocal microscopy were confirmed through flow cytometry analysis (Fig. 9). Approximately 93% of DBTRG-05MG cells were positively labeled after 1 h incubation with QDs-(Tf) (Fig. 9C), indicating that these cells express a high amount of TfRs. However, when the cells were incubated with bare QDs, a significant decrease in the percentage of labeled cells was observed to about 26% (Fig. 9B). Furthermore, when the TfR was blocked by addition of excess free Tf, 69.2% of DBTRG-05MG cells still presented labeling by QDs-(Tf) (Fig. 9D), corroborating the observations made by confocal microscopy. Taken together, these results denote a more efficient TfR recycling in these cells as compared to U87 or HeLa cells, which can be attributed to a higher metabolic activity of DBTRG-05MG cells [37].

As mentioned before, the DBTRG-05MG cell line was originated from the tumor tissue of a patient owing a recurrent glioblastoma that has been treated with irradiation and chemotherapy [38]. This variant of glioblastoma is more aggressive and resistant to current chemotherapy when compared to that originated from U87 cells [39–41], which can also justify the high metabolic rate and the probably faster recycling of the TfR observed in DBTRG-05MG cells.

Moreover, our results demonstrate that HeLa and DBTRG-05MG cells express and internalize comparable amounts of TfRs, showing 94% and 93% of cells labeled by QDs-(Tf), respectively, while U87 cells present a lower quantity of TfRs, associated to a lower extent of internalization of these receptors, resulting in 57% of cells labeled by QDs-(Tf).

Fig. 10 shows comparative confocal microscopy images of the three cell lines, HeLa (Fig. 10A), U87 (Fig. 10B) and DBTRG-05MG (Fig. 10C), after incubation with QDs-(Tf). As observed, after 1 h of incubation, TfRs are accumulated inside HeLa and DBTRG-05MG cells in endocytic vesicles, indicating an efficient uptake of these receptors. This kind of internalization profile has already been reported previously in HeLa cells [16,19,35]. On the other hand, U87 cells (Fig. 10B) present a lower amount of TfRs, and the conjugates seem to be preferentially located at the cell membrane level, suggesting a lower endocytosis extent when compared to HeLa or DBTRG-05MG cells.

4. Conclusions

QDs-(Tf) were used in this work to quantify the expression and study the traffic of the TfRs in different types of mammalian cancer cells. HeLa and DBTRG-05MG cells present a similar amount of TfR, while U87 cells demonstrated to have a lower quantity of this receptor, when compared to the other two cell lines. Furthermore, DBTRG-05MG cells were more efficient in promoting the recycling of TfRs than HeLa or U87 cells. Therefore, this work suggests that a specific chemotherapeutic drug delivery

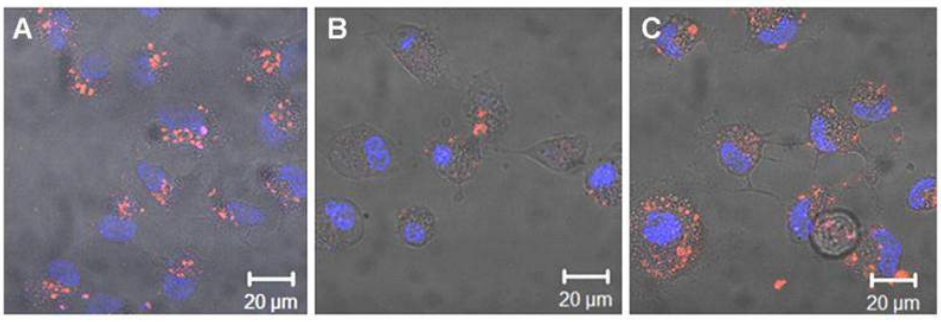

Fig. 10. Confocal microscopy images comparing HeLa, U87 and DBTRG-05MG cells following labeling by QDs-(Tf). These micrographs are overlaps of the confocal filters: LP 565, BP 420–480 nm emission and DIC. (A) HeLa cells, (B) U87 cells and (C) DBTRG-05MG cells. Scale bar: 20 nm.

system targeting TfRs could be more effective in DBTRG-05MG and HeLa cancer cells than in U87. This is an interesting result, particularly taking into consideration the fact that DBTRG-05MG cells are originated from a recurrent glioblastoma, while U87 cells derive from a primary tumor, which suggests that TfRs may play an important role in cancer cell maintenance in recurrent situations.

Overall, the results presented in this study illustrate that QDs-(Tf) can be applied to quantify TfR expression and also to study the dynamics of this receptor in different types of cancer cells. Therefore, we believe that this biophotonic tool can be of great value in future studies in cancer cell biology. The understanding of the molecular aspects of cancer cell biology can help to develop new and effective therapies for this disease, such as those targeting TfRs as a specific and efficient entry pathway for chemotherapeutic drugs.

Author contributions

PECF participated in all experiments involved in the study; MIAP and APMR synthesized and characterized the QDs and conjugates; GALP, MMC and FH analyzed and discussed the bioconjugation; ALC, MCPL, PECF and AF interpreted the microscopy and flow cytometry results; AF, BSS, GALP and CFGCG conceived and designed the experiments. All authors read and approved the final manuscript.

Disclosure

The authors confirm that there are no conflicts of interest in this work.

Acknowledgments

This work was supported by the Brazilian agencies: the Coordination for the Improvement of Higher Education Personnel (CAPES), through the Transnational Cooperation Program CAPES/FCT (331/13), the National Council for Scientific and Technological Development (CNPq), and the Foundation for Science and Technology of Pernambuco (FACEPE). This work is also linked to the National Institute of Photonics (INFo).

Transparency document

The Transparency document associated with this article can be found in the online version.

References

[1] H. Li, Z.M. Qian, Transferrin/transferrin receptor-mediated drug delivery, Med. Res. Rev. 22 (2002) 225–250.
[2] T.R. Daniels, E. Bernabeu, J.A. Rodríguez, S. Patel, M. Kozman, D.A. Chiappetta, E. Holler, J.Y. Ljubimova, G. Helguera, M.L. Penichet, Transferrin receptors and the targeted delivery of therapeutic agents against cancer, Biochim. Biophys. Acta 1820 (2012) 291–317.
[3] W. Ding, L. Guo, Immobilized transferrin Fe(3)O(4)@SiO(2) nanoparticle with high doxorubicin loading for dual-targeted tumor drug delivery, Int. J. Nanomedicine 8 (2013) 4631–4639.
[4] G. Zhai, J. Wu, B. Yu, C. Guo, X. Yang, R.J. Lee, A transferrin receptor-targeted liposomal formulation for docetaxel, J. Nanosci. Nanotechnol. 10 (2010) 5129–5136.
[5] H. Li, H. Sun, Z.M. Qian, The role of the transferrin–transferrin-receptor system in drug delivery and targeting, Trends Pharmacol. Sci. 23 (2002) 206–209.
[6] D.T. Wiley, P. Webster, A. Gale, M.E. Davis, Transcytosis and brain uptake of transferrin-containing nanoparticles by tuning avidity to transferrin receptor, Proc. Natl. Acad. Sci. U. S. A. 110 (2013) 8662–8667.
[7] S. Dixit, T. Novak, K. Miller, Y. Zhu, M.E. Kenney, A.-M. Broome, Transferrin receptor-targeted theranostic gold nanoparticles for photosensitizer delivery in brain tumors, Nanoscale 7 (2015) 1782–1790.
[8] D.J. Yoon, D.S.H. Chu, C.W. Ng, E.A. Pham, A.B. Mason, D. Hudson, V.C. Smith, R.T.A. MacGillivray, D.T. Kamei, Genetically engineering transferrin to improve its in vitro ability to deliver cytotoxins, J. Control. Release 133 (2009) 178–184.
[9] P. Ponka, C.N. Lok, The transferrin receptor: role in health and disease, Int. J. Biochem. Cell Biol. 31 (1999) 1111–1137.
[10] E.W. Müllner, L.C. Kühn, A stem-loop in the 3′ untranslated region mediates iron-dependent regulation of transferrin receptor mRNA stability in the cytoplasm, Cell 53 (1988) 815–825.
[11] L. Jing, K. Ding, S.V. Kershaw, I.M. Kempson, A.L. Rogach, M. Gao, Magnetically engineered semiconductor quantum dots as multimodal imaging probes, Adv. Mater. 26 (2014) 6367–6386.
[12] A. Sukhanova, I. Nabiev, Fluorescent nanocrystal quantum dots as medical diagnostic tools, Expert Opinion on Medical Diagnostics, 2 2008, pp. 429–447.
[13] I.L. Medintz, H.T. Uyeda, E.R. Goldman, H. Mattoussi, Quantum dot bioconjugates for imaging, labelling and sensing, Nat. Mater. 4 (2005) 435–446.
[14] X. Michalet, F.F. Pinaud, L.A. Bentolila, J.M. Tsay, S. Doose, J.J. Li, G. Sundaresan, A.M. Wu, S.S. Gambhir, S. Weiss, Quantum dots for live cells, in vivo imaging, and diagnostics, Science 307 (2005) 538–544.
[15] P. Alivisatos, The use of nanocrystals in biological detection, Nat. Biotechnol. 22 (2004) 47–52.
[16] W.C.W. Chan, S. Nie, Quantum dot bioconjugates for ultrasensitive nonisotopic detection, Science 281 (1998) 2016–2018.
[17] C. Schieber, A. Bestetti, J.P. Lim, A.D. Ryan, T.-L. Nguyen, R. Eldridge, A.R. White, P.A. Gleeson, P.S. Donnelly, S.J. Williams, P. Mulvaney, Conjugation of transferrin to azide-modified CdSe/ZnS core–shell quantum dots using cyclooctyne click chemistry, Angew. Chem. Int. Ed. 51 (2012) 10523–10527.
[18] L.-Y. Guan, Y.-Q. Li, S. Lin, M.-Z. Zhang, J. Chen, Z.-Y. Ma, Y.-D. Zhao, Characterization of CdTe/CdSe quantum dots-transferrin fluorescent probes for cellular labeling, Anal. Chim. Acta 741 (2012) 86–92.
[19] C. Tekle, B.v. Deurs, K. Sandvig, T.-G. Iversen, Cellular trafficking of quantum dot-ligand bioconjugates and their induction of changes in normal routing of unconjugated ligands, Nano Lett. 8 (2008) 1858–1865.
[20] C.G. Andrade, P.E. Cabral Filho, D.P.L. Tenório, B.S. Santos, E.I.C. Beltrão, A. Fontes, L.B. Carvalho, Evaluation of glycophenotype in breast cancer by quantum dot-lectin histochemistry, Int. J. Nanomedicine 8 (2013) 4623–4629.
[21] J. Wang, X. Huang, F. Zan, C.-g. Guo, C. Cao, J. Ren, Studies on bioconjugation of quantum dots using capillary electrophoresis and fluorescence correlation spectroscopy, Electrophoresis 33 (2012) 1987–1995.
[22] G.T. Hermanson, Chapter 3 — zero-length crosslinkers, in: G.T. Hermanson (Ed.), Bioconjugate Techniques, second editionAcademic Press, New York 2008, pp. 213–233.
[23] K.H.G. Carvalho, A.G. Brasi, P.E.C. Filho, D.P.L.A. Tenorio, A.C.A. de Siqueira, E.S. Leite, A. Fontes, B.S. Santos, Fluorescence plate reader for quantum dot-protein bioconjugation analysis, J. Nanosci. Nanotechnol. 14 (2014) 3320–3327.
[24] A.L.C. Cardoso, S. Simões, L.P. de Almeida, N. Plesnila, M.C. Pedroso de Lima, E. Wagner, C. Culmsee, Tf-lipoplexes for neuronal siRNA delivery: a promising system to mediate gene silencing in the CNS, J. Control. Release 132 (2008) 113–123.
[25] P. Dagtepe, V. Chikan, J. Jasinski, V.J. Leppert, Quantized growth of CdTe quantum dots; observation of magic-sized CdTe quantum dots, J. Phys. Chem. C 111 (2007) 14977–14983.
[26] A.L. Rogach, T. Franzl, T.A. Klar, J. Feldmann, N. Gaponik, V. Lesnyak, A. Shavel, A. Eychmüller, Y.P. Rakovich, J.F. Donegan, Aqueous synthesis of thiol-capped CdTe nanocrystals: state-of-the-art, J. Phys. Chem. C 111 (2007) 14628–14637.
[27] W.W. Yu, L. Qu, W. Guo, X. Peng, Experimental determination of the extinction coefficient of CdTe, CdSe, and CdS nanocrystals, Chem. Mater. 15 (2003) 2854–2860.
[28] J.-H. Wang, Y.-Q. Li, H.-L. Zhang, H.-Q. Wang, S. Lin, J. Chen, Y.-D. Zhao, Q.-M. Luo, Bioconjugation of concanavalin and CdTe quantum dots and the detection of glucose, Colloids Surf. A Physicochem. Eng. Asp. 364 (2010) 82–86.
[29] P.E. Cabral Filho, M.I.A. Pereira, H.P. Fernandes, A.A. de Thomaz, C.L. Cesar, B.S. Santos, M.L. Barjas-Castro, A. Fontes, Blood groups antigens studies using CdTe quantum dots and flow cytometry, Int. J. Nanomedicine 10 (2015) 4393–4404.
[30] S. Zhang, J. Li, G. Lykotrafitis, G. Bao, S. Suresh, Size-Dependent Endocytosis of Nanoparticles, Advanced materials (Deerfield Beach, Fla.), 21 2009, pp. 419–424.
[31] K.-T. Yong, H. Ding, I. Roy, W.-C. Law, E.J. Bergey, A. Maitra, P.N. Prasad, Imaging pancreatic cancer using bioconjugated InP quantum dots, ACS Nano 3 (2009) 502–510.
[32] D. Chen, G. Xu, B.A. Ali, K.-T. Yong, C. Zhou, X. Wang, J. Qu, P.N. Prasad, H. Niu, Uptake of transferrin-conjugated quantum dots in single living cells, Chin. Opt. Lett. 8 (2010) 940–943.
[33] V. Biju, T. Itoh, M. Ishikawa, Delivering quantum dots to cells: bioconjugated quantum dots for targeted and nonspecific extracellular and intracellular imaging, Chem. Soc. Rev. 39 (2010) 3031–3056.
[34] P.R. Sager, P.A. Brown, R.D. Berlin, Analysis of transferrin recycling in mitotic and interphase hela cells by quantitative fluorescence microscopy, Cell 39 (1984) 275–282.
[35] M.-Z. Zhang, R.-N. Yu, J. Chen, Z.-Y. Ma, Y.-D. Zhao, Targeted quantum dots fluorescence probes functionalized with aptamer and peptide for transferrin receptor on tumor cells, Nanotechnology 23 (2012) 485104.
[36] S.K. Sahoo, V. Labhasetwar, Enhanced antiproliferative activity of transferrin-conjugated paclitaxel-loaded nanoparticles is mediated via sustained intracellular drug retention, Mol. Pharm. 2 (2005) 373–383.
[37] N.-M. Tsai, S.-Z. Lin, C.-C. Lee, S.-P. Chen, H.-C. Su, W.-L. Chang, H.-J. Harn, The antitumor effects of angelica sinensis on malignant brain tumors in vitro and in vivo, Clin. Cancer Res. 11 (2005) 3475–3484.
[38] C.A. Kruse, D.H. Mitchell, B.K. Kleinschmidt-DeMasters, W.A. Franklin, H.G. Morse, E.B. Spector, K.O. Lillehei, Characterization of a continuous human glioma cell line DBTRG-05MG: growth kinetics, karyotype, receptor expression, and tumor suppressor gene analyses, In Vitro Cell. Dev. Biol. Anim. 28 (1992) 609–614.
[39] M.M. Zulkifli, R. Ibrahim, A.M. Ali, I. Aini, H. Jaafar, S.S. Hilda, N.B. Alitheen, J.M. Abdullah, Newcastle diseases virus strain V4UPM displayed oncolytic ability against experimental human malignant glioma, Neurol. Res. 31 (2009) 3–10.
[40] P.-C. Lin, T.-W. Chiou, H.-J. Harn, An evidence-based perspective of Angelica Sinensis (Chinese Angelica) for cancer patients, in: W.C.S. Cho (Ed.), Evidence-based Anticancer Materia Medica, Springer, Netherlands 2011, pp. 131–153.
[41] R. Wondergem, J.W. Bartley, Menthol increases human glioblastoma intracellular Ca(2+), BK channel activity and cell migration, J. Biomed. Sci. 16 (2009) 90-90.

ANEXO C

Bimodal nanostructured materials…

(capítulo aceito para publicação na *Encyclopedia of Nanoscience and Nanotechonology)*

ENN Encyclopedia of Nanoscience and Nanotechnology
www.aspbs.com/enn

Bimodal Nanostructured Materials Containing Quantum Dots for Optical and Magnetic Resonance Imaging

Goreti Pereira

Pharmaceutical Science Department, Federal University of Pernambuco, Recife, Pernambuco, Brazil; Biomedical Nanotechnology Research Group, Federal University of Pernambuco, Recife, Pernambuco, Brazil

Paulo E. Cabral Filho, Maria I. A. Pereira, Mariana P. Cabrera

Biomedical Nanotechnology Research Group, Federal University of Pernambuco, Recife, Pernambuco, Brazil; Biophysics and Radiobiology Department, Federal University of Pernambuco, Recife, Pernambuco, Brazil

Giovannia A. L. Pereira

Biomedical Nanotechnology Research Group, Federal University of Pernambuco, Recife, Pernambuco, Brazil; Fundamental Chemistry Department, Federal University of Pernambuco, Recife, Pernambuco, Brazil

Adriana Fontes

Biomedical Nanotechnology Research Group, Federal University of Pernambuco, Recife, Pernambuco, Brazil; Biophysics and Radiobiology Department, Federal University of Pernambuco, Recife, Pernambuco, Brazil

Beate S. Santos

Pharmaceutical Science Department, Federal University of Pernambuco, Recife, Pernambuco, Brazil; Biomedical Nanotechnology Research Group, Federal University of Pernambuco, Recife, Pernambuco, Brazil

CONTENTS

1. INTRODUCTION

Over the last years the interest in the development of bimodal probes, which could allow complementary

ISBN: x-xxxxx-xxx-x/$xx.00

Encyclopedia of Nanoscience and Nanotechnology
Edited by H. S. Nalwa
Volume xx: Pages (1–28)

diagnostic methods or that could be used as theranostic systems, has increased [1–3]. Since the majority of diseases that affect humans are multifactorial, the diagnostic techniques must be able to detect and distinguish the various mechanisms and/or phases of the disease. The association and simultaneous use of two or more diagnostic techniques will allow a more precise diagnostic, thus the utilization of two types of probes in one single particle can be very useful to reach this purpose [4–6]. In this chapter, we review the development of bimodal systems for optical and magnetic resonance images, specifically systems containing quantum dots (QDs).

Techniques based on fluorescence enabled not only the visualization, but also the biochemical analysis of several biological structures. Thus, advances in these techniques are the great interest in biomedical sciences, since these advances will allow a better understanding of the cellular functions and, consequently, the development of more efficient diagnostic and/or treatment approaches [7–9]. One of the principal advances in the microscopy-based techniques was the invention of fluorescence microscopy, which allowed the visualization in real-time images with chemical specificity and high sensibility [10, 11]. The use of fluorescent labels is important to evidence the desired structures of biomolecules. In this way, organic fluorophores are frequently used, although these dyes have some disadvantages such as fast photodegradation and high cytotoxicity [12, 13].

Scientific advances that aim to decrease the disadvantages associated with the currently used organic dyes has led to the emergence of a new class of fluorophores: quantum dots. QDs are semiconductor nanocrystals with dimensions of 1.5 to 10 nm that possess unique photophysical properties, due to the quantum confinement regime, such as great photostability, emission tunable according to the nanoparticle size, and an active surface, which allows their conjugation with other molecules [14, 15]. QDs have been widely used in bioanalytical assays, (1) for *in vitro* cells and tissues imaging, (2) for *in vivo* imaging of small animals, (3) for cancer and other diseases diagnosis, and (4) in biosensors [16–20].

Currently, the diagnostic imaging techniques available clinically are magnetic resonance image (MRI), X-ray computer tomography (also called CT), single photon emission tomography (SPECT), and positron emission tomography (PET), which can give images with resolution of a few millimeters. All these techniques have specific advantages and disadvantages, which can be related to spatial resolution, sensitivity, and/or the nature of the signal used for acquiring the images. MRI is one of the most powerful imaging diagnostic technique developed so far. It is non-invasive and produces images with anatomic detail able to draw inferences about the diagnosis of several diseases [6, 21]. When compared to the other clinical imaging techniques, MRI has several advantages, such as it does not use ionization radiation, images of normal and diseased tissues can be differentiable, and it presents a better spatial resolution (Fig. 1) [4, 5, 21].

In this context, the association of optical and magnetic resonance imaging techniques can offer a combination of imaging modalities more accurate for nanomedicine research and clinical applications. However, the development of multimodal imaging by association of optical and MRI probes is still considered a challenge, mainly since it depends on the design and fabrication of nanostructures that should have both properties in a unique and hybrid optimized nanoprobe. QDs have already been used in the development of bimodal probes for optical/PET, optical/CT and optical/MRI imaging [5, 6, 22–25].

In this chapter, we discuss not only the development of bimodal systems, for optical and magnetic resonance images, but also challenges and advances of their use in biomedical applications over the last 10 years. Aiming a better comprehension of the highlighted characteristics for the presented bimodal systems, first we present briefly QDs and MRI principles, followed by the development of bimodal nanostructures, which is divided into three parts according to the adopted preparation strategy, namely (1) QDs associated with iron-nanoparticles, (2) doped QDs, and (3) QDs associated to Gd^{3+} chelates.

2. BASIC PRINCIPLES OF QUANTUM DOTS AND MAGNETIC RESONANCE IMAGING

2.1. Quantum Dots

Nanotechnology has attracted the attention of many research groups and the nanomaterials have become fundamental elements to technology and science, due to their specific size-dependent properties. QDs dots are a class of these emerging nanomaterials and they are known to be powerful tool in several applications involving the production and use of fluorescence, such as in electroluminescent devices, photovoltaic cells, and more recently in biomedical application and also as probes for nanotheranostic and/or bimodal nanoparticles [14, 26–28].

QDs are semiconductor nanocrystals that have typical diameters ranging from 1.5 to 10 nm, and at this size range, they are under quantum confinement effect in three dimensions. As consequence of this effect, QDs have unique optical properties that are different from bulk semiconductors materials [17, 29]. The intrinsic fluorescence of the semiconductor materials arise due to electronic transitions from the valence band (VB) to the conduction band (CB) and their return to the fundamental state, promoting light emission [30]. The emission region depends on the energetic distance between CB and VB (band gap energy-E_g). In bulk semiconductors, the emission region is related to the material composition. As aforementioned, after light absorption by the semiconductor an electron (e^-) from the BV can be excited to the BC, resulting in a hole (h^+) in the BV. The electron–hole pair has a high attraction between them, due to the Coulomb forces during the small time of light absorption, and may become bounded together [31]. Therefore, the fluorescence is emitted when the e^- returns to its h^+. The e^-h^+ pair is called exciton and also can be considered a hydrogen-like species. Moreover, the distance between e^-h^+ pair is called exciton Bohr radius (a_B). When the semiconductor material has a small size, about a few nanometers, which is smaller than the Bohr radius, we can say that they are under quantum confinement regime [31, 32]. This was a brief explanation about the quantum confinement effect.

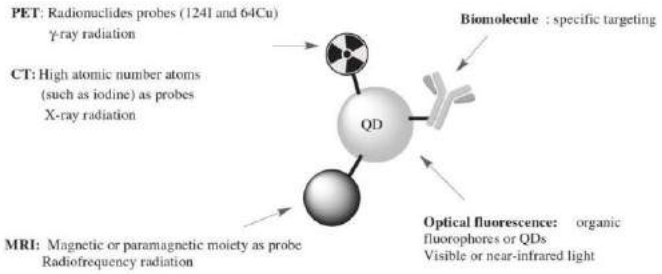

Figure 1. Characteristics of some diagnostic image techniques (PET, CT, MRI and optical fluorescence imaging). Adapted with permission from [4], R. Hachani, et al., *Nanoscale* 5, 11362 (2013). © 2013, Royal Society of Chemistry.

Thus, when the semiconductor materials are exclusively confined in three dimensions, they are called quantum dots. The cadmium selenide (CdSe) bulk, for example, has an exciton Bohr radius approximately $a_B = 5$ nm, thus we only have CdSe QDs if the a_B was less than 5 nm [17].

QDs with different sizes can present light emission from the ultraviolet (UV) to the infrared (IR), even if they have the same chemical composition. This is a consequence of the quantum confinement effect, that changes the E_g [15], which is higher as smaller is the QDs' size, as represented in Figure 2. In other words, after the absorption processes, the electrons return to VB and QDs' emission is proportional to their band gap. Thus, as energy is inversely proportional to the fluorescence wavelength, this means that the larger the QD, the smaller is the E_g and the more toward the red end of the spectrum is its corresponding fluorescence emission [31].

QDs used for biological applications are usually aqueous colloidal nanoparticles. Their nanocrystals structures are usually defined as a core/shell type (Fig. 3), where the core is responsible for fundamental optical properties of the nanoparticle, while the shell is used to improve their optical properties and reduce the chemical effects associated to the environment. The shell assures a physical separation of the core, and is usually composed by another semiconductor that presents an E_g higher than that of the core. Consequently, the optical properties of the nanoparticle become less sensitive to changes induced by medium, for example, the presence of oxidative species and the pH [14, 33].

For QDs' application in the life science, in which fluorescence in the visible/infrared region is usually required, both core and shell are commonly composed of elements from the II B and VI A groups of the Periodic Table (which correspond to groups 12 and 16 in the new International Union of Pure and Applied Chemistry (IUPAC) scheme). The importance of QDs for biophotonic applications is their use as fluorescent probes to replace organic dyes, since they present several advantages, such as [26, 34–39]:

- Photostability: QDs can be 100 times more photostable than organic fluorescent dyes, i.e., this allow the researchers to monitor long-term biological processes in real time.
- QDs' broad excitation (absorption) band: only one light source is necessary at the UV/blue region to excite several QDs, which have different emission colors.
- QDs' emission bands are symmetric and narrow with full width at half maxima (FWHM) usually smaller than

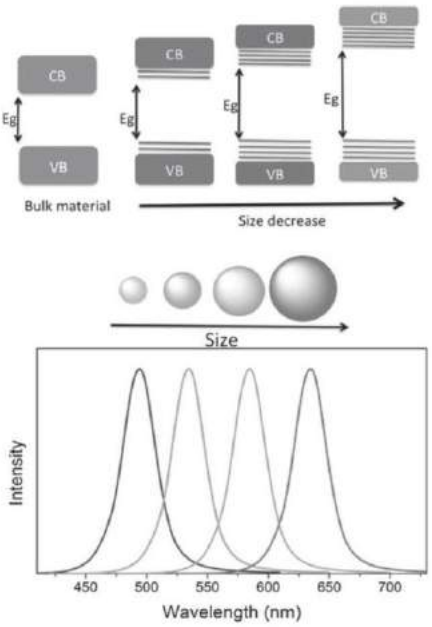

Figure 2. (A) Illustration of the quantum confinement effect with the size decrease that occurs in semiconductor materials of direct band. Energetic levels distribution of the bulk materials in the form of bands; CB = conduction band, VB = valence band, E_g = band gap. (B) Emission spectrum in function of the QD size with the same composition; the colored spheres represent the particle size.

Figure 3. Schematic representation of a core–shell quantum dot functionalized and conjugated with a biomolecule.

50 nm, which can provide more colors in multi-staining methods avoiding cross-talking.

During the colloidal synthesis, the QDs are coated by either organic or inorganic compounds, which are called stabilizing or functionalizing agents [17, 40–43]. They keep the nanoparticles separated from each other preventing precipitation and agglomeration, resulting in stable QDs' suspensions [17, 31]. The main classes of organic molecules used, in aqueous media, as QDs' functionalizing/stabilizing agents are alkyl-thiol molecules, such as mercaptopropionic acid (MPA), mercaptoacetic acid (MAA) and mercaptosuccinic acid (MSA), dihydrolipoic acid (DHLA), cysteine (CYS), cysteamine (CYSAM) and different mercaptodithiols [44]. In organic synthesis, the QDs' functionalizing/stabilizing agents utilized possess long alkyl chains such as tri-n-octylphosphine oxide (TOPO) and hexadecylamine [45].

The QDs' active surfaces promoted by the functionalizing agents allow the QDs' interaction with biomolecules and/or other nanoparticles, enabling the QDs to be useful systems to site-specific biological applications or to develop multimodal image probes. The association/conjugation of QDs to biomolecules is also called bioconjugation [46]. The (bio)conjugation procedures can be carried out by adsorption or by covalent coupling to the systems. Nowadays, the main bioconjugation strategies in aqueous media are performed between carboxylic and amine groups using EDC (1-ethyl-3-(3-dimethylaminopropyl)carbodiimide) and sulfo-NHS (*N*-hidroxysulfosuccinimide), amine–amine using glutaraldehyde, disulfide bonds, and streptavidin-biotin interaction [14, 44, 47, 48]. QDs have been already associated with several biomolecules as fluorescent markers for biological applications [49–52].

Recently, the number of published works involving cell-specific labeling has increased. Some of these works, employing bioconjugated QDs, have been performed for a better comprehension of the antigen expression patterns on the cell surface [52], and also to study proteins or carbohydrates expressions to the comprehension of cell biology in some diseases, such as the cancer [53–55]. Cabral Filho et al. [54] conjugated aqueous CdTe QDs with transferrin (Tf) to study the expression of transferrin receptors (TfRs) in HeLa cells (human epithelial cervical carcinoma) and two glioblastoma cells lines, U87 cells (human primary glioblastoma), and DBRTG cells (human recurrent glioblastoma). The authors showed that HeLa and DBTRG cells present a large amount and a higher extent of TfRs internalization when compared to U87. Furthermore, using a TfR saturation assay, the authors concluded that DBRTG have a faster recycling of the TfR on the cell surface when compared to other two types. The results suggest that the TfR have an important role in cancer maintenance and in recurrent situations. Moreover, the studies about the molecular aspects of cancer cell biology can help in developing more effective therapeutic methods.

Furthermore, QDs conjugated to biomolecules have been used successfully to study the glycoconjugates on microbials cells, such as fungus [56] and bacteria [57]. These studies can help to optimize phototherapy protocols for microbial opportunistic infections. Tenório et al. [56] employed QDs conjugated with ConA (concanavalin A lectin) for understanding cells and biofilm-forming organisms of *Candida albicans*, a human opportunistic fugal pathogen. The authors showed that yeasts, hyphae cells, and biofilm structures were efficiently and specifically labeled indicating that glucose and manose are present in these structures. This work opens new possibilities to monitor glycoconjugates by fluorescence, which can help to improve phototherapy protocols for this kind of fungus.

However, QDs' conjugation with molecules or other nanoparticles to obtain bimodal nanoparticles is still considered a challenge, due to some remaining challenges, such as (1) the conjugation process cannot denature the molecule or cannot affect the nanoparticles' properties; (2) the binding of QDs with biomolecules or with other nanoparticles cannot dissociate during the application in biological systems, and (3) nonspecific interactions cannot occur between conjugated and biological systems [14]. For these reasons, many studies are being carried out to improve the conjugation procedures in an attempt to form bimodal nanostructured systems with high stability, versatility, and the ability to obtain images with high quality and specificity [58–61].

2.2. Magnetic Resonance Imaging (MRI)

MRI has become an indispensable tool in the clinical diagnostic area. This technique present several advantages compared with other clinical image techniques, such as high spatial resolution (0.2–0.3 mm), producing images with fine anatomic details, and it is a non-invasive technique, since it does not use ionizing radiation [62, 63]. The first demonstration that nuclear magnetic resonance (NMR) could be used to distinguish tumors and normal tissues was performed by Raymond [64]. This author showed that the nuclear magnetic relaxation times, T_1 and T_2, are distinct for normal and malignant tissues. After that, the MRI was first demonstrated in 1973 by Paul Lauterbur [65].

The NMR signal related to body water protons (^{1}H) is used to generate the MRI images. The reason for monitoring the ^{1}H water molecules is mainly due to the natural abundance of water in the live organisms and the high sensitivity of hydrogen protons to NMR. The sensibility of the ^{1}H atoms (present in the water molecules of the tissues at different concentration and mobility) to the magnetic field allows the detection of tumors and anomalies in the soft tissues of the body by the differentiation of the images of normal tissue and those which have some morphological or metabolic alterations [64–66]. In abnormal tissues, the values of intrinsic nuclear magnetic relaxation times (T_1 and T_2) change, consequently changing the images obtained.

Briefly, when the positively charged spinning nucleus of the hydrogen atom is in the presence of an external magnetic field (B_0), a spin alignment occurs, generating a resultant magnetization M_0, which is parallel and proportional to B_0. In equilibrium $M_0 = M_z$, where z is the longitudinal axis. To be able to measure M_0, it is necessary to apply a pulse of radio frequency oscillating in the Larmor frequency (or precession frequency) of the ^{1}H, in order to divert M_0 to the xy plane (transverse). Subsequently, the protons release the absorbed energy (at radio wave region) returning to the equilibrium state (the original alignment), a process that is known as relaxation. The relaxation process is modulated by two exponential time constants, T_1 and T_2, which depend on the physical and chemical properties of the tissues. The T_1, known as longitudinal or spin-lattice relaxation, reflects the relaxation due to the energy loss for the neighborhood, and T_2, known as transverse or spin–spin relaxation, is the relaxation due to the interactions between the spins (dipolar interactions). Generally, T_1 gives information about the recuperation velocity of the system's magnetization parallel to the static magnetic field after a perturbation is applied. And, T_2 is related to the quickness of coherence loses of the magnetization in the transverse plane to the static magnetic field and is smaller than T_1 [67]. In practice, this results in differences on the generated image for local chemically and/or morphologically different environments [21, 63, 68].

In order to enhance the quality of the generated images, contrast agents (CAs) are highly administrated in clinical procedures. These MRI CAs must contain paramagnetic or superparamagnetic ions. The most MRI CAs approved for clinical use are based on paramagnetic chelates containing a lanthanide ion, namely gadolinium (III), and iron oxide particles [69]. Usually, contrast agents are classified as T_1 or T_2 MRI CAs, depending on whether they affect mainly the longitudinal (T_1) or the transverse (T_2) relaxation times of the water protons, correspondently. Contrast agents containing gadolinium and manganese ions are commonly T_1 contrast agents, while iron oxides particles are T_2 contrast agents [67].

The Gd^{3+} ion has specific physical properties that are suitable for reducing mainly the longitudinal (T_1) proton relaxation times of surrounding molecules, specifically water molecules protons. Since the Gd^{3+} ion undergoes a rapid hydrolysis at physiological pH, producing insoluble $Gd(OH)_3$ and accumulates in bones and liver, a high thermodynamic and kinetic stability of the complexes used as MRI CAs are required, and these properties are fundamental for their use *in vivo*. Iron oxide particles possess several properties that make them good candidates to be used as MRI contrast agents, and their low toxicity makes them attractive alternatives to gadolinium-based contrast agents [70].

The efficiency of the MRI CAs is measured in terms of the relaxivity (r_i, in $s^{-1} \cdot mM^{-1}$, $i = 1,2$) that indicates their ability to decrease the relaxation times of the water protons per unit (mM) concentration of the paramagnetic ion. Higher values of r_1 and r_2 correspond respectively to smaller T_1 and T_2 values. Longitudinal and transverse relaxivities (r_1 and r_2, respectively) are generally different, and they depend on the magnetic field strength [70]. Relaxivity can be defined as the increase in the water protons relaxation rates provoked by 1 mmol·L^{-1} of the para- or superparamagnetic ion [71]. The relaxivity can be obtained by Eq. (1):

$$r_{1,2} = \frac{R_{1,2}^{obs} - R_{1,2}^{dia}}{C} \quad (1)$$

where $R_{1,2}^{obs}$ is the longitudinal or transverse relaxation rate ($1/T_{1,2}$) of the water protons observed in the presence of the para- or superparamagnetic ions, $R_{1,2}^{dia}$ is the diamagnetic longitudinal or transverse relaxation rate ($1/T_{1,2}$) of the water protons (in the absence of the para- or superparamagnetic ions), and C is the concentration of the para- or superparamagnetic ions [72]. Usually, water protons' longitudinal relaxation time are around 2500 ms, and its transverse relaxation times around 3000 ms.

The enhancement of the contrast is obtained when one tissue has either a higher affinity for the CAs or a higher vascularity than another one. Diseased tissues, such as tumors, are metabolically different compared with healthy tissues, and they have a much higher uptake of the contrast agents, resulting in a higher contrast in MRI images [73].

Despite its high spatial resolution (0.2–0.3 mm), the investigation of molecular events at the cellular level using MRI is limited, because it requires a relatively large local concentration of CAs to achieve an observable contrast enhancement. Considering the molecular structures that usually are used as CA, this is not an easy task. Recently, one of the approaches to overcome this limitation is the use of nanoparticulate systems as MRI contrast agents, which could be able to increase the local concentration of paramagnetic or superparamagnetic ions to each target site [74–76]. Several nanosystems have been developed as CA for MRI such as polymeric nanoparticles [77–79], micelles [80, 81], carbon nanotubes [82–84], liposomes [85, 86], dendrimers [87, 88], proteins [89, 90] and gold nanoparticles [91, 92]. Their r_1 values can be at least 100 times higher per unit CA than those values found to molecular clinical approved MRI CA, such as $[Gd(DTPA)]^-$. The r_2/r_1 ratio is dependent on the particles size, water content, and porosity and can give us the classification of the CAs. Depending on the r_2/r_1 ratios and magnetic field used, they can thus be useful as CAs for T_2-weighting (negative contrast) and/or T_1-weighting (positive contrast) imaging [93]. A contrast agent enhances the positive contrast (T_1) when the $r2/r1$ is around 1–2, and negative CAs usually have r_2/r_1 ratios higher than 10 [94].

The work of Turner et al. [79] is one example of the improvement of the relaxometric properties by preparing nanostructured CAs. They prepared a micellar nanoparticle by aqueous assembly of a diblock copolymer and conjugated them to a Gd-DTPA complex derivative. The nanoparticle prepared presented a r_1 value of 21.2 $mM^{-1}s^{-1}$ (at 0.47 T and 25 °C), which shows an improvement when compared to the Gd-DTPA complex (r_1 = 4.3 $mM^{-1}s^{-1}$ at 0.47 T and 25 °C).

Covalent functionalization of carbon nanotubes with DTPA chelates followed by complexation with Gd^{3+}, originated CAs nanostructured with an improvement in r_1 value by a factor of two, when compared with the DTPA-Gd^{3+} complexes [84].

Other example is the report of Ferreira et al. [92], where they attached DOTA (1,4,7,10-tetraazacyclododecane-1,4,7,10-tetraacetic acid) derivatives complexed with gadolinium to gold nanoparticles, and they observed an enhancement in the r_1 value (at 0.7 T) of at least three times for the nanoparticle system when compared to the bare chelates.

Furthermore, nanoparticles can be important for the development of specific contrast agents for MRI. Several nanoparticles have a functionalized surface that allows the conjugation to biomolecules, conveying the CA to a specific target, which will be fundamental to monitoring cellular events *in vivo* [95].

3. BIMODAL NANOSTRUCTURED PARTICLES

The development of bimodal nanostructures, containing QDs for optical and magnetic resonance images, relies on the design and further preparation of nanomaterials that will present both technique properties. To prepare new particles as potential bimodal nanoprobes for biological applications, some criteria must be considered. The bimodal probes must have [96]:

- High relaxivity and quantum yield;
- Appropriate size for the application
- A simple and cheap preparation method
- Low toxicity
- Kinetic and thermodynamic stability, to avoid inaccurate images and/or toxicity

One of the QDs advantages is their chemically active surface, allowing the conjugation with a variety of molecules and/or other particles, which can originate new multimodal nanostructured particles. The most common approaches used to prepare bimodal nanostructures containing QDs for optical and MR images are their association with iron-oxide based nanoparticles by doping QDs with paramagnetic ions and by their association with paramagnetic chelates. The interest in bimodal nanoparticles for optical and magnetic resonance imaging containing QDs aroused attention throughout the last 10 years. In the next sections, we will present a review of the development of materials aimed at bimodal properties, giving special attention to the maintenance of optical/relaxometric or magnetic properties and their application in biological systems.

3.1. Quantum Dots–Iron Oxide Nanoparticles

QDs associated with magnetic nanoparticles (MNPs) have generated great interest as a new class of materials, because this association can provide a combination of optical and magnetic properties in a single material, enabling simultaneous biolabeling/imaging, cells sorting/separation and therapy/diagnostic (nanotheranostic particles) [97, 98]. There are many examples of multimodal imaging agents containing MNPs, the superparamagnetic iron oxide nanoparticles (SPIONs) being the most used, since the US Food and Drug Administration approved them as contrast agents for MR [I.99].

Bulk iron oxide is classified as a ferromagnetic material, because it presents a permanent magnetization, even without an external magnetic field [100, 101]. Decreasing particles' size from macroscopic to nanoscale, their physical and chemical properties are changed. When iron oxide particles are reduced to a few nanometers (~1–20 nm), each particle behaves as a magnetic single-domain, so their magnetic properties are considerably altered, due to quantum size effects and surface area increase, becoming superparamagnetic [71, 97, 100]. SPIONs are in a uniform magnetization state, which means that after removal of the external magnetic field they lose their magnetization, making them dispersed and diminishing their tendency to aggregate [98].

SPIONs possess an iron oxide core, which provides their magnetic properties, such as the superparamagnetism. The more common iron oxide cores are the magnetite crystalline phase (Fe_3O_4) and its fully oxidized form, the maghemite crystalline form (γ-Fe_2O_3). However, the most used iron oxide core to produce bimodal nanoparticles is the magnetite type, because it has better ferromagnetic response presenting a saturation magnetization (*Ms*) about 92–100 emu · g^{-1} at 300 K, while the maghemite form presents a *Ms* about 60–80 emu · g^{-1} at 300 K [101]. The core is, usually capped with a biocompatible polymer, which shields the core from the surrounding environment and allows the nanoparticles' functionalization, enabling the attachment of other particles or molecules [102].

There are several synthetic methodologies for the SPIONs preparation, such as coprecipitation, microemulsion, hydrothermal processes, electrochemical deposition, sonochemical reactions, thermal decompositions, gas phase depositions and sol–gel processes. The most used methodology is coprecipitation since it is a simple and less expensive method. In this methodology, iron salts in both oxidative stats (ferric and ferrous ions in 2:1 molar ratio) are added to an alkali solution, under inert atmosphere, and the SPIONs are obtained by precipitation [97, 102, 103].

Today, iron-based MNPs are attracting much attention from several research groups, since they have found application in many fields, such as in the material and life sciences. MNPs have been used for *in vivo* biomedical applications, such as contrast agents for MRI, therapeutic agents for hyperthermia, drug carriers, and in radionuclide therapy [104–108].

For biological applications, some characteristics need to be considered: (1) the probe needs to be hydrophilic and stable in water at physiological pH, (2) it should have a narrow size distribution, and (3) it must have a surface coated with biocompatible polymers and a chemical active surface for conjugation with other molecules [98, 102, 109].

Especially for MRI applications, the probes used produce an image contrast enhancement. Although SPIONs can affect the longitudinal relaxation time (T_1), they affect primarily the transverse relaxation time (T_2) of the water protons. Usually, SPIONs have greater transverse relaxivity (r_2) than longitudinal relaxivity (r_1), producing hypointense (dark) signal in MRI [67, 70, 110].

Magnetic properties of SPIONs arise from the presence of Fe^{2+} and Fe^{3+} ions and depend on several factors, such as size, composition, shape, and crystallinity. The magnetic characterization is usually performed by saturation

magnetization (*Ms*) measurements, which indicates the magnetization magnitude of the material when submitted to an external magnetic field. The *Ms* value indicates the higher magnetization of the material, meaning that all the single domains are aligned with the field. However, the efficiency of CAs for MRI is generally discussed based on the materials relaxivity values (r_1 and/or r_2). Many researchers working with SPIONs do not present the relaxivity values and only measure the *Ms* of the material. A direct correlation between saturation magnetization and relaxivity does not exist, although a higher *Ms* will increase the local magnetic field, affecting the surrounding protons and enhancing the MRI signal [111, 112].

Since *Ms* and relaxivity are related, the same factors that affect the magnetization will also affect their ability to reduce T_2. Namely, this ability increases with their size, since their magnetic properties are attenuated in the surface, a smaller ratio between the atoms near the surface and ones in the core will improve their T_2 reduction capacity. The surface coating of the nanoparticles can also affect their CA efficiency, and it has been observed that T_2 contrast decreases with increasing the coating thickness [67, 111, 113, 114].

Several reports demonstrated the association of QDs and SPIONs aimed at the generation of bimodal nanoparticles. In an attempt to overcome the challenges of the bimodal nanoparticles' production using SPIONs and QDs, most works have been concerned with the optimization of the binding process between these nanoparticles. These studies include methodologies to insert QDs and SPIONs in silica spheres [115, 116], micelles [117] and polymer nanospheres [118], mediated by cross-linkers [119, 120] or electrostatic interaction [99, 121, 122].

In this section, we focus our discussion on the different bimodal nanoparticles reported in the literature for biological applications, composed by QDs and SPIONs, which contain their optical and magnetic properties. For better comparison between the bimodal systems developed, we organized them by their synthesis strategy.

3.1.1. Association of QDs and SPIONs by Covalent Binding

One approach to associate QDs and SPIONs is to bind covalently the two nanoparticles using conjugation strategies and cross-linkers (Fig. 4) [119, 120, 122–124].

To our knowledge, the first work describing the formation of a bimodal system by covalently associating cadmium selenide/zinc sulfide (CdSe/ZnS) QDs and SPIONs (γ-Fe_2O_3) was reported by Wang et al. [125], using thiol groups. Since then, other groups have prepared bimodal nanoparticles using this methodology.

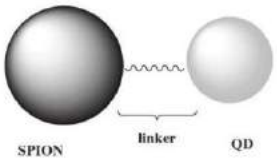

Figure 4. Schematic representation of the covalent association between QDs and SPIONs.

The same approach to bind cadmium telluride (CdTe) QDs to Fe_3O_4 was adopted by Sun et al. [126], where thioglycolic acid (TGA)-stabilized CdTe QDs were linked to the surface of silica (SiO_2)-coated SPIONs. The nanocomposites prepared presented an emission similar to the precursors QDs, and an *Ms* of 2.26 emu · g^{-1}, which is smaller than the *Ms* of bare Fe_3O_4 nanoparticles (49.97 emu · g^{-1}). Then Fe_3O_4@SiO_2-CdTe magnetic/fluorescent nanocomposites were conjugated to the anti-CEACAM8 antibody, which recognized the CEACAM8 receptor on the HeLa (adenocarcinoma cervical human) cell membrane, using *N*-hydroxysuccinimide (NHS) as a cross-linker. The bimodal nanoparticles-anti-CEACAM8 were successfully employed for immune-labeling and fluorescent imaging of HeLa cells.

Kale et al. [119] prepared bimodal nanoparticles by controlled synthesis from CdTe QDs decorated with magnetite nanoparticles using dodecyl amine (DDA) as a linker. CdTe QDs functionalized with mercaptopropionic acid (MPA) were prepared in the presence of the Fe_3O_4 core functionalized with DDA. The bimodal nanoparticles presented a maximum emission at 531 nm with a fluorescence quantum yield (QY) of 18%, in water. The magnetite decorated with CdTe retained the superparamagnetic property of the core, presenting an *Ms* of 44 emu · g^{-1}. The bimodal nanoparticles were conjugated with anti-EGFR antibody and used to specific separation and imaging of positive T leukemic cells (Molt-4), utilizing a mixed cell suspension of Molt-4 and myelogenous leukemia (K562) cells. This specific separation was possible since the EGFR is highly expressed on Molt-4 cells, whereas K562 cells lack this receptor. The results showed that these bimodal nanoparticles exhibited an excellent potential for the magnetic separation and for acquiring fluorescent images of positive leukemic cells (Molt-4).

Koktysh et al. [99] demonstrated the preparation of bimodal nanoparticles by covalent binding of glutathione-coated visible CdTe/CdS (600 nm) or near-infrared (NIR) light-emitting CdHgTe/CdS QDs (800 nm) to Fe_3O_4 nanoparticles functionalized by dextran, which is a biocompatible stabilizing agent commonly used to increase the CAs retention on the blood circulation. According to TEM images, the bimodal nanoparticles showed an average size of around 7.8 nm. Furthermore, inductively coupled plasma (ICP) and energy-dispersive X-ray spectroscopy (EDS) confirming the presence of Fe > 80% and Cd > 13% for both techniques, and the optical characterization showed no changes in the emission spectrum profile. The authors reported that none toxicity of the particles was observed in mice. The *ex vivo* images showed that the particles were accumulated in the lungs and subsequently in the draining lymph nodes. At the end, the authors stated that the bimodal nanoparticles are a combined system that could be used for simultaneous optical and MR images; however, the authors did not present magnetic properties of the systems or magnetic resonance images.

3.1.2. Coating QDs and SPIONs with Silica Layers

Another approach for the synthesis of bimodal nanoparticles is the encapsulation of QDs and magnetic nanoparticles in an outer shell of silica (Fig. 5) [127–133].

Salgueiriño-Maceira et al. [134] incorporated Fe_3O_4/γ-Fe_2O_3 nanoparticles coated with silica and CdTe QDs in an outer shell of silica. The bimodal particles presented a diameter around 220 nm an *Ms* of 1.34 emu · g^{-1} at room temperature and showed efficient fluorescence. The same approach was used by Li et al. [131], avoiding the direct interaction of QDs and MNPs, improving the optical and magnetic response of the bimodal nanosystem. They prepared magnetic-fluorescent dual-functional nanoparticles with a mean size of 60 nm, *Ms* of 3.2 emu · g^{-1} and an emission maximum at 618 nm. In both works the authors presented the bimodal nanoparticle, with a silica shell, as a new bimodal tool for biological application. Further, in 2009 the same research group [135] also used the reverse microemulsion approach to prepare bimodal nanoparticles in order to label specifically prostate cancer cells. The bimodal nanoparticles (with 50 nm of mean diameter and an *Ms* = 3.24 emu · g^{-1}) were functionalized by 3-aminopropyltrietoxysilan (APS) and conjugated to single chain variable fragment antibody (scFv) of human γ-seminoprotein-specific, using glutaraldehyde as coupling agent. The specific bimodal nanostructures were applied in human embryonic kidney cells (HEK293) as a negative control and human prostate cancer cells (LNCaP) as a positive test, since LNCaP cells have an overexpression of γ-seminoprotein. Both cells were analyzed by fluorescence microscopy. Furthermore, the authors also injected LNCaP cells subcutaneously into female nude mice, and then the animals were analyzed by MR and fluorescence images. The results showed that bimodal nanoparticles-scFv did not label HEK293 cells, while LNCaP cells were labeled both on the membrane and also inside the cells. Moreover, the bimodal nanoparticles did not present apparent toxicity. In mice after 6 h, bimodal nanoparticles-scFv were concentrated in the tumor tissues and in other organs, such as the liver, lung, heart, and kidney. However, after 24 h, most of the nanoparticles disappeared from the organs of mice and were mainly observed in local tumor tissues, both by fluorescence imaging as MRI. The authors also explored the hyperthermia using bimodal nanoparticles-scFv and found that the number of LNCaP cells destroyed was proportional to the concentration of the nanoprobes in the medium.

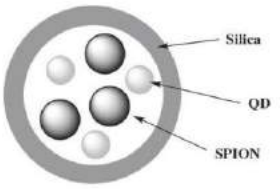

Figure 5. Schematic representation of QDs and SPIONs encapsulated in an outer silica shell.

In other works of the same group [116], they used the amino-modified bimodal nanoparticles (Fe_3O_4–CdTe@SiO_2) to label mesenchymal stem cells (MSCs) in gastric cancer, *in vitro* and *in vivo*. *In vitro* studies showed that the fluorescent and magnetic resonance signals of the labeled cells, with the bimodal nanoparticles, were stable for up to 14 days. Then the *in vivo* studies were performed by the intravenous injection of the MSC labeled with bimodal nanoparticles in nude mice containing gastric cancer. Bimodal nanoparticles distributions in the whole body were monitored for a period of 14 days after injection by using *in vivo* image system (IVIS) and MRI. It was observed that the fluorescent and MR signals in the tumor tissue increased gradually from day 7 to 14 post-injection. The hyperthermia therapy study showed that only amino-modified bimodal nanoparticles presented tumor shrinkage while bimodal nanoparticles did not show evident alteration.

Ma et al. [136] synthesized bimodal nanoparticles from two color emission CdSeTe/CdS hydrophobic QDs (λ = 600 nm and λ = 780 nm) and Fe_3O_4 nanoparticles. To obtain the bimodal nanoparticles, authors grew a silica layer in a Fe_3O_4 MNP core, forming a MNP bead. Then they added the QDs and tetraethyl orthosilicate (TEOS) to form a thin shell of QDs/silica around the MNP beads. Bimodal nanoparticles have an average size of about 150 nm and maxima emission at λ = 600 and λ = 750 nm. The authors referred that these bimodal nanoparticles acted predominately in T_2-weighted images, because the nanoparticles presented relaxivity values for r_1 and r_2 about 13 and 1914 mg · L^{-1} · s^{-1}, respectively. For specific labeling, they conjugated the bimodal nanoparticles to anti-HER2 (human epidermal growth receptor 2 antibody) antibody using EDC. To confirm the ability of the bimodal nanoparticles functionalized with anti-HER2 antibody to label specific target, the authors performed *in vivo* and *in vitro* tumor imaging. Breast cancer tumors were induced on nude mice by transplantation of green fluorescent protein (GFP) human breast cancer cells (KPL-4 cells). The specific binding *in vitro* was confirmed by fluorescence microscopy and fluorescence cell sorting analysis and for *in vivo* images, they used near-infrared fluorescence (NIR-fluorescence) and MR imaging. The authors presented an efficient method to produce bimodal nanoparticles that can be used for biomedical applications and as diagnostic methods of several diseases.

Chen et al. [133] also prepared magneto-fluorescent nanoparticles, mixing hydrophobic CdSe/CdS QDs and Fe_3O_4 SPIONs, and transferred them to aqueous solution using the surfactant dodecyltrimethylammonium bromide (DTAB). Briefly, the authors synthesized the bimodal nanoparticles in four steps: (1) micelle formation in chloroform by using DTAB as a surfactant with a random magnetic core, (2) a supercrystalline magnetic core formation by using poly(vinylpyrrolidone)/ethylene glycol (PVP/EG) under heating at ~80 °C and stirring, (3) silica shell growth using TEOS, and (4) finally the silica-bimodal nanoparticles were coated by polyethylene glycol (PEG). In this work, the authors demonstrated that after coating with PEG, silica-coated-bimodal nanoparticles showed an efficient bimodal image probe for *in vivo* multiphoton (MP) and MRI, with a size of 120 nm, an *Ms* of 15.2 emu · g^{-1} (at room temperature), and a QY of 12% in water. Intravital multiphoton

microscopy images were obtained through a cranial window in model C_3H mice after injection of murine cancer cells stage IV (MCaIV). Figure 6 shows the intravital MP images, where in Figure 6(A) shows MP image before injection of bimodal nanoparticle, Figure 6(B) after 4 h of injection, and Figure 6(C) after 24 h of injection. MRI (Fig. 7) was obtained in a 9.4 T magnet, before (Fig. 7(A)) and after 24 h (Fig. 7(B)) of the bimodal nanoparticles injection.

3.1.3. Incorporation of QDs and SPIONs in Polymer Beads

Another approach for the preparation of bimodal nanoparticles containing QDs and SPIONs is the incorporation of these nanoparticles in polymer beads (Fig. 8) [118, 137–142].

Although there are many reports using this methodology to prepare bimodal nanoparticles, to our knowledge only one research group applies them in biological studies. Song et al. [118] synthesized bimodal nanoparticles by an organic route, using an hydrazine-treated poly-(styrene/acrylamide) copolymer nanosphere. The bimodal nanoparticles were constituted of CdSe/ZnS QDs and the Fe_2O_3. The bimodal nanospheres were conjugated to avidin that was associated to a biotynilated goat anti-mouse IgG (Fc specific polyclonal antibody), and then, mouse anti-human anti-CD3 monoclonal antibody (mAb) or mouse anti-human anti-PSMA mAb, respectively. The authors demonstrated the potential of the bimodal system conjugated to the antibody for the detection and isolation of cancer cells. They used two complex samples containing Jurkat T cells (human peripheral blood leukemia T cells) and red blood cells (RBCs) and another containing LNCaP and RBCs as a control. The Jurkat T cells were bound to anti-CD3 mAb-coupled bimodal nanoparticles, and the LNCaP cells were bound to anti-human anti-PSMA mAb-coupled bimodal nanoparticles and separated using an external magnetic field. They reported that the conjugated nanoparticles were able to detect and extract two different types of tumor cells (leukemia cells and prostate cancer cells) from a complex sample. Therefore, the authors presented a simple and sensitive approach for detection and isolation of multiple cancer cells at early stages, *in vitro*.

3.1.4. Association of QDs to SPIONs by Electrostatic Interactions

The electrostatic interactions based on oppositely charged materials attraction was employed by some authors [122, 132, 143–145] to prepare magnetic-luminescent nanocomposites (Fig. 9).

Ahmed et al. [121] synthesized bimodal nanoparticles associating Fe_3O_4 and green CdTe QDs by electrostatic interaction. The bimodal nanoparticles were obtained with a mean size of 50 nm and an *Ms* of 65 emu $\cdot$ g^{-1}. The bimodal systems were incubated with human embryonic kidney cells (HEK293) and human epithelial colon cell line (LS174TK), after conjugation to antigen-binding fragment (Fab) region of hCC49 antibodies also by electrostatic interaction. The conjugated nanoparticles were specifically attached around the nucleus of LS174T cancer cells, while HEK293 cells presented no labeling around the nucleus.

Using the interaction of the metal coordination bonding to DNA, Lee and collaborators [146, 147] developed a new strategy for the preparation of bimodal nanoprobes. These authors linked QDs conjugated with platinum to magnetic nanoparticles (MNPs) functionalized with guanines (Fig. 10(A)), using the coordination bonding of Pt with the guanines. They used two QDs with different emission maximum (605 and 800 nm) and the association with the MNPs has not changed their emission properties. The bimodal nanoparticles prepared presented an average size of 50 nm (determined by DLS) and they were tested with HeLa cells. Fluorescence microscopy showed that the HeLa cells internalized these particles, and the nanoparticles were mainly located next to the nuclei (Figs. 10(B and C)). The magnetization curve showed that the magnetism of the MNPs was maintained after conjugation with the QDs. *In vitro* magnetic resonance images of HeLa cells incubated with QDs-MNPs conjugates showed the preservation of the magnetic properties of the bimodal systems (Fig. 10(D)).

3.1.5. Final Considerations About QDs–Iron Nanoparticles

Most authors cited in this section reported a decrease in the saturation magnetization (*Ms*) of the bimodal nanoparticles, when compared to the bare magnetic nanoparticles (Table 1). Table 1 also shows data from several research groups that employed different methodologies to associate QDs and SPIONs. They did not necessarily apply these systems; however we presented them as potential bimodal probes for biological applications.

3.2. Doped Quantum Dots

At the nanoscale range, the QDs structural stability, the electronic and photophysical properties can be changed by

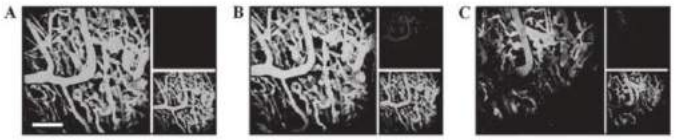

Figure 6. Intravital MP microscopy images of the cranial window. In (A) before injection, (B) 4 h after injection and (C) 24 h after injection of bimodal nanoparticles. Images from red and green channels are shown in small panels (top: red channel, bottom: green channel). Green emission signals was generated from fluorescein isothiocyanate–dextran (FITC–dextran) a blood vessel tracer and the red emission are generated by bimodal nanoparticles. Scale bar = 150 mm. Adapted with permission from [133], O. Chen, et al., *Nature Comm.* 5 (2014). © 2014, Nature Publishing Group.

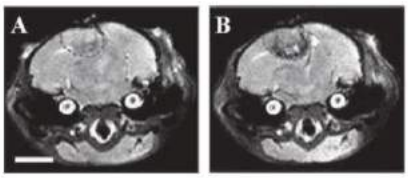

Figure 7. *In vivo* T_2-weighted MRI. In (A) before bimodal nanoparticles injection, and in (B) 24 h after bimodal nanoparticles injection. After 24 h post injection image (B) show clear tumor visualization (inside the red dashed line). Scale bar = 3 mm. Adapted with permission from [133], O. Chen, et al., *Nature Comm.* 5 (2014). © 2014, Nature Publishing Group.

any perturbation in the crystalline lattice. Thus, the incorporation of dopant ions in QDs can bring new properties that could lead to new advances for several applications. The control over size and shape in colloidal synthesis, developed so far, allowed the incorporation of transition metal ions in semiconductor QDs. In an effective doping procedure, the dopant ions will replace some atoms on the host crystal structure in the QD matrix [149–151]. However, nanocrystals try to purify themselves, and during their growth process, they tend to anneal out the dopants, since the impurities incorporation requires much more energy [152, 153].

As aforementioned, in non-doped QDs, an electron from the VB upon absorption of light goes to the CB, and its return to the fundamental state promotes the emission of a photon of wavelength related to the QDs' bang gap energy. The presence of impurities or high concentration of surface defects will increase the nonradiative decay pathways in a random way, which will decrease or quench the photoluminescence and change the expected spectral profile. The incorporation of dopants in QDs will create new defined electronic states inside the band gap region (between the VB and CB) (Fig. 11). Thus, it will decrease the energy separation between the CB and the VB, leading to adjustments in the relaxation pathways to the fundamental state, originating new luminescence properties. In other words, the doped QDs' emission will be red-shifted when compared to the non-doped QDs and the bandwidth will increase. Hence, QDs' optical and electronic properties can be tuned by controlling the dopant's type and concentration [150, 151, 154].

In the last years, there have been several reports on the preparation of doped QDs, using several transition metals and lanthanides ions, such as Mn, Co, Cu, Fe, Eu, and Yb, showing promising applications in biological imaging [155], MRI [6], solar cells [156, 157], light-emitting

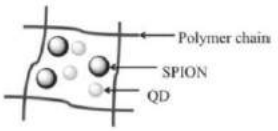

Figure 8. Schematic representation of the incorporation of QDs and SPIONs in polymer beads.

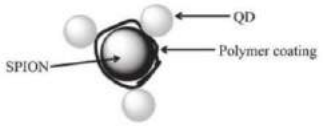

Figure 9. Schematic representation of QDs and SPION associated by electrostatic interactions.

devices (LEDs) [158, 159], biosensors [160, 161], and photocatalysis [162]. In this section we will focus our attention only on doped QDs developed simultaneously for optical and magnetic resonance imaging reported in the literature, which present optical and relaxometric studies.

For MRI proposes, QDs have been doped with Mn^{2+}, Gd^{3+}, and Fe^{2+}. Paramagnetic metal ions, with a large spin number, are often chosen as CA for MRI, since they have physical properties that are able to decrease the nuclear relaxation times of specific isotopes on the surrounding environment. The paramagnetic lanthanide ion most used is gadolinium, since it has seven unpaired electrons. Another metal ion widely used is manganese, which has five unpaired electron in its bivalent state. These ions, when used as CA, shorten the longitudinal relaxation time (T_1) of water protons, enhancing the T_1-weighted MR images [163, 164], while iron shortens the transverse relaxation time (T_2) of water protons, enhancing the T_2-weighted MR images. Therefore in this section we will discuss first the Mn^{2+} doped QDs, followed by Gd^{3+} and Fe^{2+} doped QDs.

3.2.1. Manganese-Doped QDs

The first QD doped with manganese was reported by Bhargava et al. [165], and the optical properties of ZnS:Mn were studied by these authors. These authors reported that incorporation of Mn^{2+} in QDs changed their optical properties, shifting the emission to the yellow emission region, which was being associated with the Mn^{2+} ions intrinsic electronic transitions. This means that after excitation of zinc sulfide (ZnS) QDs, a subsequent transfer of electron and hole into the electronic level of the Mn^{2+} occurs, leading to the characteristic emission of Mn^{2+}. Since then, several reports on the preparation of manganese doped QDs have appeared [151, 166–169].

Several authors reported the synthesis and the potential of QDs doped with manganese as bimodal markers for optical and MRI [155, 170, 171]. However, Wang et al. [172] were the first to present, simultaneously, the optical properties together with relaxivity measurements for these materials. These authors prepared core/shell QDs of CdSe/ZnS doped with manganese (CdSe/ZnS:Mn) by an organometallic route, with an average size of 4.7 nm (estimated by TEM). They achieved a dopant maximum of 6.2% (determined by elemental analysis), and they verified by electronic paramagnetic resonance (EPR) studies that the Mn^{2+} was incorporated into the shell. The nanoparticles, containing different amounts of Mn^{2+}, showed an emission centered from 570 to 650 nm. In organic solvents, these QDs presented a fluorescence quantum yield (QY) of 60%, but in water (after being coated with an amphiphilic polymer) the

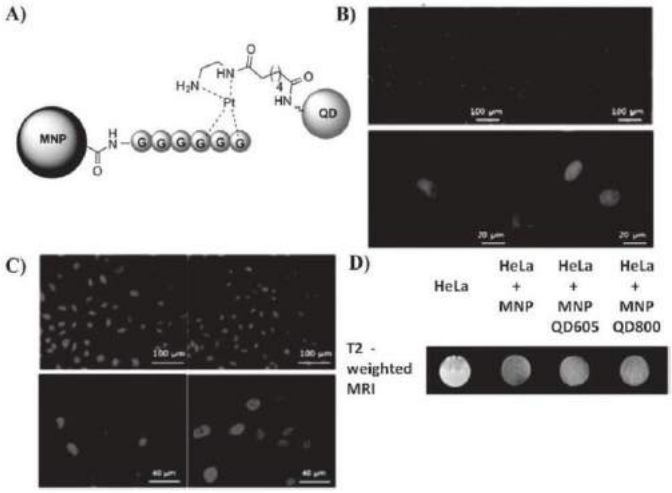

Figure 10. (A) Schematic representation of the bimodal system (MNP-QD) prepared by Lee et al. Fluorescence microscopy images of MNP-QD systems incubated with HeLa cells (B) with emission at 605 nm and (C) at 800 nm. (D) MRI results of HeLa cells incubated with MNP, MNP-QD with emission at 605 nm and 800 nm. Adapted with permission from [147], J. Lee, et al., *Analyst*, 140, 2864 (2015). © 2015, Royal Society of Chemistry.

QY decreased to 21%. The CdSe/ZnS:Mn also showed high longitudinal relaxivity value (r_1), being 18 mM^{-1} s^{-1} (at 7 T and room temperature) for the QD with 6.2% of Mn^{2+}. These authors have performed both optical and MR images incubating the water-dispersed nanoparticles (0.408 mM) with macrophages. They observed spots of luminescence in the cytoplasm of the cells by confocal microscopy, and a contrast enhancement of the incubated cells, compared with the unlabeled ones, by MRI. This means that the quantity of Mn^{2+} incorporated in the QDs was reasonable to produce images in both modalities, and the bimodal nanoparticle is suitable to be used in both optical and MR imaging.

ZnS QDs doped with manganese were prepared as a dual-imaging contrast agent, for optical and MR images, by Gaceur et al. [173]. These nanoparticles presented a 10% concentration of Mn^{2+} (estimated by X-ray Diffraction, XRD) with a diameter about 1.5 nm (determined by TEM). The ZnS:Mn showed a blue-green emission, with a broad band centered at 466 nm with a shoulder at 507 nm. As opposed to previous studies [165], in this report no emission arising from the Mn^{2+} electronic level (580–600 nm) was observed. These authors attributed this fact to concentration quenching, i.e., the number of Mn^{2+}–Mn^{2+} pairs increased when the Mn^{2+} concentration was high, which resulted in an

Table 1. SPIONs saturation magnetization values before and after conjugation to QDs.

Synthetic strategy	Bimodal nanoparticle composition	Size (nm)	*Ms* of bare SPIONs (emu · g^{-1})[a]	*Ms* of bimodal nanoparticles (emu · g^{-1})[a]	Reference
Cross-linking	Fe_3O_4@SiO_2-CdSe/ZnS	25	67.7	2.38	[124]
	Fe_3O_4@SiO_2-CdTe	30	40.97	2.26	[126]
	SPION-CdS	100	55	9.5	[120]
	Fe_3O_4-CdTe/CdS	11	62	44	[119]
Silica coating	(Fe_3O_4/γ-Fe_2O_3@SiO_2-CdTe)@SiO_2	220	54	1.43	[134]
	(Fe_3O_4-CdTe)@SiO_2	50	54	3.21	[130]
	Fe_3O_4@SiO_2-CdSe/ZnS@SiO_2	60	45.2	3.2	[131]
	(γ-Fe_2O_3-CdSe)@SiO_2	11	26[b]	0.4[b]	[148]
	(Fe_3O_4-CdSe/CdS)@ SiO_2	100	63.7	15.2	[133]
Polymer coating	(Fe_3O_4-CdTe)chitosan	65	77	11	[139]
Electrostatic interactions	Fe_3O_4@SiO_2-CdSe	~100	68	11.7	[132]
	Fe_3O_4@SiO_2- CdTeS	100	38.26	9.09	[144]
	CdTe–Fe_3O_4	50	71	65	[121]

Notes: [a] at room temperature–300 K. [b] at 15 K.

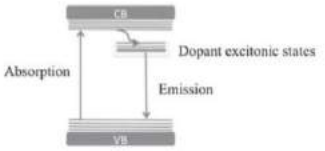

Figure 11. Scheme illustrating the creation of electronic states inside the band gag region, due to the incorporations of dopants in QDs and its decay pathways.

increase in the non-radiative decays from the excited states being observed. Relaxometric studies gave a value of r_1 of 20 mM^{-1} s^{-1} (at 3 T and 25 °C). These nanoparticles were used in an intracellular uptake study using Chinese hamster ovarian (CHO) cells, and it was observed by confocal microscopy that after 24 h of exposure, the QDs were internalized and were dispersed in the cytosol. Cytotoxic studies showed that these QDs did not hinder the cell viability and proliferation (at concentration of 0.05 mM of Mn^{2+}).

Jing et al. [174] prepared core/shell CdTe/ZnS QDs doped with manganese ions using colloidal aqueous synthesis. These nanoparticles presented a diameter of 4.3 nm (estimated by TEM) and different dopant levels were used (4.7–9.7%, determined by inductively coupled plasma optical emission spectrometry (ICP-OES)). EPR studies confirmed that the dopant ions are in the surface region distributed within the ZnS shell. Fluorescence studies showed that CdTe/ZnS:Mn emitted at 650 nm, and their QY decrease with increasing the dopant proportion. This QY decrease may be explained by the presence of some manganese ions in the core/shell interface. The QDs with 4.7, 7.5, and 9.7% of Mn^{2+} presented ionic longitudinal relaxivity values of 10.7, 6.5, and 5.4 $mM^{-1}s^{-1}$ (per Mn^{2+}, at 3 T and room temperature). These results showed that ionic relaxivity values decrease with increasing Mn^{2+}.

Lin et al. [175] prepared cadmium-free QDs with paramagnetic properties. These authors synthesized an I–III–VI ternary core, copper indium disulfide ($CuInS_2$), capped with manganese-doped ZnS, by colloidal organic synthesis. ICP confirmed that they were able to incorporate 0.2 to 2.3% of Mn^{2+}, by EPR was confirmed that the Mn^{2+} was present in the ZnS shell, and by TEM was observed that these nanoparticles have a diameter of 4 nm. These QDs emitted around 600 nm and their QY in organic solvent was 52%, but when transferred to an aqueous phase the QY decreased to 18%. Relaxivity measurements presented values between 5.1 and 7.2 mM^{-1} s^{-1} (3 T at room temperature), depending on the quantity of Mn^{2+}. In order to show that these QDs can be used as dual-modality probes, they incubated the $CuInS_2$/ZnS:Mn with human pancreatic cancer cells (BXPC-3 cells line). The red emission observed in confocal microscopy indicated that BXPC-3 cells internalized these QDs. In cells lysates it was possible to observe that the internalized QDs produced MRI contrast enhancement in a T_1-weighted image.

Manganese doped zinc selenide (ZnSe:Mn) QDs for dual-modal imaging were prepared by Sharma et al. [176], in organic medium and varying Mn^{2+} concentration. These nanoparticles had an average size of 6.5 nm (observed by TEM) and ICP confirmed they had incorporated 1.1 to 5.9% of Mn^{2+}. As others before, these authors also observed that by increasing Mn^{2+} concentration, the emission intensity first increases (these QDs reached a maximum at Mn^{2+}concentration of 3.2%), starting to decrease after. However, the emission peak position stayed at 585 nm independent of the dopant concentration. The QY for these QDs, in water, was determined to be 18%, after a ligand exchange, using the MPA as functionalizing/stabilizing agents. The potential application of the ZnSe:Mn for MRI was investigated, and these nanoparticles presented a relaxivity value of 2.95 $mM^{-1}s^{-1}$ (at 3 T and 25 °C).

Zhang et al. [177] prepared Mn^{2+} doped CdTe QDs in aqueous solution, obtaining QDs with a size of around 3.7 nm (estimated by TEM) and a Mn^{2+} level of 2.8% (by atomic absorption spectroscopy). Fluorescence studies, in water, showed that the QY of CdTe:Mn (48%) increases when compared to CdTe (23%), and decreases with further increase of Mn^{2+} concentration. The emission wavelength can be tuned with the Mn^{2+} amount, and the doped QDs emission peak was red-shifted, relatively to non-doped QDs, emitting at 545 nm. The longitudinal relaxivity of these CdTe:Mn value was 4.29 $mM^{-1}s^{-1}$ (measured at 7 T and room temperature).

Although several groups reported the potential of manganese-doped QDs for optical and MR imaging, only Ding et al. [178] presented experiments of fluorescence and MR imaging *in vivo* for passive tumor targeting. They prepared $CuInS_2$/ZnS:Mn nanoparticles with a diameter of 3.6 nm (determined by TEM) and emissions around 620 nm. The QDs containing a Mn^{2+} concentration of 1.4% (by ICP-OES), presented the higher QY, and a relaxivity of 5.84 $Mm^{-1}s^{-1}$ (at 1.5 T and 37 °C). For the *in vivo* studies, first the cytotoxicity of PEGylated QDs on the proliferation of HeLa cells was evaluated, and it was observed that these QDs presented no toxicity for the concentration below of 9 mM. Nude mice, subcutaneously transplanted with human colon cancer (LS180) tumor cells at the leg, was injected intravenously with the PEGylated $CuInS_2$/ZnS:Mn. By optical images, it was observed that the fluorescence signal appears 10 min after the injection and reaches its maximum around 6 h post-injection. For the MRI studies, the nude mice were implanted with a tumor and injected intravenously with the same dosage level of nanoparticles. T_1-weighted MR images showed that the contrast reaches its maximum at 8 h post-injection, companying the decrease of the T_1 value. The biodistribution of the QD-injected studies showed that the strongest fluorescent signal was found in the liver, followed by stomach, kidney, tumor, and spleen. But in the heart and lungs no optical signal was observed.

3.2.2. Gadolinium-Doped QDs

The first example of gadolinium-doped QDs as multimodal agents for optical and MR images was reported by Li and Yeh [179]. These authors prepared CdSe:Gd capped with TOPO, with a diameter of 6.3 nm (estimated from TEM) and a dopant level of 0.061% (from ICP). These QDs have an emission maximum at 600 nm, and it was observed that by increasing the dopant amount, a decrease in the QY was observed. Exchanging the stabilizer from TOPO to the water-soluble MPA stabilizing agents leads to a decrease in

the QY from 4.6 to 0.2% (relative to rhodamine). The longitudinal and transverse relaxivities were measured at 3 T, and these CdSe:Gd presented a $r_1 = 76.7\ mM^{-1}s^{-1}$ and a $r_2 = 54.3\ mM^{-1}s^{-1}$. Since the r_2/r_1 value was 0.7 (close to 1) these QDs could act as a positive contrast agents, for T_1-weighted images.

Liu et al. [96] prepared zinc oxide (ZnO) QDs doped with Gd^{3+} in ethanol, with a Gd/Zn rate of 8% (determined by inductively coupled plasma mass spectrometry, ICP-MS). The ZnO:Gd presented a size of 4 nm (estimated by TEM) and an emission maximum around 550 nm. The incorporation of Gd^{3+} (8%) increased the fluorescence QY (from 13.5 to 34%, in ethanol relatively to rhodamine), but further incorporation of Gd^{3+} led to a decrease in the QY. A surface modification using *N*-(2-aminoethyl)aminopropyltrimethoxysilane (AEAPS) was performed in order to disperse the QDs in aqueous medium and to use them in biological systems. The ZnO:Gd cytotoxicity was studied in HeLa cells showed a low toxicity, with 1 mM of QDs during 24 h. The longitudinal relaxivity was determined at 1.5 T showing a value of $r_1 = 16\ mM^{-1}s^{-1}$. The ZnO:Gd were incubated with HeLa cells and a yellow emission, due to the presence of QDs, was observed in confocal microscopy. Cell pellets of HeLa cells with and without QDs were used in T_1-weighted MR imaging, proving that the cells treated with QDs showed brighter images than the others.

Quaternary QDs of zinc copper indium sulfide (ZnCuInS) were doped with Gd^{3+} and capped with ZnS by Guo et al. [180]. These authors prepared ZnCuInS:Gd with an amount of Gd^{3+} from 7.9 to 14.3% (determined by ICP-MS), and passivated them with a shell of ZnS in order to enhance their fluorescence. These ZnCuInS:Gd/ZnS presented a size around 4.3 nm (determined by TEM) and an emission centered between 550 nm to 725 nm depending on the Zn/Cu ratio, with increasing the amount of Zn a blue-shift was observed. Also a slight decrease in QY was observed with the incorporation of Gd^{3+}. For biological applications, the doped QDs were coated with bovine serum albumin (BSA), forming nanohybrids with a hydrodynamic diameter around 70 nm. Relaxivity studies of ZnCuInS:Gd/ZnS@BSA showed that these systems presented stronger T_1 effect, with r_1 values of 11.53, 13.65, and 15.78 $mM^{-1}s^{-1}$ (7 T) for the systems with 7.9, 10.6, and 14.3% of Gd^{3+}, correspondingly.

For the *in vitro* studies, the ZnCuInS:Gd/ZnS were incubated with HeLa cells, a fluorescence signal was observed inside the cells except for the nucleus region, and the MR signal was enhanced in the cells containing these systems for 6 h, showing that these QDs were uptaken by the cells. The toxicity studies of ZnCuInS:Gd/ZnS@BSA in HeLa cells showed no apparent loss of the cell viability, after incubation with QDs with a concentration of 500 $\mu g\ mL^{-1}$ for 24 h. The ZnCuInS:Gd/ZnS@BSA nanohybrids were also used in *in vivo* imaging, injecting them intravenously into BALB/c mice at a dosage of 0.05 mmol Gd/kg. By fluorescence imaging it was observed that these systems accumulated in the liver 30 min after injection, and using a MRI scanner (7 T) an enhancement in T_1-weighted MR images was observed 1 h post-injection. At 6 h after injection, the mice were sacrificed and it was observed that the majority of the nanohybrids remained in the liver and the spleen. No fluorescence in the kidneys was observed, which can mean that particles with this size do not undergo renal clearance. To evaluate the toxicity of these nanohybrids in major organs (such as heart, liver, spleen, lungs, and kidneys), H&E (hematoxylin and eosin) staining examination was performed. The organs were collected at 2 and 14 days after the injection, and the results revealed no organ abnormality or lesions in mice administrated with ZnCuInS:Gd/ZnS@BSA, indicating a good biocompatibility of these systems [180].

Zhang et al. [181] prepared CdTe:Gd in aqueous suspension with an amount of 2.03% (determined by ICP) of dopant and a size around 3 nm (determined by TEM). These QDs have a maximum emission peak in 640 nm with a QY of 38% in water (relatively to rhodamine), which decreases when the amount of Gd^{3+} increases. Paramagnetic studies demonstrated a longitudinal relaxation rate (r_1) value of 3.27 $mM^{-1}s^{-1}$ (3 T). For targeting cancer cells, the CdTe:Gd QDs were conjugated with folic acid (FA) using the EDC/NHS coupling strategy. For the *in vitro* studies, the conjugates were incubated with HepG2 cells (human liver cancer cells) and a red fluorescence was observed, showing that the CdTe:Gd-FA successfully labeled the cells, compared to CdTe-Gd that could not label the cells. Using MTT (methyl thiazolyl tetrazolium) assay, the cytotoxicity of CdTe:Gd-FA in HepG2 cells was evaluated, showing that, after 24 h, more than 80% of the cells remained viable with a conjugate concentration of 0.5 $mg \cdot mL^{-1}$. For the *in vivo* studies, BALB/c nude mice were injected with HepG2 cells into their right axillar, and then CdTe:Gd-FA were injected in their eye veins. Fluorescence and MR images were recorded, and an enhancement in the fluorescence and the MR signals were observed in the tumor site.

Gd-doped CuInS caped with ZnS (Gd:CuInS/ZnS) were prepared by Yang et al. [182] as bimodal QDs. These particles presented a size around 3.0 nm (determined by TEM), a 3.05% Gd:CuInS (calculated by EDS) and an emission maximum around 670 nm. For the magnetic properties studies and further applications, the hydrophobic QDs obtained were encapsulated with the PEG and transferred to aqueous phase. Gd:CuInS/ZnS@PEG bimodal systems presented a r_1 value of 9.41 s^{-1} per mM of Gd^{3+} (at 1.5 T), suggesting that these particles can be used as T_1 contrast agents. MTT studies with U87MG cells (glioblastoma astrocytoma) showed that Gd:CuInS/ZnS@PEG presented low cytotoxicity against these cells. *In vivo* studies were performed to detect U87-expression in tumors by fluorescence imaging, and the fluorescence signal due to the presence of these bimodal nanoparticles were detected in tumor and liver 4 h post-injection (Fig. 12(A)). T_1-weighted MR images were obtained, after injecting a dosage of 0.05 mmol Gd/Kg body weight of nude mice, which showed a enhancement in the MRI signal in the tumor site 4 h post-injection (Fig. 12(B)). H&E staining study of several major organs, allowed the study of the *in vivo* toxicity of the Gd:CuInS/ZnS@PEG nanoparticles, and no necrosis and inflammation in the tissue of several organs was observed 7 days after injection.

3.2.3. Iron-Doped QDs

As far as we know, up to the present moment in the literature exists only one report of iron-doped QDs for optical and MR imaging that presents its emission and relaxivity

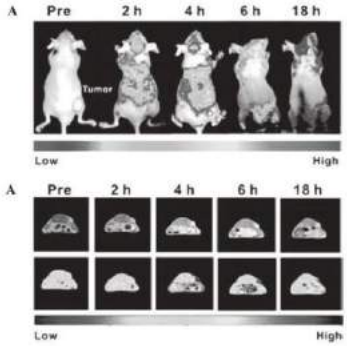

Figure 12. *In vivo* (A) fluorescence images and (B) T_1-weighted MRI of mice bearing U87 tumor cells. Adapted with permission from [182], W. Yang, et al., *ACS Appl. Mater. Interfaces* 7, 18759 (2015). © 2015, American Chemical Society.

properties for these QDs. Saha and collaborators [183] prepared CdTe:Fe QDs for magnetic and vis-NIR imaging. These QDs have been synthesized by an aqueous hydrothermal technique, using Teflon®-lined autoclaves. This methodology allows the utilization of high temperatures in aqueous media, which accelerates the nanocrystal growth rate. The CdTe:Fe presented an emission between 530 and 738 nm, depending on the reaction time. The nanocrystals were obtained with a diameter around 4.9 nm (determined by TEM) and 5.6% of iron (determined by ICP) in their composition. As have been seen for other dopants (such as Mn^{2+} and Gd^{3+}), an increase in dopant concentration leads to a decrease in fluorescence intensity. By X-ray photoelectron spectroscopy (XPS), these authors verified that the major quantity of Fe^{2+} was found in the core, decreasing toward the border. The transverse relaxivity (r_2) for CdTe:Fe was determined to be 3.6 $mM^{-1}s^{-1}$ (in 4.7 T at room temperature). As a proof of concept, these QDs were incubated with murine macrophages cell line (J774) cells, in water for 6 h with a concentration of 0.37 mM of Fe^{2+}, and the results showed optical images with high emission intensity and T_2-weighted MR images. This demonstrated that these QDs had the capability to produce both optical and MR images.

3.2.4. Final Considerations About Doped QDs

Doped quantum dots have attracted much attention, but the control of the doping efficiency is still a challenge. Doping efficiency depends of various aspects such as the size difference between the host and the dopant cations, and the precursor source (which can control the ligand-metal bond strength) [151]. Although some advantages have also been linked to the use of doped QDs [181]:

- Integration of two capabilities in a single nanoparticle, such as bimodal imaging agent.
- Smaller size, when compared with other dual-modal imaging agents, such as QDs-iron oxide or paramagnetic coating of Gd^{3+} chelates.
- The loss in the fluorescence properties can be avoided; it depends on the dopant amount.
- These nanoparticles can be prepared in a one-pot strategy, reducing the cost, the reaction steps and the waste of reagents.

From the presented examples, we can notice that the incorporation of certain ions (such as manganese, gadolinium, and iron) in QDs is a possible methodology to produce bimodal nanoparticles for optical and MR imaging (Table 2). Although, it seems consensual that the main drawback for these systems is that the introduction of a high quantity of dopant in the nanocrystal (without changing the nanoparticle crystalline lattice) is not easy, and it leads to fluorescence quenching. Consequently, the improvement of MRI properties will cause the degradation of the optical properties. Thus, other methods for the incorporation of paramagnetic ions in QDs, which will not modify their emission efficiency and produce small nanostructures, are still desirable.

3.3. Quantum Dots Associated with Gd^{3+} Chelates

As has been previously mentioned, among the CAs, paramagnetic chelates containing Gd^{3+} ions are widely used. Gadolinium has physical properties that make it a good candidate to be used as CA. It possesses seven unpaired electrons (highest spin density) and relatively long electronic relaxation times, reducing the longitudinal (T_1) proton relaxation times [184, 185]. Gd^{3+} cannot be used freely in human body, since at physiological pH it suffer hydrolysis and produces insoluble $Gd(OH)_3$, which accumulates in the bones and liver. Thus, it has been a great interest in the development of highly stable Gd^{3+} complexes, to be used as CA for MRI [21, 186]. Gd^{3+} chelates must present several properties, such as water solubility, chemical stability, high aqueous relaxivity, and low toxicity *in vivo* and be relatively rapidly cleared from the circulation after their application for diagnosis procedure [73, 94, 187]. From the beginning of the 1980s, the majority of CAs used clinically in MRI have chelates Gd^{3+} as their active component, since CAs based on chelates ensures great security for human use, less toxicity than the free gadolinium ions, and different biodistribution [188].

Gd^{3+} complex-based MRI CAs are mainly classified into two groups: linear and macrocyclic chelates, the latter being more stable than the linear ones (Fig. 13). Currently, among the macrocyclic CAs gadolinium-based for MRI most used clinically are Dotarem® [gadoterate, Gd-DOTA (tetraazacyclododecane tetraacetic acid)], Prohance® [gadoteridol, Gd(HP-DO3A)], and Gadovist® (Gd-BT-DO3A). And those with linear structure are: Magnevist® (gadopentetate dimeglumine, Gd-DTPA (diethylene triamine pentaacetic acid), Omniscan® (gadodiamide, Gd(DTPA-BMA)), Opti-MARK (Gd-DTPA-BMEA), Multihance® (Gd-BOPTA), and Eovist® or Primovist® [Gd(EOB-DTPA)] [189]. These CAs affect specially the longitudinal relaxation time (T_1), providing bright contrast, which facilitates diagnosis of diseases, besides being well tolerated when administered in patients [190].

In order to increase the relaxivity, paramagnetic chelates have been bounded to larger structures, such as

Table 2. Dopant amount (%), size (nm), emission wavelength (nm), relaxivity ($mM^{-1}s^{-1}$) of the doped QDs discussed in this chapter.

Dopant	QD	Dopant amount (%)	Size (nm)	λ_{em} (nm)	r_1 ($mM^{-1}s^{-1}$)[a]	Ref.
Mn^{2+}	CdSe/ZnS	6.2	4.7	650	18[b]	[172]
	ZnS	10	1.5	466, 507(sh)[c]	20[d]	[173]
	CdTe/ZnS	4.7–9.7	4.3	650	10.7–5.4[d]	[174]
	$CuInS_2$/ZnS	2.3	4.0	600	7.2[d]	[175]
	CdTe	2.8	3.7	545	4.29[b]	[177]
	$CuInS_2$/ZnS	1.4	3.6	620	5.84[e,f]	[178]
Gd^{3+}	CdSe	0.061	6.3	600	76.7[d]	[179]
	ZnO	8	4	550	16[c]	[96]
	ZnCuInS/ ZnS@BSA	7.9–14.3	70	700	11.53–15.78[b]	[180]
	CdTe	2.03	3	640	3.27[d]	[181]
	CuInS/ZnS @PEG	3.05	3	670	9.41[e]	[182]
Fe^{2+}	CdTe	5.6	4.9	530–738	$r_2 = 3.6$[g]	[183]

Notes: [a] room temperature, [b] 7 T, [c] shoulder, [d] 3 T, [e] 1.5 T, [f] 37 °C and [g] 4.7 T.

biomolecules [191] and gold nanoparticles [92, 192] and have also been used to coating silica and lipid-nanostructures (nanospheres, micelles, and liposomes) [193].

A recent study by Zhou and Lu [194] showed that the relaxivity of encapsulated Gd^{3+} chelates is lower than that of the corresponding small molecular complex, due to a permeability barrier imposed by the vesicle membrane, making difficult the exchange between bulk water and the water complexed to encaged Gd^{3+}. However, if the chelates are linked to the nanostructures' surface, it can increase their relaxivity, since bulk water could easily access the Gd^{3+} chelates. Moreover, a nanocarrier containing both core-encapsulated and surface-conjugated Gd^{3+} chelates presents a better relaxivity [195]. This fact is due to a higher Gd^{3+} concentration per unit of liposomal particle. Most contrast agents based on Gd^{3+} chelates act by increasing the longitudinal relaxivity r_1, but can also provide enhancement in transverse relaxivity r_2 [196].

As previously mentioned in the QDs section, they have a chemically active surface that can be easily modified and that makes it possible to conjugate them with a variety of organic and inorganic particles, such as, peptides, antibodies, DNA, drugs, and magnetic materials, as well as to make them water-dispersed and biocompatible in biological fluids [14]. The main motivation for the preparation of QDs-Gd^{3+} chelates is that with this combination it will be possible to produce nanoparticles with a high concentration of Gd^{3+} ions, which can increase the relaxivity per particle and decrease the dosage needed for MRI contrast [21, 197]. Thus, several approaches to develop bimodal nanoparticles for optical and MR imaging involving the association of Gd^{3+} chelates to QDs have been reported [198–202]. In this

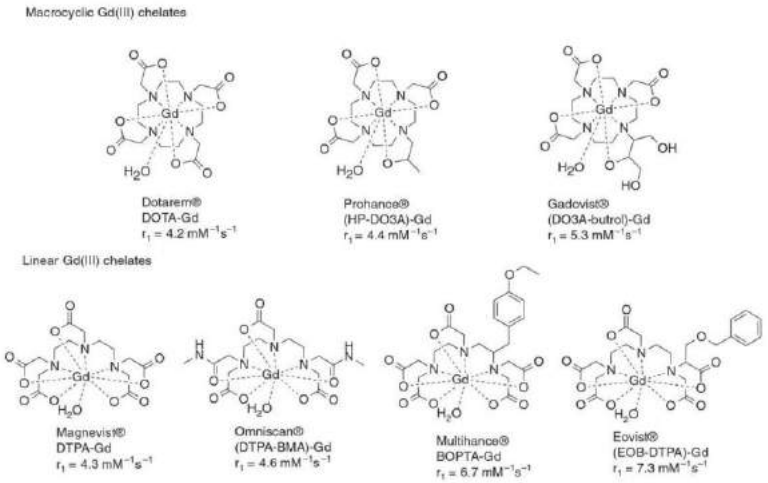

Figure 13. Chemical structure of the principals ACs based- gadolinium paramagnetic with its relaxivity values at 1.5 T189.

section, we divided them in three categories: coating QDs with molecules containing Gd^{3+} chelates, encapsulation of free QDs together with chelates in nanostructures, and direct conjugation of the chelates with the QDs' surface.

3.3.1. Coating of Quantum Dots with Molecules Containing Gd^{3+} Chelates

Lipids and other amphiphilic compounds have been used as building blocks for the preparation of bimodal nanoparticles for optical images and MRI. These amphiphilic structures possess both hydrophobic and hydrophilic sites and the unfavorable contact between the non-polar part and the water leads to a self-organization in aggregates. When in the presence of hydrophobic QDs, the hydrophobic chain of the amphiphiles can interact with QDs' stabilization agents, coating QDs one by one as represented in Figure 14 [193].

Lipid-based particles can carry several Gd^{3+} chelates exhibiting a higher relaxivity per particle [199]. An example of this approach is the work of Mulder et al. [198]. They synthesized CdSe/ZnS core/shell QDs, emitting fluorescence around 560 nm in chloroform. In order to make these QDs water-dispersed and biocompatible, they were coated with a mixture of PEGylated [PEG-DSPE: 1,2-Distearoyl-*sn*-glycero-3-phosphoethanolamine-*N*-(methoxy(polyethyleneglycol))-2000] and paramagnetic [Gd-DTPA-BSA:Gd-DTPA-bis(stearylamide)] lipids (p-QDs). These authors suggested that a lipid monolayer coating the QD could be obtained using a huge amount of PEGylated lipids in the formulation. This bimodal nanoprobe presented a high r_1 of 12 $mM^{-1}s^{-1}$ per ions (at 1.41 T), which is higher than for the Gd-DTPA alone, and 2000 $mM^{-1}s^{-1}$ per QDs (also at 1.41 T). These p-QDs were conjugated covalently with the cyclic peptide RGD (arginine-glycine-aspartic acid), via a maleimide-functionalized PEGylated lipid (PEG-DSPE-Mal), in order to prepare a specific probe for angiogenic blood vessels. The p-QDs-RGD was incubated with human umbilical vein endothelial cells (HUVECs) for *in vitro* assays. Fluorescence microscopy images showed that the p-QDs-RGD were internalized by the cells and accumulated at a perinuclear location. Cells incubated with p-QDs also presented a minor fluorescence signal, indicating that a non-specific cellular internalization also occurred. Cell pellet of the cells incubated with p-QDs-RGD presented a brighter T_1-weighted image than the ones incubated with p-QDs. The results suggested that these systems could be attractive contrast agents to early screening and for following the effect of anti-angiogenesis therapy.

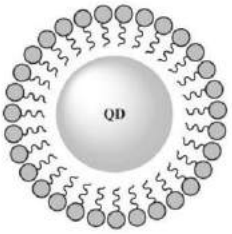

Figure 14. Schematic representation of a QD coated by lipids.

In other work the same group [203] used the p-QDs-RGD intravenously injected for further *in vivo* studies of ongoing tumor angiogenesis in mice. This single molecular imaging contrast agent (p-QDs-RGD) allowed parallel detection by both optical [intravital microscopy (IVM) and optical imaging] and magnetic (MRI) techniques. The IVM allowed the detection of microvessels in tumor-bearing mice at cellular resolution and the observation of their typical tortuous morphology (Fig. 15). By fluorescence microscopy, 5 to 10 min post-injection, the authors also observed endothelial cells labeled by bimodal nanoparticle in the tumor blood vessels (Fig. 15). None fluorescence emission was found in the blood vessels from distant normal tissues. MRI *in vivo* was also performed providing an anatomical resolution of the entire tumor and the p-QDs-RGD was also injected in real time inside the MR image scanner, to be able to compare the pre- and post-injection images. MRI, taken 45 min after the injection, showed an enhancement in T_1-weighted images, observed in the tumor periphery (the regions where the angiogenic activity was higher (Fig. 15). Biodistribution studies showed that the p-QDs-RGDs accumulated in the liver and spleen.

In other work, the Mulder's group published a paper about the application of recombinant human annexin A5 conjugated to bimodal nanoparticles in apoptotic cells using a similar p-QDs coated by paramagnetic lipids [205]. The maleimide group of Mal-PEG-DSPE, present in the p-QDs' coating, was covalently conjugated to the cysteine of the recombinant human annexin-A5. The ionic relaxivities of this nanomicelles were equivalent to those found in p-QDs-RGDs [198], being 12.4 (r_1) and 18.0 $mM^{-1}s^{-1}$ (r_2), whereas the relaxivity per particles was at least 150 times higher than ionic relaxivity. They demonstrated the specificity of annexin A5-p-QDs to detect apoptotic events *in vitro* by fluorescence microscopy and MRI in Jurkat cells (T-lymphoma cell line).

The annexin A5 is a molecular bioprobe to target the phosphatidylserine (PS) exposed on the cell surface, which is an amino-phospholipid present in the membrane of apoptotic cells, triggering phagocytosis. For this, PS has been

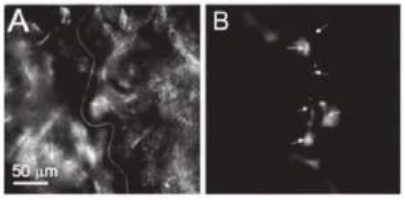

Figure 15. Images of tumor blood vessels were specifically labeled by RGD-labeled paramagnetic quantum dots (p-QDs-RGD) using parallel detection of IVM (A) and fluorescence microscopy (B). (A) Bright field image showing typical tortuous morphology of the angiogenic blood vessels (indicated by the yellow lines). (B) Fluorescence image showing endothelial cells labeled by contrast agent (p-QDs-RGD) (indicated by yellow arrows). Adapted with permission from [204], W. J. Mulder, et al., *Angiogenesis* 12, 17 (2009). © 2009, Springer.

considered one of the most explored targets of programmed cell death (PCD) [206].

To study PCD in apoptotic cells with the annexin A5, Jurkat cells were incubated with anti-Fas (CD95 human monoclonal antibody) for 15 min to induce an increase of apoptotic events. When apoptotic cells were incubated with A5-p-QDs, a high brightness image was observed by fluorescent microscopy. On the other hand, when the cells were not stimulated with anti-Fas, less bright images were observed. In relation to T_1-weighted images, a strong signal of the apoptotic cells incubated with A5-p-QDs was revealed. However, cells that were not treated with anti-Fas also presented some signal, because they undergo naturally apoptosis even in the culture without stimuli, in about 5% to 10% of the cells [205]. Therefore, in other studies involving annexin A5 with radioactive compounds, a tumor decrease was observed due to the increase of the cellular uptake after radiotherapy, indicating therapy efficiency caused by radiation-induced apoptosis [207]. Thus, fluorescence and MRI images with annexin A5 can allow the evaluation of the cancer development and treatment by detecting apoptosis using A5-p-QDs. According to these authors, the A5-p-QDs nanoparticles can be applied for acquiring *in vivo* and *in vitro* apoptosis images, being bimodal nanoparticles with potential use in MRI and intravital microscopy [205].

A different approach, using silica as the capping agent, was reported by Yang et al. [208]. These authors synthesized core/shell QDs of cadmium sulfide: manganese/zinc sulfide (CdS:Mn/ZnS) by a reverse-micelle method and to make them water-dispersed and biocompatible, coated then with a silica layer, by injecting the following components in the QDs micellar solution: tetraethyl orthosilicate (TEOS), 3-(aminopropyl)-triethoxysilane (APTES), and 3-(trihydroxysilyl)-propylmethylphosphonate (THPMP). The CdS:Mn/ZnS/Si were associated with a paramagnetic chelate using a silane-coupling agent [*N*-(trimethoxysilylpropyl)-ethylenediamine triacetic acid trisodium salt, TSPETE], acting also as a chelating agent for Gd^{3+}. TEM images of the final systems showed the presence of nanoparticles with a diameter of about 7 to 10 nm, containing an electron-dense core of 3 nm. Their emission spectrum presented a maximum at 590 nm, corresponding to the yellow emission of Mn^{2+}. XPS was used to confirm the presence of Gd^{3+} in the nanoparticle surface, and the number of Gd^{3+} ions per particle was determined by ICP, which provided a value of around 107 Gd^{3+} ions per particle. Relaxometric studies at 4.7 T provided a longitudinal relaxivity (r_1) of 20.5 $mM^{-1}s^{-1}$ and a transverse relaxivity (r_2) of 151 $mM^{-1}s^{-1}$, which indicate that these particles may be used as both T_1 and T_2 contrast agents.

Koole et al. [199] prepared bimodal agents by coating QDs with silica and an additional lipid dense monolayer. QDs of CdSe/CdS/ZnS were prepared with a diameter of 7.7 nm (determined by TEM). These QDs were incorporated in silica particles using TEOS, rendering particles of 31 nm. In a next step, the silica capping QDs (QD-Si) were coated with octadecanol to make them hydrophobic, after which they were covered with PEGylated, maleimide-PEGylated, and paramagnetic lipids (containing Gd-DTPA), using the same approach described in their previous work [198]. The average size for these particles (QD-Si-pLip) was 58 nm determined by dynamic light scattering (DLS). From photophysical studies, it was observed that the successive coatings did not affect the absorption and emission spectra, and the nanoparticles' emission maximum remained at 630 nm. Longitudinal relaxivity (r_1) of the QD-Si-pLip was determined as 14.4 $mM^{-1}s^{-1}$ (at 6.3 T) and by ICP it was found that each nanoparticle contains 2500 Gd^{3+} ions. As a proof of concept, tests *in vitro* were performed with serum-activated of human umbilical vein endothelial cells (HUVEC). Using the same methodology as before [198], the RGD peptide was conjugated with the nanoparticle, and the QD-Si-pLip-RGD obtained was incubated with the cells for 7 h at 37 °C. By fluorescence microscopy it was observed that HUVEC cells were specifically labeled by QD-Si-pLip-RGDs. The nanoparticles were internalized, and they also accumulated in a perinuclear location of these cells. T_1-weighted images of cells pellets showed an enhancement in signal intensity coming from the cells incubated with QD-Si-pLip-RGDs when compared with the ones incubated with QD-Si-pLips, confirming the specific uptake by HUVEC cells.

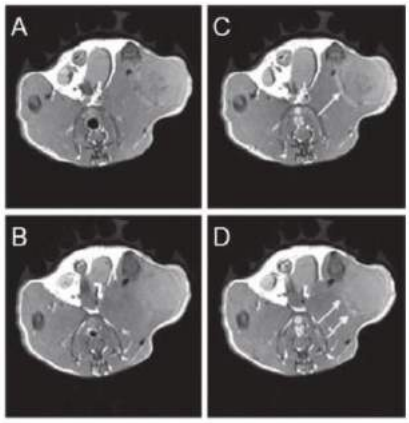

Figure 16. Images by MRI of two slices from the tumor of the mice that was infused with p-QDs-RGD. [A, B] T_1-weighted images before the injection of the contrast agent and [C, D] after the injection, where it was observed bright regions in the peripheral part of the tumor (indicated by yellow arrows). Adapted with permission from [204], W. J. Mulder, et al., *Angiogenesis* 12, 17 (2009). © 2009, Springer.

Ternary semiconductors QDs of $CuInS_2$ coated with ZnS were prepared by an organometallic synthesis [209]. In order to make these QDs water-dispersed, they were capped with an amphiphilic polymer PMO [poly(maleic anhydride-alt-1-octadecene)] by self-assembly of the polymer around the QDs. In water, the maleic anhydride residues presented in the PMO were hydrolyzed forming two carboxylate groups. This way, the capping step makes the QDs hydrophilic and allows further conjugations with the reactive carboxylic groups. These QDs-PMO-COOH particles were reacted

with ethylenediamine, using a standard EDC/NHS procedure, to introduce amine groups in the surface, giving QDs-PMO-NH_2. Gd-DTPA was conjugated with QDs-PMO-NH_2 using the EDC/NHS methodology, associating optical and paramagnetic properties in the same nanoparticle (QD-PMO-Gd). Finally, these authors conjugated a target ligand to the nanoparticle, the folic acid (FA), creating the complex system QD-PMO-Gd-FA. The fluorescence studies showed that the successive coatings and conjugations did not affect significantly the emission, which presented a maximum at 574 nm for QDs-PMO-Gd-FA. Longitudinal relaxation times were measured for these particles, and it obtained a $r_1 = 3.72\ mM^{-1}s^{-1}$ at 7 T. Results from MTT assays with HeLa, MCF-7 (breast cancer of Michigan Cancer Foundation-7) and HepG2 cells, showed no significant cytotoxicity. Incubation of QD-PMO-Gd-FA with HeLa, for 1 h, originated a red fluorescence inside the cells, in the cytoplasm region, which were observed by confocal microscopy. For MCF-7 and HepG2 cells, after incubation in the same conditions, only images with punctuated fluorescence were observed. The authors attributed these results to the fact that both MCF-7 and HepG2 cells present few folate receptors on their membrane, thus they cannot internalize high amounts of QD-PMO-Gd-FA, while HeLa cells possess many folate receptors.

3.3.2. Encapsulation of QDs and Gd^{3+} Chelates

Another approach used to associate Gd^{3+} chelates and QDs is the encapsulation of these two components in polymers or liposomes. In this type of methodology, the QDs are free inside polymeric/lipidic micelles, and the chelates can be inside or on the surface of the nanocomposite. Just one particle can have multiple QDs and Gd^{3+} chelates (Fig. 17) [200, 210].

Tan and Zhang [210] encapsulated QDs and the Gd^{3+} chelate Gd-DTPA in the biopolymer chitosan to produce fluorescent and paramagnetic labels. To prepare this system, the negatively charged CdSe/ZnS QDs (stabilized with 3-mercaptopropionic acid) and Gd-DTPA were dispersed in an acidic solution containing chitosan. Chitosan is a polymer that possesses amino groups, which will be protonated in an acid medium, being positively charged. Thus, it can interact electrostatically with the QDs and the chelates, encapsulating them. These systems presented a size of around 50 nm (determined by TEM and DLS), and it was found that the chitosan-encapsulated system contain 34% of QD and 6% of Gd-DTPA, in mass. The encapsulation of the QDs does not change their fluorescence properties; the emission maximum remained around 565 nm. The relaxometric studies showed that the chitosan bimodal nanobeads presented smaller longitudinal relaxation ($r_1 \approx 33\ mM^{-1}s^{-1}$, 7 T) than the Gd-DTPA chelates ($r_1 \approx 38\ mM^{-1}s^{-1}$, 7 T), although these authors stated that the difference is not statistically significant.

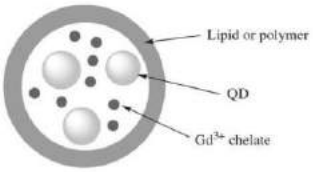

Figure 17. Schematic representation of QDs and Gd^{3+} chelates encapsulated inside polymeric/lipidic micelles.

Liu et al. [200] encapsulated QDs in polymers, followed by their conjugation with a Gd-DOTA derivative. Hydrophobic CdTe/ZnS QDs were encapsulated into two polymers, in the amine-terminated m-PEG-phospholipid and in the amine-modified Pluronic F127. The average sizes obtained by TEM were 10.8 nm for PEG-QD and 22.1 nm for F127-QD. The optical studies showed a red shift, about 20–40 nm, in the emission spectra for the encapsulated QDs, when compared with non-encapsulated ones. In order to obtain nanoprobes that could be used also in MRI, they conjugated the encapsulated systems with the chelating agent DOTA, followed by addition of $GdCl_3$. The relaxivity measurement provided a value of $r_1 = 4.38$ and $8.17\ mM^{-1}s^{-1}$ (4.7 T), for PEG-QD-Gd and F127-QD-Gd, respectively. These authors also performed *in vitro* studies, incubating the PEG-QD-Gd and F127-QD-Gd with macrophage cells for 2 h. By confocal microscopy it was possible to observe the accumulation of the nanoparticles inside the cells without apparent damage to the cells. Cell viability studies were done, and the results suggested that the cells treated with PEG-QD-Gd presented lower cell viability that the ones treated with F127-QD-Gd.

3.3.3. Direct Conjugation of Quantum Dots to Gd^{3+} Chelates

Bimodal imaging probes by covalent attachment of a Gd^{3+} chelate to the QDs' surface was used by Stasiuk et al. [211]. They linked covalently Gd^{3+} chelates to indium phosphide/zinc sulfide (InP/ZnS) QDs' surface by a stabilizer exchange (Fig. 18). The Gd^{3+} chelate was prepared by reacting a 1,4,7-triazacyclononane derivative (TACN) and lipoic acid. By magnetic susceptibility measurements and UV-visible spectroscopy, these authors confirmed the attachment of around 80 Gd^{3+} complexes. The attachment of the chelates to QDs increased nanoparticles hydrodynamic diameter from 6.9 to 8.6 nm, measured by DLS. The photophysical studies showed that the linkage of the Gd^{3+} complexes to the QDs did not affect their luminescence,

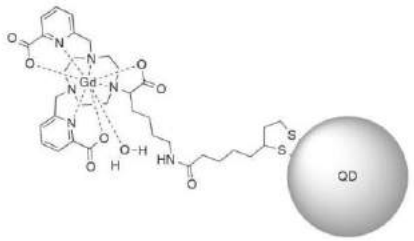

Figure 18. Schematic structure of the bimodal system prepared by Stasiuk et al. Adapted with permission from [212]. G. J. Stasiuk, et al., *ACS Nano.* 5, 8193 (2011). © 2011, ACS Publications.

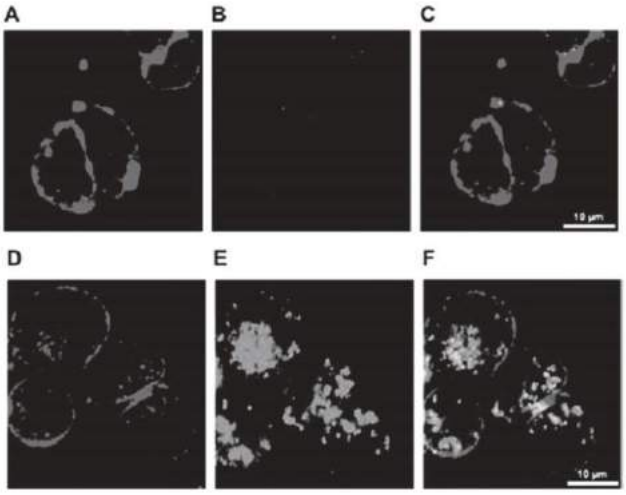

Figure 19. Optical images of CHO cells. The cell were incubated with (A, D) concanavalin A rhodamine (in red); (B) Gd-QDs (in green); (E) QDs-Gd-MCa (in green). In C: merged image of A and B. In F: merged image of D and E. [Adapted with permission from [211], G. J. Stasiuk, et al., *ACS Nano* 5, 8193 (2011). © 2011, American Chemical Society.

maintaining their emission peak around 620 nm, although with a slight decrease in the QY, from 8.5 to 6.1% in water. Relaxivity measurements gave values of $r_1 = 13\ mM^{-1}s^{-1}$ per Gd^{3+} ion (0.81 T, 25 °C) and 900 $mM^{-1}s^{-1}$ per bimodal particle (0.81 T, 25 °C).

For monitoring biological events the nanoparticles needed to be internalized by cells. For this reason, these authors conjugated a cell penetrating peptide (maurocalcine, MCa) and the Gd^{3+} chelates to the QDs, obtaining a probe with 30–40 Gd^{3+} complexes (QDs-Gd-MCa) [211]. The final systems were incubated with Chinese hamster ovarian cells (CHO cell) during 2 h, which were evaluated by confocal microscopy (Fig. 19). The appearance of punctuate dots inside cells incubated with the QDs-Gd-MCa was observed, suggesting that these systems were trapped in endosomes showing that they were uptaken by cells through an endocytosis-mediated mechanism. To delimitate the cells, they authors stained the cell plasma membrane with rhodamine-conjugated concanavalin A. MRI studies showed that QDs-Gd-MCa (injected in rats) led to a distinct signal, 15 min after injection. And when compared with Dotarem®, this dual-probe had an higher tissue retention time; the signal intensity was still measurable after 4 h (Fig. 20) [211].

Theoretically, restrictions of internal rotations of the complex (bond to QDs) will accelerate the water exchange of the water coordinated to Gd^{3+} and the surrounding bulk water molecules, increasing the relaxivity value. Thus, in order to optimize the relaxivity of Gd^{3+} chelates linked to InP/ZnS, these same authors prepared three ligands with different linkers (Fig. 21) [212]. They used linkers with different flexibility: lipoic acid (L1), which has a dithiol promoting a strong bond with the QDs' surface; mercaptopropionic acid (L2), which probably will reduce the mobility of the complex due to its shorter aliphatic chain; and mercaptobenzoic acid (L3), which has a rigid π-conjugated system that could reduce the internal rotation of the complex. The

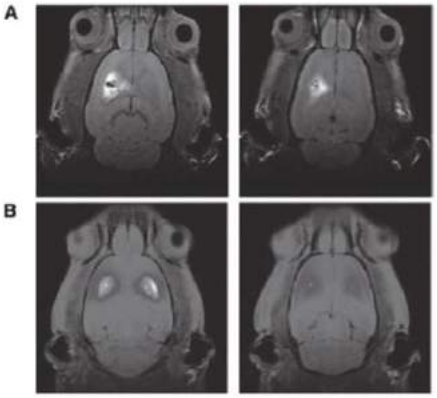

Figure 20. T_1-weighted MRI images of rat brain incubated with (A) QDs-Gd-MCa and (B) with Dotarem®, after 15 min (left) and after 4 h (right). The images were obtained at 7 T. Adapted with permission from [211], G. J. Stasiuk, et al., *ACS Nano.* 5, 8193 (2011). © 2011, American Chemical Society.

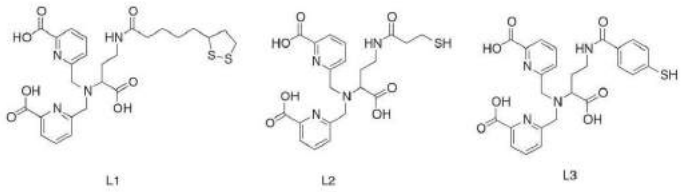

Figure 21. Schematic representation of the ligands prepared by Stasiuk et al. Adapted with permission from [212], G. J. Stasiuk, et al., *ACS Nano.* 5, 8193 (2011). © 2011, ACS Publications.

QDs and the QDs-Gd^{3+} chelates were prepared using the same methodology as before [211], and it was observed that the number of complexes bonded to QDs depend on the linker, affording 115, 66, and 80 complexes per QD for QD-L1, QD-L2 and QD-L3 respectively. As observed in their previous work, no change was observed in the emission spectrum, when compared with InP/ZnS QDs. The relaxivity measurements provided values of r_1 of 21, 9, and 31.5 $mM^{-1}s^{-1}$ per Gd^{3+} ion (at 0.81 T and 25 °C) for QD-L1, QD-L2 and QD-L3 respectively. The r_1 values per QD of 2406, 585 and 2523 $mM^{-1}s^{-1}$ (at 0.81 T and 25 °C) for QD-L1, QD-L2 and QD-L3 correspondingly. QD-L3 showed the higher relaxivity, per Gd^{3+} ion and per QD, indicating that the rigidity of the linkage between the complex and the QD is higher for the benzoyl linker, decreasing more effectively the internal rotation and increasing the exchange of the coordinated water molecules, giving a higher relaxivity.

Other important factor that should be taking in attention, when applying these probes in biological systems, is that cell-internalization could affect the probe properties. This issue was studied by Starmans, et al. [213], and they observed that the internalized p-QDs-RGD and p-QDs showed lower longitudinal relaxivity, when compared with the same systems in solution. This may be explained by the fact that the internalization was mediated by endocytosis, entrapping the Gd-based CA into endosomes.

In 2015, Xing and co-authors [214] developed a paramagnetic-fluorescent nanoprobe based on CdSe QDs coated with DTPA-Gd, coupled to BSA and labeled with anti-Glut1 polyclonal antibody (^{Gd}DTPA·BSA@QDs-PcAb) for targeting colorectal cancer *in vivo* by MRI (diagnosis) and *in vitro* tissue "biopsy-imaging." BSA was an important multivalent ligand for water-solubilization hydrophobic QDs and allowed the conjugation of DTPA to BSA (confirmed by FTIR analysis) and anti-Glut1. The nanoprobes presented diameters of around 35 nm by TEM and the emission maximum at 680 nm, which was maintained for 7 days of storage.

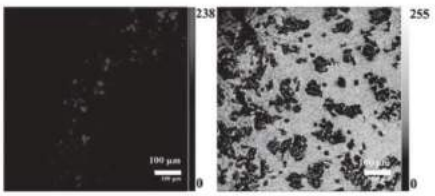

Figure 22. Confocal microscopy images of BXPC-3 cells incubated with Fe_3O_4/CIS@SiO_2 (DTPA-Gd)-RGD, when irradiated at 488 nm (A) and bright field (B). Adapted with permission from [215], J. Shen, et al., *J. Mater. Chem. B* 3, 2873 (2015). © 2015, Royal Society of Chemistry.

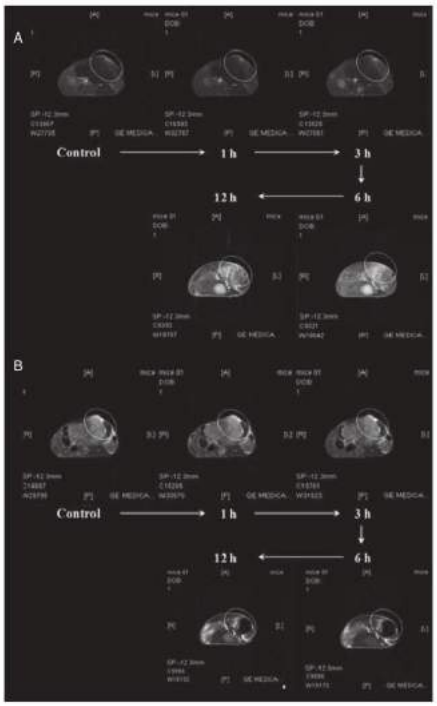

Figure 23. *In vivo* T_1-(A) and T_2-weighted (B) MR images of pancreatic adenocarcinoma obtained before injection, 1 h, 3 h, 6 h and 12 h post-injection with Fe_3O_4/CIS@SiO_2 (DTPA-Gd)-RGD. Adapted with permission from [215], J. Shen, et al., *J. Mater. Chem. B* 3, 2873 (2015). © 2015, Royal Society of Chemistry.

Table 3. Size (nm), emission wavelength (nm), and relaxivity ($mM^{-1}s^{-1}$) of the QDs associated with Gd^{3+} chelates discussed in this chapter.

Association method	Ligand	Size (nm)	λ_{em} (nm)	r_1 ($mM^{-1}s^{-1}$)[a]	Reference
Coating					
Lipids and RGD	DTPA	–	560	12[b]	[198]
Lipids and annexin	DTPA	–	560	12.4[b]	[205]
Silica	TSPETE	7–10	590	20.5[c]	[208]
Silica and lipids	DTPA	58	630	14.4[d]	[199]
Polymer	DTPA	–	574	3.72[e]	[209]
Encapsulation					
Chitosan	DTPA	50	565	33[e]	[210]
Polymers	DOTA	10.8–22-1	630	4.4–8.2[e]	[200]
Conjugation					
Disulfide bond	TACN	8.6	620	13[f]	[211]
Adsorption	DTPA	35	680	16.561[b]	[214]
Amide bond	DTPA	45	650	1.56[g]	[215]

Notes: [a] Room temperature, [b] 1.41 T, [c] 4.7 T, [d] 6.3 T, [e] 7 T, [f] 0.81 T, [g] 3 T.

The NMR analysis, confirmed high relaxivity of 16.561 (r_1) and 27.702 (r_2) $mM^{-1}s^{-1}$ per Gd^{3+} ion (at 1.4 T, 37 °C). The MTT studies showed that no significant cytotoxicity was found in 3T3 cells incubated with the bimodal nanoprobes, indicating good biocompatibility. Human colonic cancer cells (HCT116) were incubated with ^{Gd}DTPA · BSA@QDs-PcAb and the authors observed intense red fluorescence by confocal laser scanning microscopy, indicating specific binding of Glut1-targeted nanoprobes to these cancer cells. ^{Gd}DTPA · BSA@QDs-PcAb were also used as CAs for detection of tumor accumulation *in vivo* by MRI, and they showed a contrast enhancement in T_1-weighted images.

Shen et al. [215] reported multifunctional nanocomposites with (DTPA-Gd) conjugated to the surface of nanoparticles composed by superparamagnetic Fe_3O_4NPs and $CuInS_2$ (CIS) QDs coated by a silica shell (Fe_3O_4/CIS@SiO_2). Silica coating protects the Fe_3O_4 and CIS from the environment, and in addition promotes biocompatibilization (as confirmed by MTT assay on human pancreatic cancer cell line, BXPC-3 cells), essential for *in vivo* applications. This silica coating was accomplished using a mixture of tetraethyl orthosilicate (TEOS) and (3-aminopropyl) triethoxysilane (APS), resulting in an aminated surface, which allowed conjugation with Gd-DTPA complex and RGD peptides via EDC/NHS strategy, obtaining the multimodal composites Fe_3O_4/CIS@SiO_2(DTPA-Gd)-RGD. The multimodal nanocomposites presented an emission maximum at 650 nm, with a red shift in their emission spectra when compared to the QDs. These nanoprobes presented a diameter of around 45 nm, determined by TEM before and after functionalization with DTPA-Gd and RGD. This integrated nanoprobe is a platform for *in vivo* tri-mode imaging, for fluorescent imaging and for T_1- weighted positive ($r_1 = 1.56$ $mM^{-1}s^{-1}$, at 3 T) and T_2-weighted negative ($r_2 = 23.22$ $mM^{-1}s^{-1}$, at 3 T) MR imaging, improving the accuracy of the diagnosis. By confocal microscopy, it was observed that the NPs were readily internalized into BXPC-3 cells, in *in vitro* assays (Fig. 22). In relation to *in vivo* assays, the uptake of these NPs by pancreatic adenocarcinoma cell was slower compared to internalization in the *in vitro* assay. A brighter and darker enhancement effect in T_1 and T_2-weighted MRI, 6 h post-injection with improvement after 12 h, was observed (Fig. 23). The authors stated the advantage of the association of the Gd and Fe to imaging simultaneously to assist in clinical surgery.

3.4. Final Considerations About the Association of QDs and Gadolinium Chelates

In this section we presented several strategies to associate QDs to Gd^{3+} chelates that could be used for dual-imaging purposes (Table 3). Although, these bimodal probes presented good fluorescence properties and high relaxivity, some of them lack an easy preparation procedure and have multiple steps. Furthermore, the longitudinal relaxometric performance due to the presence of Gd^{3+} chelates is probably favored by changes in the water proton exchange rate between the coordinated water molecule and the bulk water (Table 3). Thus, it seems that the direct attachment of the chelate to the QD surface is a synthetic strategy with the potential to prepare efficient bimodal probes. However, the dissociation of the Gd^{3+} ions from the nanoparticle, when applied *in vivo*, is a serious concern, since it can lead to inaccurate images and the formation of $Gd(OH)_3$ is harmful to living organisms. Thus, before the *in vivo* applications, the stability toward transmetallation and leaching of the Gd^{3+} ions presented in the bimodal systems should be well studied [6, 73, 216].

4. CONCLUSION

Bimodal nanoparticles based on QDs, for optical and magnetic resonance images, have attracted much interest. In this chapter, different approaches for the development of these bimodal nanostructures were presented, such as the association of QDs to iron oxide nanoparticles, QDs' doping with paramagnetic ions, and the association of QDs and gadolinium chelates. Although many bimodal systems have been prepared, there still exists a lack in the study of these particles *in vivo*, in order to know their stability and toxicity. In the case of QD-iron oxide nanoparticles, relaxometric studies are also needed to allow comparing with other contrast agents. Thus, further development of nanoparticles for optical and MR imaging with improvement of their

properties and stability, and with flexible and simple synthetic strategies, which could allow the size and composition manipulation, and the conjugation to biomolecules for specific cellular targeting, are still required.

ACKNOWLEDGEMENTS

The authors are grateful for the discussion with the research group Nanotecnologia Biomédica/UFPE members, to Fundação de Amparo a Ciência e Tecnologia do Estado de Pernambuco (FACEPE), to Conselho Nacional de Desenvolvimento Científico e Tecnológico (CNPq), to Coordenação de Aperfeiçoamento de Pessoal de Nível Superior (CAPES), to Academia Brasileira de Ciências, to Instituto Nacional de Ciência e Tecnologia de Fotônica (INCT-INFo), and to the Universidade Federal de Pernambuco (UFPE).

GLOSSARY

Bimodal probes Bimodal probes associate two types of probes in one single system, allowing the simultaneous use of two or more diagnostic techniques. These bimodal systems aim to sum the advantages of both techniques and suppress the limitations of each one, becoming potential and innovative probes for biological investigation.

Bioconjugation A strategy to conjugate, non-covalent (by electrostatic interaction) or covalently (via coupling agents), particles and biomolecules such as amino acids, proteins, antibodies, or DNA sequences.

Contrast agents (CAs) Molecules or particles used to enhance the quality of the images generated by magnetic resonance. The MRI CAs approved for clinical use are based on paramagnetic chelates containing a lanthanide ion, namely gadolinium (III), and iron oxide particles.

Doped QDs QDs containing dopant ions in their crystalline lattice, which change their electronic and photophysical properties. An effective doping procedure requires the replacement of some atoms of the host QD's crystal structure by adequate ions, creating new defined electronic states inside the band gap region.

Fluorescence A rapid process of light emission (10^{-9} to 10^{-7} seconds) by a substance/particle when decaying from the electronic excited state, after absorption of light.

Functionalization Surface particle modification with functional groups, such as amine, carboxyl, or thiol groups, in order to make them able to bind to organic molecules.

Gadolinium chelates Coordination compounds containing gadolinium as metal ion and organic molecules as ligands. The gadolinium chelates are clinically used as MRI CAs, since they avoid the free gadolinium and consequently its toxicity.

Magnetic resonance imaging (MRI Diagnostic image technique based on the nuclear magnetic resonance (NMR) phenomenon. This technique is non-invasive, has a high spatial resolution (0.2–0.3 mm) giving images with anatomical details, and does not use ionizing radiation. MRI is a very efficient technique to reveal differences in the water constitution of the different body tissues, revealing the existence of anomalies in the soft tissues of the body.

Non-specific labeling/marker Cell labeling promoted by a direct interaction with chemical structures, without a specific target.

Optical imaging Technique that relies on the acquisition of images by using light excitation (ultraviolet, visible, or infrared regions of the electromagnetic spectrum). This technique uses fluorescent labels (frequently organic fluorophores) to evidence the desired structures or biomolecules.

Quantum dots (QDs) Fluorescent semiconductor nanocrystals quantum-confined in three dimensions, with a size of 1.5 to 10 nm. QDs have unique photophysical properties, such as photostability, fluorescence tuned with their size, and a chemically active surface. Due to their optical properties, they have been studied as probes in biomedical sciences and in electronic devices.

Quantum yield (QY) Parameter used to determine the efficiency of the fluorescence process. It is defined by the ratio between the number of emitted photons and the number of absorbed photons per time unit.

Relaxation times The relaxation process is modulated by two exponential time constants, T_1 and T_2, which depend on the physical and chemical properties of the environment. In practice, it results in differences on the generated image for local chemically and/or morphologically different tissues.

Relaxivity (r_i, $i = 1,2$) Parameter used to determine of the contrast agent efficiency, and it is given in s^{-1} by mM of paramagnetic ion. This parameter indicates the CAs ability to decrease the relaxation times of the water molecules protons that are located near the paramagnetic system.

Saturation magnetization (Ms) The *Ms* value indicates the higher magnetization of the material, beyond this value no further increase in magnetization occurs, meaning that all the single domains are aligned with the field.

Specific labeling/marker Cells labeling mediated by antibodies or other biomolecules, which provide a specific direction to target.

Superparamagnetic iron oxide nanoparticles Nanoparticles composed by an iron oxide core and in an uniform magnetization state, which means that after removal of the external magnetic field they lose their magnetization.

T_1 The longitudinal or spin-lattice relaxation. Reflects the relaxation due to the energy loss for the neighborhood and gives information about the recuperation velocity of the system's magnetization parallel to the static magnetic field after a perturbation is applied.

T_2 The transverse or spin-spin relaxation. The relaxation due to the interactions between the spins (dipolar interactions) and related to the quickness of coherence losses of the magnetization in the plane transverse to the static magnetic field.

REFERENCES

1. Y.-P. Ho and K. W. Leong, Quantum dot-based theranostics. *Nanoscale* 2, 60 (2010).
2. S. P. Singh, Multifunctional magnetic quantum dots for cancer theranostics. *J. Biomed. Nanotechnol.* 7, 95 (2011).
3. F. Lux, L. Sancey, A. Bianchi, Y. Crémillieux, S. Roux, and O. Tillement, Gadolinium-based nanoparticles for theranostic MRI-radiosensitization. *Nanomedicine* 10, 1801 (2015).

4. R. Hachani, M. Lowdell, M. Birchall, and N. N. T. K. Thanh, Tracking stem cells in tissue-engineered organs using magnetic nanoparticles. *Nanoscale* 5, 11362 (2013).
5. D. P. Cormode, B. L. Sanchez-Gaytan, A. J. Mieszawska, Z. A. Fayad, and W. J. M. Mulder, Inorganic nanocrystals as contrast agents in MRI: Synthesis, coating and introduction of multifunctionality. *NMR in Biomed.* 26, 766 (2013).
6. L. Jing, K. Ding, S. V. Kershaw, I. M. Kempson, A. L. Rogach, and M. Gao, Magnetically engineered semiconductor quantum dots as multimodal imaging probes. *Adv. Mat.* 26, 6367 (2014).
7. H. Xu, Q. Li, L. Wang, Y. He, J. Shi, B. Tang, and C. Fan, Nanoscale optical probes for cellular imaging. *Chem. Soc. Rev.* 43, 2650 (2014).
8. K. M. Dean and A. E. Palmer, Advances in fluorescence labeling strategies for dynamic cellular imaging. *Nat. Chem. Biol.* 10, 512 (2014).
9. Z. Guo, S. Park, J. Yoon, and I. Shin, Recent progress in the development of near-infrared fluorescent probes for bioimaging applications. *Chem. Soc. Rev.* 43, 16 (2014).
10. P. W. Winter and H. Shroff, Faster fluorescence microscopy: Advances in high speed biological imaging. *Curr. Opin. Chem. Biol.* 20, 46 (2014).
11. A. J. Meixner, The nobel prize in chemistry 2014 for the development of super-resolved fluorescence microscopy. *Anal. Bioanal. Chem.* 407, 1797 (2015).
12. B. N. G. Giepmans, S. R. Adams, M. H. Ellisman, and R. Y. Tsien, The fluorescent toolbox for assessing protein location and function. *Science* 312, 217 (2006).
13. U. Resch-Genger, M. Grabolle, S. Cavaliere-Jaricot, R. Nitschke, and T. Nann, Quantum dots versus organic dyes as fluorescent labels. *Nat. Meth.* 5, 763 (2008).
14. A. Fontes, R. B. D. Lira, M. A. B. L. Seabra, T. G. D. Silva, A. G. D. C. Neto, and B. S. Santos, "Biomedical Engineering—Technical Applications in Medicine" (R. Hudak, Ed.), InTech. 2012.
15. C. L. Cesar, "Quantum Dots: Applications in Biology," pp. 3–9. Springer, 2014.
16. S. K. Vashist, R. Tewari, R. P. Bajpai, L. M. Bharadwaj, and R. Raiteri, Review of quantum dot technologies for cancer detection and treatment. *AZojono J. Nanotechnology Online* 2, 1 (2006).
17. B. S. Santos, P. M. A. Farias, and A. Fontes, "Handbook of Self Assembled Semiconductor Nanostructures for Novel Devices in Photonics and Electronics" (M. Henini, Ed.). pp. 773–798. Elsevier, Amsterdam, 2008.
18. Y. Wang and L. Chen, Quantum dots, lighting up the research and development of nanomedicine. *Nanomed. Nanotechnol. Biol. Med.* 7, 385 (2011).
19. L.-W. Wang, C.-W. Peng, C. Chen, and Y. Li, Quantum dots-based tissue and *in vivo* imaging in breast cancer researches: Current status and future perspectives. *Breast Cancer Res. Treat* 151, 7 (2015).
20. K. D. Wegner and N. Hildebrandt, Quantum dots: Bright and versatile *in vitro* and *in vivo* fluorescence imaging biosensors. *Chem. Soc. Rev.* (2015).
21. G. A. Pereira and C. F. G. C. Geraldes, Design and optimization of gadolinium based contrast agents for magnetic resonance imaging. *Ann. Magn. Reson.* 6, 1 (2007).
22. W. Cai, K. Chen, Z.-B. Li, S. S. Gambhir, and X. Chen, Dual-function probe for PET and near-infrared fluorescence imaging of tumor vasculature. *J. Nucl. Med.* 48, 1862 (2007).
23. K. Chen, Z.-B. Li, H. Wang, W. Cai, and X. Chen, Dual-modality optical and positron emission tomography imaging of vascular endothelial growth factor receptor on tumor vasculature using quantum dots. *Eur. J. Nucl. Med. Mol. Imaging* 35, 2235 (2008).
24. C. Tu, X. Ma, A. House, S. M. Kauzlarich, and A. Y. Louie, PET imaging and biodistribution of silicon quantum dots in mice. *ACS Med. Chem. Lett.* 2, 285 (2011).
25. W. Guo, X. Sun, O. Jacobson, X. Yan, K. Min, A. Srivatsan, G. Niu, D. O. Kiesewetter, J. Chang, and X. Chen, Intrinsically radioactive [64Cu]CuInS/ZnS quantum dots for PET and optical imaging: Improved radiochemical stability and controllable cerenkov luminescence. *ACS Nano.* 9, 488 (2015).
26. I. L. Medintz, H. T. Uyeda, E. R. Goldman, and H. Mattoussi, Quantum dot bioconjugates for imaging, labelling and sensing. *Nat. Mater.* 4, 435 (2005).
27. X. Michalet, F. F. Pinaud, L. A. Bentolila, J. M. Tsay, S. Doose, J. J. Li, G. Sundaresan, A. M. Wu, S. S. Gambhir, and S. Weiss, Quantum dots for live cells, *in vivo* imaging, and diagnostics. *Science* 307, 538 (2005).
28. L. Shao, Y. Gao, and F. Yan, Semiconductor quantum dots for biomedicial applications. *Sensors* 11, 11736 (2011).
29. X. Michalet, L. A. Bentolila, and S. Weiss, Eds., "Molecular Imaging: Physics and Bioapplications of Quantum Dots" 2008.
30. A. M. Smith, X. Gao, and S. Nie, Quantum dot nanocrystals for *in vivo* molecular and cellular imaging. *Photochem. Photobiol.* 80, 377, (2004).
31. L. E. Brus, Electron–electron and electron–hole interactions in small semiconductor crystallites: The size dependence of the lowest excited electronic state. *J. Chem. Phys.* 80, 6 (1984).
32. P. Petroff, "Single Quantum Dots," Vol. 90, pp. 1–24, Springer Berlin, Heidelberg, 2003.
33. B. O. Dabbousi, J. Rodriguez-Viejo, F. V. Mikulec, J. R. Heine, H. Mattoussi, R. Ober, K. F. Jensen, and M. G. Bawendi, (CdSe)ZnS core–shell quantum dots: Synthesis and characterization of a size series of highly luminescent nanocrystallites. *J. Phys. Chem. B* 101, 9463 (1997).
34. Y. Xiao, S. P. Forry, X. Gao, R. D. Holbrook, W. G. Telford, and A. Tona, Research dynamics and mechanisms of quantum dot nanoparticle cellular uptake. *J. Nanobiotechnology* 8 (2010).
35. X. Wu, H. Liu, J. Liu, K. N. Haley, J. A. Treadway, J. P. Larson, N. Ge, F. Peale, and M. P. Bruchez, Immunofluorescent labeling of cancer marker Her2 and other cellular targets with semiconductor quantum dots. *Nat. Biotech.* 21, 41 (2003).
36. P. Alivisatos, The use of nanocrystals in biological detection. *Nat. Biotech.* 22, 47 (2004).
37. T. Jamieson, R. Bakhshi, D. Petrova, R. Pocock, M. Imani, and A. M. Seifalian, Biological applications of quantum dots. *Biomaterials* 28, 4717 (2007).
38. A. Sukhanova and I. Nabiev, Fluorescent nanocrystal quantum dots as medical diagnostic tools. *Expert. Opin Med. Diagn.* 2, 429 (2008).
39. M. A. Walling, J. A. Novak, and J. R. Shepard, Quantum dots for live cell and *in vivo* imaging. *Int. J. Mol. Sci.* 10, 441 (2009).
40. W. C. W. Chan, D. J. Maxwell, X. Gao, R. E. Bailey, M. Han, and S. Nie, Luminescent quantum dots for multiplexed biological detection and imaging. *Curr. Opin Biotechnol.* 13, 40 (2002).
41. O. I. Micić and A. J. Nozik, "Nanostructured Materials and Nanotechnology," (H. S. Nalwa, Ed.). pp. 183–205. Academic Press, San Diego, 2002.
42. F. D. Menezes, A. G. Brasil Jr., W. L. Moreira, L. C. Barbosa, C. L. Cesar, R. D. C. Ferreira, P. M. A. de Farias, and B. S. Santos, CdTe/CdS core shell quantum dots for photonic applications. *Microelectr. J.* 36, 989 (2005).
43. C. Carrillo-Carrion, S. Cardenas, B. M. Simonet, and M. Valcarcel, Quantum dots luminescence enhancement due to illumination with UV/Vis light. *Chem Comm.* 5214 (2009).
44. E. R. Goldman, G. P. Anderson, P. T. Tran, H. Mattoussi, P. T. Charles, and J. M. Mauro, Conjugation of luminescent quantum dots with antibodies using an engineered adaptor protein to provide new reagents for fluoroimmunoassays. *Anal. Chem.* 74, 841 (2002).
45. X. Gao, L. Yang, J. A. Petros, F. F. Marshall, J. W. Simons, and S. Nie, *In vivo* molecular and cellular imaging with quantum dots. *Curr. Opin. Biotechnol.* 16, 63 (2005).
46. K. H. G. Carvalho, A. G. Brasil Jr., P. E. Cabral Filho, D. P. L. A. Tenorio, A. C. A. de Siqueira, E. S. Leite, A. Fontes, and B. S.

Santos, Fluorescence plate reader for quantum dot-protein bioconjugation analysis. *J. Nanosci. Nanotechnol.* 14, 3320 (2014).
47. G. T. Hermanson, "Bioconjugate Techniques" (G. T. Hermanson, Ed.), pp. 169–212, Academic Press, New York, 2008.
48. G. T. Hermanson, "Bioconjugate Techniques" (G. T. Hermanson, Ed.), pp. 213–233, Academic Press, New York, 2008.
49. C. G. Andrade, P. E. Cabral Filho, D. P. L. Tenório, B. S. Santos, E. I. C. Beltrão, A. Fontes, and L. B. Carvalho Jr., Evaluation of glycophenotype in breast cancer by quantum dot-lectin histochemistry. *Int. J. Nanomedicine.* 8, 4623 (2013).
50. A. Fontes and B. S. Santos, "Quantum Dots: Applications in Biology" Springer, 2014.
51. D. P. L. A. Tenório, C. G. Andrade, P. E. Cabral Filho, C. P. Sabino, I. T. Kato, L. B. Carvalho Jr., S. Alves Jr, M. S. Ribeiro, A. Fontes, and B. S. Santos, CdTe quantum dots conjugated to concanavalin A as potential fluorescent molecular probes for saccharides detection in Candida albicans. *J. Photochem. Photobiol. B Biol.* 142, 237 (2015).
52. P. E. Cabral Filho, M. I. A. Pereira, H. P. Fernandes, A. A. de Thomaz, C. L. Cesar, B. S. Santos, M. L. Barjas-Castro, and A. Fontes, Blood group antigen studies using CdTe quantum dots and flow cytometry. *Int. J. Nanomedicine* 10, 4393 (2015).
53. M.-Z. Zhang, R.-N. Yu, J. Chen, Z.-Y. Ma, and Y.-D. Zhao, Targeted quantum dots fluorescence probes functionalized with aptamer and peptide for transferrin receptor on tumor cells. *Nanotechnology* 23, 485104 (2012).
54. P. E. Cabral Filho, A. L. C. Cardoso, M. I. A. Pereira, A. P. M. Ramos, F. Hallwas, M. M. C. A. Castro, C. F. G. C. Geraldes, B. S. Santos, M. C. Pedroso de Lima, G. A. L. Pereira, and A. Fontes, CdTe quantum dots as fluorescent probes to study transferrin receptors in glioblastoma cells. *Biochimica et Biophysica Acta (BBA)-General Subjects* 1860, 28 (2016).
55. C. G. Andrade, P. E. Cabral Filho, D. P. L. Tenório, B. S. Santos, E. I. C. Beltrão, A. Fontes, and L. B. Carvalho, Evaluation of glycophenotype in breast cancer by quantum dot-lectin histochemistry. *Int. J. Nanomedicine.* 8, 4623 (2013).
56. D. P. L. A. Tenório, C. G. Andrade, P. E. Cabral Filho, C. P. Sabino, I. T. Kato, L. B. Carvalho Jr., S. Alves Jr., M. S. Ribeiro, A. Fontes, and B. S. Santos, CdTe quantum dots conjugated to concanavalin A as potential fluorescent molecular probes for saccharides detection in Candida albicans. *Journal of Photochemistry and Photobiology B: Biology* 142, 237 (2015).
57. V. Biju, T. Itoh, and M. Ishikawa, Delivering quantum dots to cells: Bioconjugated quantum dots for targeted and nonspecific extracellular and intracellular imaging. *Chem. Soc. Rev.* 39, 3031 (2010).
58. K. Klepárník, V. Datinská, I. Voráčová, and M. Lišková, "Quantum Dots: Applications in Biology," (A. Fontes and B. S. Santos, Eds.). Vol. 1199, pp. 33–54. Springer, New York, 2014.
59. K. Brazhnik, I. Nabiev, and A. Sukhanova, "Quantum Dots: Applications in Biology," (A. Fontes and B. S. Santos, Eds.), Vol. 1199, pp. 55–66. Springer, New York, 2014.
60. D. East, M. Todd, and I. Bruce, "Quantum Dots: Applications in Biology," (A. Fontes and B. S. Santos, Eds.), Vol. 1199, pp. 67–83. Springer, New York, 2014.
61. A. G. Brasil Jr., K. H. G. Carvalho, E. S. Leite, A. Fontes, and B. S. Santos, Quantum Dots: Applications in Biology, (A. Fontes and B. S. Santos, Eds.), Vol. 1199, pp. 103–110, Springer, New York, 2014.
62. L. Landini, V. Positano, and M. Santarelli, Advanced image processing in magnetic resonance imaging. *Taylor and Francis Group* (2005).
63. R. B. Buxton, "Introduction to Functional Magnetic Resonance Imaging: Principles and Techniques," pp. 67–84, Cambridge University Press, 2009.
64. R. Damadian, Tumor detection by nuclear magnetic resonance. *Science* 171, 1151 (1971).
65. P. C. Lauterbur, Image formation by induced local interactions: Examples employing nuclear magnetic resonance. *Nature* 242, 190 (1973).
66. A. Merbach, L. Helm, and É. Tóth, Eds., "The Chemistry of Contrast Agents in Medical Magnetic Resonance Imaging," John Wiley & Sons, Ltd, Chichester, UK, 2013.
67. T. Lam, P. Pouliot, P. K. Avti, F. Lesage, and A. K. Kakkar, Superparamagnetic iron oxide based nanoprobes for imaging and theranostics. *Adv. Colloid Interface Sci.* 199–200, 95 (2013).
68. R. R. Edelman and S. Warach, Magnetic resonance imaging. *N. Engl. J. Med.* 328, 708 (1993).
69. G.-P. Yan, L. Robinson, and P. Hogg, Magnetic resonance imaging contrast agents: Overview and perspectives. *Radiography* 13, e5 (2007).
70. J. S. Weinstein, C. G. Varallyay, E. Dosa, S. Gahramanov, B. Hamilton, W. D. Rooney, L. L. Muldoon, and E. A. Neuwelt, Superparamagnetic iron oxide nanoparticles: Diagnostic magnetic resonance imaging and potential therapeutic applications in neurooncology and central nervous system inflammatory pathologies, a review. *J. Cereb. Blood Flow Metab.* 30, 15 (2010).
71. S. Laurent, D. Forge, M. Port, A. Roch, C. Robic, L. Vander Elst, and R. N. Muller, Magnetic iron oxide nanoparticles: Synthesis, stabilization, vectorization, physicochemical characterizations, and biological applications. *Chem. Rev.* 108, 2064 (2008).
72. C. Henoumont, S. Laurent, and L. Vander Elst, How to perform accurate and reliable measurements of longitudinal and transverse relaxation times of MRI contrast media in aqueous solutions. *Contrast Media Mol. Imaging* 4, 312 (2009).
73. C. F. G. C. Geraldes and S. Laurent, Classification and basic properties of contrast agents for magnetic resonance imaging. *Contrast Media Mol. Imaging* 4, 1 (2009).
74. H. B. Na, I. C. Song, and T. Hyeon, Inorganic nanoparticles for MRI contrast agents. *Adv. Mat.* 21, 2133 (2009).
75. S. H. Lee, B. H. Kim, H. B. Na, and T. Hyeon, Paramagnetic inorganic nanoparticles as T_1 MRI contrast agents. *Wiley Interdiscip Rev: Nanomed. Nanobiotechnol.* 6, 196 (2014).
76. M. A. Bruckman, X. Yu, and N. F. Steinmetz, Engineering Gd-loaded nanoparticles to enhance MRI sensitivity via T 1 shortening. *Nanotechnology* 24, 462001 (2013).
77. F. Mouffouk, T. Simão, D. F. Dornelles, A. D. Lopes, P. Sau, J. Martins, K. M. Abu-Salah, S. A. Alrokayan, A. M. Rosa da Costa, and N. R. dos Santos, Self-assembled polymeric nanoparticles as new, smart contrast agents for cancer early detection using magnetic resonance imaging. *Int. J. Nanomedicine.* 10, 63 (2015).
78. R. Srikar, A. Upendran, and R. Kannan, Polymeric nanoparticles for molecular imaging. *Wiley Interdiscip Rev Nanomed Nanobiotechnol.* 6, 245 (2014).
79. J. L. Turner, D. Pan, R. Plummer, Z. Chen, A. K. Whittaker, and K. L. Wooley, Synthesis of gadolinium-labeled shell-crosslinked nanoparticles for magnetic resonance imaging applications. *Adv. Funct. Materials* 15, 1248 (2005).
80. E. Chung, F. Pineda, K. Nord, and L. S. Karczmar, Fibrin-targeting, peptide amphiphile micelles as contrast agents for molecular MRI. *J. Cell. Sci. Ther.* 5, 2 (2014).
81. K. B. Vargo, A. A. Zaki, R. Warden-Rothman, A. Tsourkas, and D. A. Hammer, Superparamagnetic iron oxide nanoparticle micelles stabilized by recombinant oleosin for targeted magnetic resonance imaging. *Small* n/a–n/a (2014).
82. B. Sitharaman, K. R. Kissell, K. B. Hartman, L. A. Tran, A. Baikalov, I. Rusakova, Y. Sun, H. A. Khant, S. J. Ludtke, W. Chiu, S. Laus, E. Toth, L. Helm, A. E. Merbach, and L. J. Wilson, Superparamagnetic gadonanotubes are high-performance MRI contrast agents. *Chem. Comm.* 3915 (2005).
83. N. KuŸnik, M. M. Tomczyk, S. Boncel, A. P. Herman, K. K. K. Koziol, and M. Kempka, Fe3 + ions anchored to Fe@O-MWCNTs as double impact T_2 MRI contrast agents. *Mater Lett.* 136, 34 (2014).

84. I. Marangon, C. Ménard-Moyon, J. Kolosnjaj-Tabi, M. L. Béoutis, L. Lartigue, D. Alloyeau, E. Pach, B. Ballesteros, G. Autret, T. Ninjbadgar, D. F. Brougham, A. Bianco, and F. Gazeau, Covalent functionalization of multi-walled carbon nanotubes with a gadolinium chelate for efficient T_1-weighted magnetic resonance imaging. *Adv. Funct. Mater.* 24, 7173 (2014).
85. L. Zhang, H. Zhou, O. Belzile, P. Thorpe, and D. Zhao, Phosphatidylserine-targeted bimodal liposomal nanoparticles for *in vivo* imaging of breast cancer in mice. *J. Control Release* 183, 114 (2014).
86. G. Mulas, G. Ferrauto, W. Dastrù, R. Anedda, S. Aime, and E. Terreno, Insights on the relaxation of liposomes encapsulating paramagnetic Ln-based complexes. *Magn. Reson. Med.* n/a (2014).
87. H. Kobayashi and M. W. Brechbiel, Nano-sized MRI contrast agents with dendrimer cores. *Adv. Drug. Deliv. Rev.* 57, 2271 (2005).
88. J. Zhu, E. M. Gale, I. Atanasova, T. A. Rietz, and P. Caravan, Hexameric MnII dendrimer as MRI contrast agent. *Chem. Eur. J.* 20, 14507 (2014).
89. B. B. Bartelle, M. D. Mana, G. A. Suero-Abreu, J. J. Rodriguez, and D. H. Turnbull, Engineering an effective Mn-binding MRI reporter protein by subcellular targeting. *Magn. Reson. Med.* n/a (2014).
90. L. I. Liron, I. K. Elena, A. B. Anna, M. S. Alexander, R. Ina, K. Jörg, P. Lorena, and L. Jean-Paul, Towards hybrid biocompatible magnetic rHuman serum albumin-based nanoparticles: Use of ultra-small (CeL n) 3/4 + cation-doped maghemite nanoparticles as functional shell. *Nanotechnology* 26, 045601 (2015).
91. C. Zeng, X. Shi, B. Wu, D. Zhang, and W. Zhang, Colloids containing gadolinium-capped gold nanoparticles as high relaxivity dual-modality contrast agents for CT and MRI. *Colloids Surf. B* 123, 130 (2014).
92. M. F. Ferreira, J. Goncalves, B. Mousavi, M. I. M. Prata, S. P. J. Rodrigues, D. Calle, P. Lopez-Larrubia, S. Cerdan, T. B. Rodrigues, P. M. Ferreira, L. Helm, J. A. Martins, and C. F. G. C. Geraldes, Gold nanoparticles functionalised with fast water exchanging Gd3 + chelates: Linker effects on the relaxivity. *Dalton Trans.* (2015).
93. Y. Gossuin, P. Gillis, A. Hocq, Q. L. Vuong, and A. Roch, Magnetic resonance relaxation properties of superparamagnetic particles. *Wiley Interdiscip Rev. Nanomed. Nanobiotechnol.* 1, 299 (2009).
94. P. Caravan, J. J. Ellison, T. J. McMurry, and R. B. Lauffer, Gadolinium (III) chelates as MRI contrast agents: Structure, dynamics, and applications. *Chem. Rev.* 99, 2293 (1999).
95. R. López-Cebral, M. Martín-Pastor, B. Seijo, and A. Sanchez, Progress in the characterization of bio-functionalized nanoparticles using NMR methods and their applications as MRI contrast agents. *Prog. Nucl. Magn. Reson. Spectrosc.* 79, 1 (2014).
96. Y. Liu, K. Ai, Q. Yuan, and L. Lu, Fluorescence-enhanced gadolinium-doped zinc oxide quantum dots for magnetic resonance and fluorescence imaging. *Biomaterials* 32, 1185 (2011).
97. J. Yang, J. Gunn, S. R. Dave, M. Zhang, Y. A. Wang, and X. Gao, Ultrasensitive detection and molecular imaging with magnetic nanoparticles. *Analyst* 133, 154 (2008).
98. P. B. Santhosh and N. P. Ulrih, Multifunctional superparamagnetic iron oxide nanoparticles: Promising tools in cancer theranostics. *Cancer Lett.* 336, 8 (2013).
99. D. Koktysh, V. Bright, and W. Pham, Fluorescent magnetic hybrid nanoprobe for multimodal bioimaging. *Nanotechnology* 22, 275606 (2011).
100. A. K. Gupta and M. Gupta, Synthesis and surface engineering of iron oxide nanoparticles for biomedical applications. *Biomaterials* 26, 3995 (2005).
101. A. S. Teja and P.-Y. Koh, Synthesis, properties, and applications of magnetic iron oxide nanoparticles. *Prog. Cryst. Growth Charact. Mater.* 55, 22 (2009).
102. M. Mahmoudi, S. Sant, B. Wang, S. Laurent, and T. Sen, Superparamagnetic iron oxide nanoparticles (SPIONs): Development, surface modification and applications in chemotherapy. *Adv. Drug. Deliv. Rev.* 63, 24 (2011).
103. A. K. Gupta, R. R. Naregalkar, V. D. Vaidya, and M. Gupta, Recent advances on surface engineering of magnetic iron oxide nanoparticles and their biomedical applications. *Nanomedicine* 2, 23 (2007).
104. A. Ito, M. Shinkai, H. Honda, and T. Kobayashi, Medical application of functionalized magnetic nanoparticles. *J. Biosci. Bioeng.* 100, 1 (2005).
105. R. Jurgons, C. Seliger, A. Hilpert, L. Trahms, S. Odenbach, and C. Alexiou, Drug loaded magnetic nanoparticles for cancer therapy. *J. Phys. Condens. Matter.* 18, S2893 (2006).
106. R. Weissleder, Molecular imaging in cancer. *Science* 312, 1168 (2006).
107. R. A. Frimpong and J. Z. Hilt, Magnetic nanoparticles in biomedicine: Synthesis, functionalization and applications. *Nanomedicine* 5, 1401 (2010).
108. L. H. Reddy, J. L. Arias, J. Nicolas, and P. Couvreur, Magnetic nanoparticles: Design and characterization, toxicity and biocompatibility, pharmaceutical and biomedical applications. *Chem. Rev.* 112, 5818 (2012).
109. Q. A. Pankhurst, J. Connolly, S. Jones, and J. Dobson, Applications of magnetic nanoparticles in biomedicine. *J. Phys. D: Appl. Phys.* 36, R167 (2003).
110. D. Jańczewski, Y. Zhang, G. K. Das, D. K. Yi, P. Padmanabhan, K. K. Bhakoo, T. T. Y. Tan, and S. T. Selvan, Bimodal magnetic–fluorescent probes for bioimaging. *Microsc ResTech.* 74, 563 (2011).
111. Z. R. Stephen, F. M. Kievit, and M. Zhang, Magnetite nanoparticles for medical MR imaging. *Mater. Today* 14, 330 (2011).
112. H. Jaganathan and A. Ivanisevic, "Nanobiomaterials Handbook," (B. Sitharaman Ed.), pp. 1–17, CRC Press, 2011.
113. A.-H. Lu, E. L. Salabas, and F. Schüth, Magnetic nanoparticles: Synthesis, protection, functionalization, and application. *Angew. Chem. Int. Ed.* 46, 1222 (2007).
114. S. L. C. Pinho, G. A. Pereira, P. Voisin, J. Kassem, V. Bouchaud, L. Etienne, J. A. Peters, L. Carlos, S. Mornet, C. F. G. C. Geraldes, J. Rocha, and M.-H. Delville, Fine tuning of the relaxometry of ã-Fe_2O_3@SiO_2 Nanoparticles by tweaking the silica coating thickness. *ACS Nano* 4, 5339 (2010).
115. N. Insin, J. B. Tracy, H. Lee, J. P. Zimmer, R. M. Westervelt, and M. G. Bawendi, Incorporation of iron oxide nanoparticles and quantum dots into silica microspheres. *ACS Nano* 2, 197 (2008).
116. J. Ruan, J. Ji, H. Song, Q. Qian, K. Wang, C. Wang, and D. Cui, Fluorescent magnetic nanoparticle-labeled mesenchymal stem cells for targeted imaging and hyperthermia therapy of in vivo gastric cancer. *Nanoscale Res. Lett.* 7, 1 (2012).
117. G. Ruan, G. Vieira, T. Henighan, A. Chen, D. Thakur, R. Sooryakumar, and J. O. Winter, Simultaneous magnetic manipulation and fluorescent tracking of multiple individual hybrid nanostructures. *Nano Lett.* 10, 2220 (2010).
118. E.-Q. Song, J. Hu, C.-Y. Wen, Z.-Q. Tian, X. Yu, Z.-L. Zhang, Y.-B. Shi, and D.-W. Pang, Fluorescent-magnetic-biotargeting multifunctional nanobioprobes for detecting and isolating multiple types of tumor cells. *ACS Nano* 5, 761 (2011).
119. A. Kale, S. Kale, P. Yadav, H. Gholap, R. Pasricha, J. Jog, B. Lefez, B. Hannoyer, P. Shastry, and S. Ogale, Magnetite/CdTe magnetic–fluorescent composite nanosystem for magnetic separation and bio-imaging. *Nanotechnology* 22, 225101 (2011).
120. D. Thakur, S. Deng, T. Baldet, and J. O. Winter, pH sensitive CdS–iron oxide fluorescent–magnetic nanocomposites. *Nanotechnology* 20, 485601 (2009).
121. S. R. Ahmed, J. Dong, M. Yui, T. Kato, J. Lee, and E. Y. Park, Quantum dots incorporated magnetic nanoparticles for imaging colon carcinoma cells. *J. Nanobiotechnology* 11, 28 (2013).

122. X. You, R. He, F. Gao, J. Shao, B. Pan, and D. Cui, Hydrophilic high-luminescent magnetic nanocomposites. *Nanotechnology* 18, 035701 (2007).
123. D. Wang, J. He, N. Rosenzweig, and Z. Rosenzweig, Superparamagnetic Fe_2O_3 beads-CdSe/ZnS quantum dots core–shell nanocomposite particles for cell separation. *Nano Lett.* 4, 409 (2004).
124. Y. Zhang, S.-N. Wang, S. Ma, J.-J. Guan, D. Li, X.-D. Zhang, and Z.-D. Zhang, Self-assembly multifunctional nanocomposites with Fe_3O_4 magnetic core and CdSe/ZnS quantum dots shell. *J. Biomed. Mater. Res. A* 85A, 840 (2008).
125. D. Wang, J. He, N. Rosenzweig, and Z. Rosenzweig, Superparamagnetic Fe_2O_3 beads-CdSe/ZnS quantum dots core–shell nanocomposite particles for cell separation. *Nano Lett.* 4, 409 (2004).
126. P. Sun, H. Zhang, C. Liu, J. Fang, M. Wang, J. Chen, J. Zhang, C. Mao, and S. Xu, Preparation and characterization of Fe_2O_3/CdTe magnetic/fluorescent nanocomposites and their applications in immuno-labeling and fluorescent imaging of cancer cells. *Langmuir* 26, 1278 (2009).
127. D. K. Yi, S. T. Selvan, S. S. Lee, G. C. Papaefthymiou, D. Kundaliya, and J. Y. Ying, Silica-coated nanocomposites of magnetic nanoparticles and quantum dots. *J. Am. Chem. Soc.* 127, 4990 (2005).
128. Q. Wang, Y. Liu, C. Lin, and H. Yan, Layer-by-layer growth of superparamagnetic, fluorescent barcode nanospheres. *Nanotechnology* 18, 405604 (2007).
129. S. T. Selvan, P. K. Patra, C. Y. Ang, and J. Y. Ying, Synthesis of silica-coated semiconductor and magnetic quantum dots and their use in the imaging of live cells. *Angew. Chem. Int. Ed.* 46, 2448 (2007).
130. R. He, X. You, J. Shao, F. Gao, B. Pan, and D. Cui, Core/shell fluorescent magnetic silica-coated composite nanoparticles for bioconjugation. *Nanotechnology* 18, 315601 (2007).
131. L. Li, E. S. G. Choo, Z. Liu, J. Ding, and J. Xue, Double-layer silica core–shell nanospheres with superparamagnetic and fluorescent functionalities. *Chem. Phys. Lett.* 461, 114 (2008).
132. B. Liu, W. Xie, D. Wang, W. Huang, M. Yu, and A. Yao, Preparation and characterization of magnetic luminescent nanocomposite particles. *Mater. Lett.* 62, 3014 (2008).
133. O. Chen, L. Riedemann, F. Etoc, H. Herrmann, M. Coppey, M. Barch, C. T. Farrar, J. Zhao, O. T. Bruns, and H. Wei, Magneto-fluorescent core–shell supernanoparticles. *Nature Comm.* 5 (2014).
134. V. Salgueiriño-Maceira, M. A. Correa-Duarte, M. Spasova, L. M. Liz-Marzán, and M. Farle, Composite silica spheres with magnetic and luminescent functionalities. *Adv. Funct. Mater.* 16, 509 (2006).
135. D. Cui, Y. Han, Z. Li, H. Song, K. Wang, R. He, B. Liu, H. Liu, C. Bao, and P. Huang, Fluorescent magnetic nanoprobes for *in vivo* targeted imaging and hyperthermia therapy of prostate cancer. *Nano Biomed. Eng.* 1, 94 (2009).
136. Q. Ma, Y. Nakane, Y. Mori, M. Hasegawa, Y. Yoshioka, T. M. Watanabe, K. Gonda, N. Ohuchi, and T. Jin, Multilayered, core/shell nanoprobes based on magnetic ferric oxide particles and quantum dots for multimodality imaging of breast cancer tumors. *Biomaterials* 33, 8486 (2012).
137. G.-P. Wang, E.-Q. Song, H.-Y. Xie, Z.-L. Zhang, Z.-Q. Tian, C. Zuo, D.-W. Pang, D.-C. Wu, and Y.-B. Shi, Biofunctionalization of fluorescent-magnetic-bifunctional nanospheres and their applications. *Chem. Comm.* 4276 (2005).
138. T. R. Sathe, A. Agrawal, and S. Nie, Mesoporous silica beads embedded with semiconductor quantum dots and iron oxide nanocrystals: Dual-function microcarriers for optical encoding and magnetic separation. *Anal. Chem.* 78, 5627 (2006).
139. L. Li, D. Chen, Y. Zhang, Z. Deng, X. Ren, X. Meng, F. Tang, J. Ren, and L. Zhang, Magnetic and fluorescent multifunctional chitosan nanoparticles as a smart drug delivery system. *Nanotechnology* 18, 405102 (2007).
140. C. Tu, Y. Yang, and M. Gao, Preparations of bifunctional polymeric beads simultaneously incorporated with fluorescent quantum dots and magnetic nanocrystals. *Nanotechnology* 19, 105601 (2008).
141. Y. F. Tan, P. Chandrasekharan, D. Maity, C. X. Yong, K.-H. Chuang, Y. Zhao, S. Wang, J. Ding, and S.-S. Feng, Multimodal tumor imaging by iron oxides and quantum dots formulated in poly(lactic acid)-D-alpha-tocopheryl polyethylene glycol 1000 succinate nanoparticles. *Biomaterials* 32, 2969 (2011).
142. Y.-H. Li, T. Song, J.-Q. Liu, S.-J. Zhu, and J. Chang, An efficient method for preparing high-performance multifunctional polymer beads simultaneously incorporated with magnetic nanoparticles and quantum dots. *J. Mater. Chem.* 21, 12520 (2011).
143. X. Hong, J. Li, M. Wang, J. Xu, W. Guo, J. Li, Y. Bai, and T. Li, Fabrication of magnetic luminescent nanocomposites by a layer-by-layer self-assembly approach. *Chem. Mater.* 16, 4022 (2004).
144. L. Jie-Mei, X. Xiao-Liang, L. Ling, Y. Nai-Qiang, and Z. Li-Xin, Preparation and characterization of bimodal magnetofluorescent nanoprobes for biomedical application. *Chin. Phys. Lett.* 29, 097803 (2012).
145. H.-M. Fan, M. Olivo, B. Shuter, J.-B. Yi, R. Bhuvaneswari, H.-R. Tan, G.-C. Xing, C.-T. Ng, L. Liu, S. S. Lucky, B.-H. Bay, and J. Ding, Quantum dot capped magnetite nanorings as high performance nanoprobe for multiphoton fluorescence and magnetic resonance imaging. *J. Am. Chem. Soc.* 132, 14803 (2010).
146. J. Lee, H. Kim, T. Sim, and R. Song, A new quantum dot-platinum conjugate for self-assembled nanoconjugates by coordination bonding mediated recognition. *Chem. Comm.* 49, 6182 (2013).
147. J. Lee, G. Hwang, Y. S. Hong, and T. Sim, One step synthesis of quantum dot-magnetic nanoparticle heterodimers for dual modal imaging applications. *Analyst.* 140, 2864 (2015).
148. P.-C. Lin, T.-W. Chiou, and H.-J. Harn, "Evidence-Based Anticancer Materia Medica," (W. C. S. Cho, Ed.), pp. 131–153, Springer Netherlands, 2011.
149. S. C. Erwin, L. Zu, M. I. Haftel, A. L. Efros, T. A. Kennedy, and D. J. Norris, Doping semiconductor nanocrystals. *Nature* 436, 91 (2005).
150. R. Beaulac, S. T. Ochsenbein, and D. R. Gamelin, "Nanocrystal Quantum Dots," (V. I. Klimov, Ed.). Taylor and Francis, Boca Raton, 2010.
151. R. Buonsanti and D. J. Milliron, Chemistry of doped colloidal nanocrystals. *Chem. Mater.* 25, 1305 (2013).
152. G. M. Dalpian and J. R. Chelikowsky, Self-purification in semiconductor nanocrystals. *Phys. Rev. Lett.* 96, 226802 (2006).
153. D. J. Norris, A. L. Efros, and S. C. Erwin, Doped nanocrystals. *Science* 319, 1776 (2008).
154. D. Mocatta, G. Cohen, J. Schattner, O. Millo, E. Rabani, and U. Banin, Heavily doped semiconductor nanocrystal quantum dots. *Science* 332, 77 (2011).
155. P. Wu and X.-P. Yan, Doped quantum dots for chemo/biosensing and bioimaging. *Chem. Soc. Rev.* 42, 5489 (2013).
156. P. K. Santra and P. V. Kamat, Mn-doped quantum dot sensitized solar cells: A strategy to boost efficiency over 5%. *J. Am. Chem. Soc.* 134, 2508 (2012).
157. Z. Huang, X. Zou, and H. Zhou, A strategy to achieve superior photocurrent by Cu-doped quantum dot sensitized solar cells. *Mater. Lett.* 95, 139 (2013).
158. S. K. Panda, S. G. Hickey, H. V. Demir, and A. Eychmüller, Bright white-light emitting manganese and copper co-doped ZnSe quantum dots. *Angew. Chem. Int. Ed.* 123, 4524 (2011).
159. N. Pradhan and D. D. Sarma, Advances in light-emitting doped semiconductor nanocrystals. *J. Phys. Chem. Lett.* 2, 2818 (2011).
160. M. Geszke-Moritz, G. Clavier, J. Lulek, and R. Schneider, Copper- or manganese-doped ZnS quantum dots as fluorescent probes for detecting folic acid in aqueous media. *J. Lumin.* 132, 987 (2012).
161. P. Wu, L.-N. Miao, H.-F. Wang, X.-G. Shao, and X.-P. Yan, A Multidimensional sensing device for the discrimination of proteins

based on manganese-doped ZnS quantum dots. *Angew. Chem. Int. Ed.* 50, 8118 (2011).
162. H. R. Rajabi, O. Khani, M. Shamsipur, and V. Vatanpour, High-performance pure and Fe^{3+}-ion doped ZnS quantum dots as green nanophotocatalysts for the removal of malachite green under UV-light irradiation. *J. Hazard. Mater.* 250–251, 370 (2013).
163. M. H. Mendonça-Dias, E. Gaggelli, and P. C. Lauterbur, Paramagnetic contrast agents in nuclear magnetic resonance medical imaging. *Semin. Nucl. Med.* 13, 364 (1983).
164. D. Pan, A. H. Schmieder, S. A. Wickline, and G. M. Lanza, Manganese-based MRI contrast agents: Past, present, and future. *Tetrahedron* 67, 8431 (2011).
165. R. N. Bhargava, D. Gallagher, X. Hong, and A. Nurmikko, Optical properties of manganese-doped nanocrystals of ZnS. *Phys. Rev. Lett.* 72, 416 (1994).
166. R. Beaulac, P. I. Archer, S. T. Ochsenbein, and D. R. Gamelin, Mn^{2+}-doped CdSe quantum dots: New inorganic materials for spin-electronics and spin-photonics. *Adv. Funct. Mater.* 18, 3873 (2008).
167. K.-T. Yong, Mn-doped near-infrared quantum dots as multimodal targeted probes for pancreatic cancer imaging. *Nanotechnology* 20, 015102 (2009).
168. G. Sitbon, S. Bouccara, M. Tasso, A. Francois, L. Bezdetnaya, F. Marchal, M. Beaumont, and T. Pons, Multimodal Mn-doped I–III–VI quantum dots for near infrared fluorescence and magnetic resonance imaging: From synthesis to *in vivo* application. *Nanoscale* 6, 9264 (2014).
169. T. Jahanbin, M. Gaceur, H. Gros-Dagnac, S. Benderbous, and S. Merah, High potential of Mn-doped ZnS nanoparticles with different dopant concentrations as novel MRI contrast agents: Synthesis and *in vitro* relaxivity studies. *J. Nanopart. Res.* 17, 1 (2015).
170. S. Santra, H. Yang, P. H. Holloway, J. T. Stanley, and R. A. Mericle, Synthesis of water-dispersible fluorescent, radio-opaque, and paramagnetic CdS:Mn/ZnS quantum dots: A multifunctional probe for bioimaging. *J. Am. Chem. Soc.* 127, 1656 (2005).
171. H. Yang, S. Santra, and P. H. Holloway, Syntheses and applications of Mn-doped II–VI semiconductor nanocrystals. *J. Nanosc. Nanotech.* 5, 1364 (2005).
172. S. Wang, B. R. Jarrett, S. M. Kauzlarich, and A. Y. Louie, Core/shell quantum dots with high relaxivity and photoluminescence for multimodality imaging. *J. Am. Chem. Soc.* 129, 3848 (2007).
173. M. Gaceur, M. Giraud, M. Hemadi, S. Nowak, N. Menguy, J. P. Quisefit, K. David, T. Jahanbin, S. Benderbous, M. Boissière, and S. Ammar, Polyol-synthesized Zn0.9Mn0.1S nanoparticles as potential luminescent and magnetic bimodal imaging probes: Synthesis, characterization, and toxicity study. *J. Nanopart. Res.* 14, 1 (2012).
174. L. Jing, K. Ding, S. Kalytchuk, Y. Wang, R. Qiao, S. V. Kershaw, A. L. Rogach, and M. Gao, Aqueous manganese-doped core/shell CdTe/ZnS quantum dots with strong fluorescence and high relaxivity. *J. Phys. Chem. C* 117, 18752 (2013).
175. B. Lin, X. Yao, Y. Zhu, J. Shen, X. Yang, H. Jiang, and X. Zhang, Multifunctional manganese-doped core–shell quantum dots for magnetic resonance and fluorescence imaging of cancer cells. *New. J. Chem.* 37, 3076 (2013).
176. V. K. Sharma, S. Gokyar, Y. Kelestemur, T. Erdem, E. Unal, and H. V. Demir, Manganese doped fluorescent paramagnetic nanocrystals for dual-modal imaging. *Small* 10, 4961 (2014).
177. F. Zhang, F. He, X.-W. He, W.-Y. Li, and Y.-K. Zhang, Aqueous synthesis of highly luminescent surface Mn^{2+}-doped CdTe quantum dots as a potential multimodal agent. *Luminescence* 29, 1059 (2014).
178. K. Ding, L. Jing, C. Liu, Y. Hou, and M. Gao, Magnetically engineered Cd-free quantum dots as dual-modality probes for fluorescence/magnetic resonance imaging of tumors. *Biomaterials* 35, 1608 (2014).
179. I. F. Li and C.-S. Yeh, Synthesis of Gd doped CdSe nanoparticles for potential optical and MR imaging applications. *J. Mater. Chem.* 20, 2079 (2010).
180. W. Guo, W. Yang, Y. Wang, X. Sun, Z. Liu, B. Zhang, J. Chang, and X. Chen, Color-tunable Gd–Zn–Cu–In–S/ZnS quantum dots for dual modality magnetic resonance and fluorescence imaging. *Nano Res.* 7, 1581 (2014).
181. F. Zhang, T.-T. Sun, Y. Zhang, Q. Li, C. Chai, L. Lu, W. Shen, J. Yang, X.-W. He, Y.-K. Zhang, and W.-Y. Li, Facile synthesis of functional gadolinium-doped CdTe quantum dots for tumor-targeted fluorescence and magnetic resonance dual-modality imaging. *J. Mat. Chem. B* 2, 7201 (2014).
182. W. Yang, W. Guo, X. Gong, B. Zhang, S. Wang, N. Chen, W. Yang, Y. Tu, X. Fang, and J. Chang, Facile synthesis of Gd–Cu–In–S/ZnS bimodal quantum dots with optimized properties for tumor targeted fluorescence/MR *in vivo* imaging. *ACS Appl. Mater. Interfaces* 7, 18759 (2015).
183. A. K. Saha, P. Sharma, H.-B. Sohn, S. Ghosh, R. K. Das, A. F. Hebard, H. Zeng, C. Baligand, G. A. Walter, and B. M. Moudgil, Fe doped CdTeS magnetic quantum dots for bioimaging. *J. Mat. Chem. B* 1, 6312 (2013).
184. S. Aime, M. Fasano, and E. Terreno, Lanthanide(III) chelates for NMR biomedical applications. *Chem. Soc. Rev.* 27, 19 (1998).
185. E. J. Werner, A. Datta, C. J. Jocher, and K. N. Raymond, High-relaxivity MRI contrast agents: Where coordination chemistry meets medical imaging. *Angew. Chem. Int. Ed.* 47, 8568 (2008).
186. M. Port, J.-M. Idée, C. Medina, C. Robic, M. Sabatou, and C. Corot, Efficiency, thermodynamic and kinetic stability of marketed gadolinium chelates and their possible clinical consequences: A critical review. *Biometals* 21, 469 (2008).
187. J.-M. Idée, M. Port, I. Raynal, M. Schaefer, S. Le Greneur, and C. Corot, Clinical and biological consequences of transmetallation induced by contrast agents for magnetic resonance imaging: A review. *Fundam. Clin. Pharmacol.* 20, 563 (2006).
188. C. de Haën, Conception of the first magnetic resonance imaging contrast agents: A brief history. *Top Magn. Reson Imaging* 12, 221 (2001).
189. P. Hermann, J. Kotek, V. Kubicek, and I. Lukes, Gadolinium(iii) complexes as MRI contrast agents: Ligand design and properties of the complexes. *Dalton Trans.* 3027–3047 (2008).
190. G.-P. Yan, L. Robinson, and P. Hogg, Magnetic resonance imaging contrast agents: Overview and perspectives. *Radiography* 13, e5 (2005).
191. P. Caravan, Protein-targeted gadolinium-based magnetic resonance imaging (MRI) contrast agents: Design and mechanism of action. *Acc. Chem. Res.* 42, 851 (2009).
192. L. Moriggi, C. Cannizzo, E. Dumas, C. R. Mayer, A. Ulianov, and L. Helm, Gold nanoparticles functionalized with gadolinium chelates as high-relaxivity MRI contrast agents. *J. Am. Chem. Soc.* 131, 10828 (2009).
193. W. J. M. Mulder, G. J. Strijkers, G. A. F. van Tilborg, A. W. Griffioen, and K. Nicolay, Lipid-based nanoparticles for contrast-enhanced MRI and molecular imaging. *NMR in Biomed.* 19, 142 (2006).
194. Z. Zhou and Z.-R. Lu, Gadolinium-based contrast agents for magnetic resonance cancer imaging. *Wiley Interdiscip Rev. Nanomed. Nanobiotechnol.* 5, 18 (2013).
195. K. B. Ghaghada, M. Ravoori, D. Sabapathy, J. Bankson, V. Kundra, and A. Annapragada, New dual mode gadolinium nanoparticle contrast agent for magnetic resonance imaging. *Plos One* 4, e7628 (2009).
196. E. Karathanasis, J. Park, A. Agarwal, V. Patel, F. Zhao, A. V. Annapragada, X. Hu, and R. V. Bellamkonda, MRI mediated, non-invasive tracking of intratumoral distribution of nanocarriers in rat glioma. *Nanotechnology* 19, 315101 (2008).
197. F. Erogbogbo, C.-W. Chang, J. L. May, L. Liu, R. Kumar, W.-C. Law, H. Ding, K. T. Yong, I. Roy, M. Sheshadri, M. T. Swihart, and

P. N. Prasad, Bioconjugation of luminescent silicon quantum dots to gadolinium ions for bioimaging applications. *Nanoscale* 4, 5483 (2012).

198. W. J. M. Mulder, R. Koole, R. J. Brandwijk, G. Storm, P. T. K. Chin, G. J. Strijkers, C. de Mello Donegá, K. Nicolay, and A. W. Griffioen, Quantum dots with a paramagnetic coating as a bimodal molecular imaging probe. *Nano Lett.* 6, 1 (2006).
199. R. Koole, M. M. van Schooneveld, J. Hilhorst, K. Castermans, D. P. Cormode, G. J. Strijkers, C. de Mello Donegá, D. Vanmaekelbergh, A. W. Griffioen, K. Nicolay, Z. A. Fayad, A. Meijerink, and W. J. M. Mulder, Paramagnetic lipid-coated silica nanoparticles with a fluorescent quantum dot core: A new contrast agent platform for multimodality imaging. *Bioconjugate Chem.* 19, 2471 (2008).
200. L. Liu, W.-C. Law, K.-T. Yong, I. Roy, H. Ding, F. Erogbogbo, X. Zhang, and P. N. Prasad, Multimodal imaging probes based on Gd-DOTA conjugated quantum dot nanomicelles. *Analyst.* 136, 1881 (2011).
201. P. Verwilst, S. Park, B. Yoon, and J. S. Kim, Recent advances in Gd-chelate based bimodal optical/MRI contrast agents. *Chem. Soc. Rev.* 44, 1791 (2015).
202. Q. Zhou, K. Mu, L. Jiang, H. Xie, W. Liu, Z. Li, H. Qi, S. Liang, H. Xu, Y. Zhu, W. Zhu, and X. Yang, Glioma-targeting micelles for optical/magnetic resonance dual-mode imaging. *Int. J. Nanomedicine* 10, 1805 (2015).
203. W. J. M. Mulder, K. Castermans, J. R. van Beijnum, M. G. A. Oude Egbrink, P. T. K. Chin, Z. A. Fayad, C. W. G. M. Löwik, E. L. Kaijzel, I. Que, G. Storm, G. J. Strijkers, A. W. Griffioen, and K. Nicolay, Molecular imaging of tumor angiogenesis using $\alpha v\beta 3$-integrin targeted multimodal quantum dots. *Angiogenesis* 12, 17 (2009).
204. W. M. Mulder, K. Castermans, J. van Beijnum, M. A. Oude Egbrink, P. K. Chin, Z. Fayad, C. G. M. Löwik, E. Kaijzel, I. Que, G. Storm, G. Strijkers, A. Griffioen, and K. Nicolay, Molecular imaging of tumor angiogenesis using $\alpha v\beta 3$-integrin targeted multimodal quantum dots. *Angiogenesis* 12, 17 (2009).
205. G. A. F. van Tilborg, W. J. M. Mulder, P. T. K. Chin, G. Storm, C. P. Reutelingsperger, K. Nicolay, and G. J. Strijkers, Annexin A5-conjugated quantum dots with a paramagnetic lipidic coating for the multimodal detection of apoptotic cells. *Bioconjugate Chem.* 17, 865 (2006).
206. J. Savill and V. Fadok, Corpse clearance defines the meaning of cell death. *Nature* 407, 784 (2000).
207. R. L. M. Haas, D. de Jong, R. A. Valdés Olmos, C. A. Hoefnagel, I. van Den Heuvel, S. F. Zerp, H. Bartelink, and M. Verheij, *In vivo* imaging of radiation-induced apoptosis in follicular lymphoma patients. *Int. J. Radiat. Oncol. Biol. Phys.* 59, 782 (2004).
208. H. Yang, S. Santra, G. A. Walter, and P. H. Holloway, Gd^{III}-functionalized fluorescent quantum dots as multimodal imaging probes. *Adv. Mater.* 18, 2890 (2006).
209. C.-Y. Cheng, K.-L. Ou, W.-T. Huang, J.-K. Chen, J.-Y. Chang, and C.-H. Yang, Gadolinium-based CuInS2/ZnS nanoprobe for dual-modality magnetic resonance/optical imaging. *ACS Appl. Mater. Inter.* 5, 4389 (2013).
210. W. B. Tan and Y. Zhang, Multifunctional quantum-dot-based magnetic chitosan nanobeads. *Adv. Mater.* 17, 2375 (2005).
211. G. J. Stasiuk, S. Tamang, D. Imbert, C. Poillot, M. Giardiello, C. Tisseyre, E. L. Barbier, P. H. Fries, M. de Waard, P. Reiss, and M. Mazzanti, Cell-permeable Ln(III) chelate-functionalized inp quantum dots as multimodal imaging agents. *ACS Nano* 5, 8193 (2011).
212. G. J. Stasiuk, S. Tamang, D. Imbert, C. Gateau, P. Reiss, P. Fries, and M. Mazzanti, Optimizing the relaxivity of Gd(iii) complexes appended to InP/ZnS quantum dots by linker tuning. *Dalton Trans.* 42, 8197 (2013).
213. L. W. E. Starmans, M. B. Kok, H. M. H. F. Sanders, Y. Zhao, C. de Mello Donegá, A. Meijerink, W. J. M. Mulder, H. Grüll, G. J. Strijkers, and K. Nicolay, Influence of cell-internalization on relaxometric, optical and compositional properties of targeted paramagnetic quantum dot micelles. *Contrast Media Mol. Imaging.* 6, 100 (2011).
214. X. Xing, B. Zhang, X. Wang, F. Liu, D. Shi, and Y. Cheng, An "imaging-biopsy" strategy for colorectal tumor reconfirmation by multipurpose paramagnetic quantum dots. *Biomaterials* 48, 16 (2015).
215. J. Shen, Y. Li, Y. Zhu, X. Yang, X. Yao, J. Li, G. Huang, and C. Li, Multifunctional gadolinium-labeled silica-coated Fe_3O_4 and $CuInS_2$ nanoparticles as a platform for *in vivo* tri-modality magnetic resonance and fluorescence imaging. *J. Mater. Chem. B* 3, 2873 (2015).
216. M. F. Ferreira, G. Pereira, A. F. Martins, C. I. O. Martins, M. I. M. Prata, S. Petoud, E. Toth, P. M. T. Ferreira, J. A. Martins, and C. F. G. C. Geraldes, Ln[DO3A-N-[small alpha]-(pyrenebutanamido)propionate] complexes: Optimized relaxivity and NIR optical properties. *Dalton Trans.* 43, 3162 (2014).